

Molecular Dynamics Simulations of Coherent Structures in Strongly Coupled Yukawa Liquids

Ashwin Joy

Institute for Plasma Research, Gandhingar, India

A thesis submitted to the Board of Physical Sciences
in fulfilment of the requirements
for the degree of
Doctor of Philosophy

HOMI BHABHA NATIONAL INSTITUTE



October 17, 2011



Homi Bhabha National Institute

Programme: Ph.D.

Board of Studies in Physical Sciences

1. Name of the Constituent Institution: Institute for Plasma Research

2. Name of the Student: Ashwin Joy

3. Enrolment Number: PHYS 06 2007 04 007

4. Date of Enrolment in HBNI: September 3, 2007

5. Date of Submission of Thesis: August 18, 2011

6. Title of the Thesis: Molecular Dynamics Simulations of Coherent Structures in Strongly Coupled Liquids

7. Composition of the Doctoral Committee:

Sr No	Composition	Designation in HBNI	Name
a.	Chairman	Senior Professor	Abhijit Sen
b.	Convener (Guide)	Assistant Professor	R. Ganesh
c.	Co-Guide , if any Member	Assistant Professor	R. Srinivasan
d.	Member	Assistant Professor	M. Warner
e.	Member	Assistant Professor	D. Raju
f.	The Technology Adviser, if any	Invitee	

8. Number of Doctoral Committee Meetings held with respective dates:

30th October 2008
8th December 2009, 29th September 2010
4th May 2011

9. Name and Organization of the Examiner 1: Professor Sundaram Balasubramanian, INCASR, Bangalore
Recommendations of the Examiner 1 (Thesis Evaluation) (i) accepted, (ii) accepted after revisions, or (iii) rejected:

10. Name and Organization of the Examiner 2: Dr. Monojoy Goswami, Oak Ridge National Laboratory, USA.
Recommendations of the Examiner 2 (Thesis Evaluation) (i) accepted, (ii) accepted after revisions, or (iii) rejected:

Name & Signature of Dean-Academic, CI:

Dr. S. Mukherjee

Recommendations of the Viva Voce Board

1. Date of Viva Voce Examination: 17th October 2011

2. Recommendations for the award of the Ph.D. degree: Recommended / Not Recommended

(If Recommended, give summary of main findings and overall quality of thesis)

(If Not Recommended, give reasons for not recommending and guidelines to be communicated by Convener of the Doctoral committee to the student for further work)

Mr. Ashwin Joy is recommended for the award of The Ph.D. degree.

Using MD simulation, Ashwin has demonstrated the generation of large-scale, coherent structures arising out of instabilities such as KH, Centrifugal and Dipole interactions in strongly coupled Yukawa liquids. This theme has been comprehensively expanded and its novel aspects have been explored by Ashwin over the seven chapters that the thesis contains.

The generation of heat at small length scales and that of coherent structures at large length scales using particle-based simulations is one of the important findings of the work.

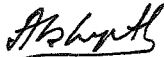
In particular, the development of a modular computer program using sophisticated algorithms and state-of-the-art programming practices is laudable.

In case Not Recommended, another date will be fixed by the Dean-Academic, CI, which shall not be earlier than a month after and not later than six months from the date of first viva.

Date: 17-Oct-2011

Name and Signature of the Viva Voce Board (Doctoral Committee and External Examiner):

ABHJIT SEN



R. SRINIVASAN

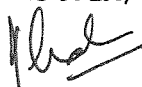


Mangj Wazari



Daniel Razi
S. Balasubramanian



 R. Govil

HOMI BHABHA NATIONAL INSTITUTE

Recommendations of the Viva Voce Board

As members of the Viva Voce Board, we certify that we have read the dissertation prepared by Ashwin Joy entitled "Molecular Dynamics Simulations of Coherent Structures in Strongly Coupled Yukawa Liquids" and recommend that it may be accepted as fulfilling the dissertation requirement for the Degree of Doctor of Philosophy.

Chairman:	Professor Abhijit Sen		Date: 17/10/2011
Guide/Convener:	Dr. R. Ganesh		Date: 17/10/2011
Member 1:	Dr. D. Raju		Date: 17.10.11
Member 2:	Dr. R. Srinivasan		Date: 17/10/11
Member 3:	Dr. M. Warriar		Date: 17/10/2011

Final approval and acceptance of this dissertation is contingent upon the candidate's submission of the final copies of the dissertation to the HOMI BHABHA NATIONAL INSTITUTE.

I hereby certify that I have read this dissertation prepared under my direction and recommend that it may be accepted as fulfilling the dissertation requirement.

R. Ganesh (Guide) 

Date: 17/10/2011



Homi Bhabha National Institute

Ph.D. Thesis Evaluation Report

1. Name of the Constituent Institution:	Institute for Plasma Research
2. Name of the Student:	ASHWIN JOY
3. Enrolment No. :	
4. Title of the Thesis:	Molecular Dynamics Simulations of Coherent Structures in Strongly Coupled Yukawa Liquids
5. Board of Studies:	

Recommendations

Tick one of the following:

1. The thesis in its present form is commended for the award of the Ph.D. Degree.
2. The thesis is commended for the award of the Ph.D. degree. However, my suggestions for improving the thesis may be considered at the time of the viva voce examination and if the viva voce board deems it appropriate, the same may be incorporated in the thesis based on the discussions during the viva voce examination. The revised thesis need not be sent to me.
3. The thesis should be revised as per the suggestions enclosed. I would like to see the revised thesis incorporating my suggestions before I give further recommendations.
4. The thesis is not acceptable for the award of the Ph.D. degree.

(Signature):

Name of Examiner: MONOJOY GOSWAMI

Date: Oct 3, 2011

Please give your detailed report in the attached sheet. You may use additional sheets, if required.

- | | |
|-------------------------|--|
| 1. Name of the Student: | ASHWIN JOY |
| 2. Enrolment No.: | |
| 3. Title of the Thesis: | Molecular Dynamics Simulations of Coherent Structures in Strongly Coupled Yukawa Liquids |
| 4. Board of Studies: | |

DETAILED REPORT

This thesis reports Molecular Dynamics (MD) simulation of strongly coupled Yukawa systems. Although the length scales of hydrodynamics and MD are entirely different, the authors did an excellent job to present the work in proper perspective. In my opinion, this thesis, in its present form, is ready for publication.

Chapter 1 does a good job in introducing the problem. In chapter 2, the author discusses the MD technique by introducing an example problem of Yukawa system near to the solid-liquid phase under a small external field. In chapter 3, the authors explained the Kelvin-Helmoltz instabilities in strongly coupled systems. The results are then compared with generalized hydrodynamics model with convincingly good qualitative agreement with the MD results. In chapter 4, the authors not only demonstrated the emergence of isolated coherent tripolar vortices from the decay of unstable axisymmetric flows in strongly coupled Yukawa liquids, they have tried to relate this work to other field of physics, e.g. condensed matter systems, which is quite fascinating. In chapter 5, the authors implemented a bold approach to explain the the formation and collision of dipolar vortices in a 2D Yukawa fluid. In my opinion, this is extremely difficult to do in MD because of the highly non-linear nature and much longer time scales of the problem. However, the authors did a profound job in performing the calculations using MD. In chapter 6, the authors did extensive MD calculations to understand the inverse cascade and spatio-temporal growth of a heat front in parallel shear flows of strongly coupled Yukawa fluid. Chapter 7 concludes with a summary of the work. I strongly recommend this thesis for the award of Doctor of Philosophy.

Name of Examiner:

MONOJOY GOSWAMI

Signature and Date:

 Oct 3, 2011



Homi Bhabha National Institute

Ph.D. Thesis Evaluation Report

1. Name of the Constituent Institution: INSTITUTE FOR PLASMA RESEARCH
2. Name of the Student: ASHWIN JOY
3. Enrolment No.: PHYS 06200704007
4. Title of the Thesis: Molecular Dynamics Simulations of Coherent Structures in Strongly coupled Yukawa liquid.
5. Name of the Board of Studies: "Board of Physical Sciences"

Recommendations

Tick one of the following:

1. The thesis in its present form is commended for the award of the Ph.D. Degree.
2. The thesis is commended for the award of the Ph.D. degree. However, my suggestions for improving the thesis may be considered at the time of the viva voce examination and if the viva voce board deems it appropriate, the same may be incorporated in the thesis based on the discussions during the viva voce examination. The revised thesis need not be sent to me.
3. The thesis should be revised as per the suggestions enclosed. I would like to see the revised thesis incorporating my suggestions before I give further recommendations.
4. The thesis is not acceptable for the award of the Ph.D. degree.

(Signature):

S. Balasubramanian

Name of Examiner: S. BALASUBRAMANIAN
JNCASR, BANGALORE

Date: 15 - SEP - 2011

Please give your detailed report in the attached sheet. You may use additional sheets, if required.

1. Name of the Student: ASHWIN JOY

2. Title of the Thesis: Molecular Dynamics Simulations of Coherent Structures in strongly Coupled Yukawa Liquids.

DETAILED REPORT

It was a delight to learn of and go through the thesis of Ashwin Joy. Although the area of plasma physics and instabilities in fluids is not one of my primary interests, I was able to grasp the thesis, thanks to the lucidity of the presentation. Ashwin Joy has clearly exploited the intrinsic power of particle-based molecular dynamics simulations to study large systems which are so essential to understand large scale hydrodynamic flows in dusty plasma. The fact that he has done so with a code that he has developed makes his work even more eminent and laudable. It is rare to see domain decomposition (and thus link lists) based MD codes for particles interacting via complex potentials (with the long range part taken care of by Ewald) being developed during the course of graduate study, in India. I am thus extremely pleased to see this successful effort of Ashwin.

The code (MPMD) has been put to excellent use, in a creative manner. The thesis discusses results of hydrodynamic flows established through transient external fields. These have enormous implications in energy dissipation in fluids in general, and plasmas in particular. The results are extremely novel and interesting. Ashwin has substantiated his numerical work by rationalizing the results through the solution of model equations, wherever possible. The work is comprehensive and constitutes a significantly large body. Nearly all the work have been published in highly reputed journals.

I warmly recommend the award of the Ph.D. degree to Mr. Ashwin Joy.

Name of Examiner: S. Balasubramanian

Signature and Date:

S. Balasubramanian

15/9/2011

Name of the Phd student : Ashwin JOY

Title of Thesis : Molecular Dynamics Simulation of Coherent Structures in Strongly Coupled Yukawa Liquids

CERTIFICATE

This is to certify that the corrections, if any, as indicated in the thesis evaluation report of the referee, have been incorporated in the Thesis.

Rajaraman Ganesh
(Thesis Supervisor)

Place : Bhat, Gandhinagar
Date : 17th October 2011

STATEMENT BY AUTHOR

This dissertation has been submitted in partial fulfillment of requirements for a Ph.D. degree at HOMI BHABHA NATIONAL INSTITUTE (HBNI) and is deposited in the Library to be made available to borrowers under rules of the HBNI.

Brief quotations from this dissertation are allowable without special permission, provided that accurate acknowledgement of source is made. Requests for permission for extended quotation from or reproduction of this manuscript in whole or in part may be granted by the competent authority of HBNI when in his or her judgment the proposed use of the material is in the interests of scholarship. In all other instances, however, permission must be obtained from the author.

A handwritten signature in blue ink, appearing to read 'Ashwin Joy', with a long horizontal stroke extending to the right.

Ashwin Joy

DECLARATION

I, hereby declare that the investigation presented in the thesis has been carried out by me. The work is original and has not been submitted earlier as a whole or in part for a degree/diploma at this or any other Institution/University.

A handwritten signature in blue ink, appearing to read "Ashwin Joy", with a long horizontal stroke extending to the right.

Ashwin Joy

To my beloved wife, Carmel . . .

Abstract

This thesis presents a computational study of large scale hydrodynamic flows in strongly coupled liquids using “first principles” classical molecular dynamics (MD) simulations. The prototype model used in the study is a Yukawa liquid. As is well known, Yukawa liquids are ubiquitous in nature and well known examples include complex or “dusty” plasmas, colloids and certain astrophysical systems such as giant planetary interiors and cometary tails, to mention a few. The components of a typical Yukawa liquid such as a complex plasma are electrons, positive ions, neutrals and negatively charged dust grains. Such a complex plasma can exist in a state of strong coupling where the ratio of average interparticle potential energy per dust grain can significantly exceed the average kinetic energy. It is important to note that the mutual influence of the components determines the physical state of the system, for eg. the grain-plasma interaction can lead to the charge on a given dust grain to be a function of time i.e $Q = Q(t)$. Hence, a complex plasma cannot, in general, be described by thermodynamic potentials and are as such *thermodynamically open* systems. As can be expected, an ideal description of complex plasma amounts to modeling grain-grain interactions including the dynamics of electrons, ions and neutrals. Such a description is clearly a formidable challenge even with the availability of modern day computers. One can, however, construct a near ideal “exact” description of complex plasma by considering only one charged species, namely the dust grains and assuming that both the grain charge and the background plasma do not evolve in time. This allows the grain dynamics to be modeled by a screened Coulomb or a Yukawa potential $U(r) = (1/r)\exp(-r/\lambda_D)$, where λ_D is the Debye length of the background plasma. The resulting N body

problem is numerically solved using a classical MD simulation.

Using “first principles” classical MD simulations, the present thesis reports the onset, growth and nonlinear saturation of large scale hydrodynamic instabilities in strongly coupled Yukawa liquids. To this end, a massively parallel **M**ulti **P**otential **M**olecular **D**ynamics (MPMD) code has been developed as part of this thesis. The code is extensively benchmarked against known results. The thesis begins with a study of Kelvin Helmholtz instability (KH) in parallel shear flows of a strongly coupled Yukawa liquid. At a given coupling strength, a subsonic shear profile is superposed on an equilibrated Yukawa liquid and an instability is observed. Linear growth rates directly computed from MD simulations are seen to increase with strong coupling and vortex roll formation in the non-linear regime is observed. The most interesting feature noticed here is the increase of instability growth rate with strong coupling. Interestingly, it is also observed that KH destabilized modes undergo inverse cascade leading to formation of giant coherent vortices. The emergence of such coherent vortices in the nonlinear regime of KH destabilized flows motivates one to investigate the stability of an isolated coherent vortex. The thesis also reports a comparison between growth rates directly obtained from MD simulations and a phenomenological generalized hydrodynamics (GH) model.

Following the study on parallel shears flows, we undertake a study on the evolution of axisymmetric flows in a 2D strongly coupled Yukawa liquid using MD simulations and report the emergence of coherent tripolar vortices in the nonlinear regime. Our MD simulations reveal that the tripolar vortices persist over several turn over times and hence may be observed in strongly coupled liquids such as complex plasma, liquid metals and astrophysical systems like white dwarfs and giant planetary interiors, thereby making the phenomenon universal. It is also seen that under certain conditions a tripolar vortex can spontaneously decay into a pair of dipolar vortices propagating in mutually opposite directions. Linear growth rates directly obtained from MD simulations are compared with a generalized hydrodynamic model. It is indeed very tempting to study if it is possible to excite such dipolar vortices from generic initial conditions and study their interactions in a laboratory

produced complex plasma. For this we undertake a study on evolution of jets in a strongly coupled Yukawa liquid using MD simulations. The initial state for this study is a sub-sonic jet profile superposed on a thermally equilibrated Yukawa liquid. A dipolar vortex is then seen to emerge from the self-organization of this jet profile. This dipole is seen to be very robust and, in general, shows a nonlinear relationship between vorticity and stream function. Starting from two jets injecting linear momentum in mutually opposite directions, we report on the centered head-on collisions between two dipolar vortices. It is seen that the inertial effects needed for the sustenance of dipolar vortices are rapidly quenched by gas friction. Hence, such dipolar vortices may be observed in a laboratory complex plasma at low gas friction.

In each of the foregoing flow studies, we noticed a significant heat generation close to the shear layers. This motivated us to perform a detailed study of molecular heat generation in shear flows of Yukawa liquids. To this end, we superposed a subsonic shear profile on an equilibrated Yukawa liquid and observed a KH instability. Inverse cascade leads to formation of giant coherent vortices. It is seen that while this inverse cascade leads to a continuous transfer of flow energy towards the largest scales, at the smallest scale there is also a simultaneous transfer of flow energy into the thermal velocities of grains. The latter is an effect of velocity shear and thus leads to the generation of a nonlinear heat front. We notice that the heat front is seen to propagate at speed much lesser than the adiabatic sound speed of the liquid in the linear regime. Hence, the spatio-temporal growth of this heat front occurs concurrently with the inverse cascade of KH modes.

The MD studies reported in the present thesis results are exact numerical solutions to the N body problem and hence “first principles” in nature. The results are “*to scale*”, for eg. in a typical laboratory dusty plasma, the dust plasma frequency $\omega_{pd} \sim 100$ Hz. A typical growth rate (normalized to ω_{pd}^{-1}) in the studies presented so far, falls in the range $\sim 10^{-3} - 10^{-2}$ and corresponds to $[0.1 - 1]$ Hz’s in physical units. Typical system size used in our studies, for eg. $L = 640$ (in units of Wigner Seitz radius a) corresponds to 26 cm approximately for $a = 0.4$ mm. Hence the hydrodynamic phenomena addressed in the thesis should be observable in laboratory experiments on

complex “dusty” plasma.

Acknowledgements

“He only is my rock and my salvation, my fortress; I shall not be shaken.”
(Psalms 62:6)

First and foremost, I wish to thank my thesis advisor, Dr. Rajaraman Ganesh, Institute for Plasma Research (IPR), for guiding me all the way in my research. I could not have imagined, having a better advisor and mentor for my Ph.D study. He is largely responsible for whatever scientific thinking and maturity I have gained so far during my stay at IPR. As I write this letter, I recall those numerous (close to infinite) instances where he emphasized the importance of reading good papers and extensive literature survey for doing great research. We would often discuss physics issues in his office (W6) or better still, in the corridor leading to the canteen. The discussions would almost invariably lead to a physics problem and in some very special cases - “Ashwin ! I think this is worth sending to PRL”. He always maintained the philosophy of balancing numerical work with extensive analysis for writing impactful papers. Apart from research, a very important thing I learnt from him is to remain calm in adverse situations. I guess that is a very important lesson one needs to learn before making a career in research. He is primarily responsible for both my aptitude and interest in numerical methods and high performance computing. The development of **MPMD** code would have remained a dream without his constant encouragement. I can only thank him from the bottom of my heart for sending me to ICTP, Trieste for an advanced school on high performance computing. It was indeed a great learning experience, truly unforgettable. During the most difficult times when writing this thesis, he gave me the moral support and

the freedom I needed to move on.

I am also indebted to my doctoral committee members Professor Abhijit Sen (Chairman), Dr. D. Raju, Dr. R. Srinivasan and Dr. M. Warriar for their timely comments on the progress of my thesis. Special thanks to Professor Sen for critically reading all my manuscripts and providing valuable inputs on each one of them. Many thanks to Dr. M. Warriar for the much needed initial help with molecular dynamics and monte carlo methods. I would like to personally thank Professor Kaw for his constant encouragement and support throughout my Ph.D. tenure. Despite his extremely busy schedule, he showed a lot of interest in my work and we had some very thought provoking and exciting discussions.

My stay at IPR graduate school was a lot of fun especially in the company of Deepak, Ujjwal, Prabal, Vikram, Kshitish, Rameswar and Sushil. I cherish those the funny moments during numerous tea breaks spent with Gurudatt, Sita, Sharad, Sanat and Vikrant. I would also like to thank the library and computer center for their excellent facility and help throughout my Ph.D.

I am falling short of words to thank my wife Carmel, whose love and confidence in me, took a great load off my shoulder. Without her I would have been a very different person today (definitely worse !), and it would have been certainly much harder to finish a Ph.D. Apart from being my wife, she has also been a very good friend and critic. In spite of her busy job schedule and domestic work, she has been tough and always supported my goals. She has also been a fantastic walking dictionary all this while correcting me on numerous typographical errors in literally everything ranging from talks, papers and to the present thesis. Thank you baby !

Ashwin Joy.

Contents

Abstract	i
Acknowledgements	v
List of Figures	xi
List of Publications	xiii
1 Introduction	1
1.1 Brief overview of complex plasma	2
1.2 Exact description of complex plasma	4
1.3 Plan of the thesis	6
2 Molecular Dynamics	11
2.1 Yukawa model for complex plasma	11
2.2 Dimensionless units	13
2.3 Boundary conditions	16
2.4 Initial state	17
2.5 Integration	18
2.6 MPMD code	19
2.6.1 Performance	19
2.6.2 Driven Yukawa system	22
2.6.3 Radial distribution function	25
2.6.4 Lattice correlation	28
2.6.5 Diffusion	29
2.6.6 Velocity autocorrelation	31
2.6.7 Mechanism of melting	32
2.7 Summary	34
3 Parallel Shear Flows	37
3.1 Introduction	37
3.2 Initial state	39

3.3	Comparison with hydrodynamics	43
3.4	Role of gas friction	47
3.5	Generalized hydrodynamics	49
3.6	Basic assumptions	52
3.7	Model equations	53
3.8	Effect of coupling parameter on shear viscosity and relaxation time	60
3.9	Effect of coupling parameter on GH growth rates	61
3.10	Effect of shear induced heating on growth rates	62
3.11	Summary	64
4	Centrifugal Flows	68
4.1	Introduction	68
4.2	Molecular dynamics	69
4.3	Evolution of a tripole	71
4.4	Effect of strong coupling	73
4.5	Comparison with viscoelastic model	74
4.6	Summary	78
5	Formation and Interaction of Dipoles	79
5.1	Introduction	79
5.2	Molecular dynamics	81
5.3	Viscous decay	86
5.4	Dipole interactions	87
5.5	Role of gas friction	89
5.6	Summary	91
6	Heat Front Propagation	94
6.1	Introduction	94
6.2	Molecular dynamics	95
6.3	Kelvin Helmholtz instability	96
6.4	Vorticity field	97
6.5	Topology of turbulent mixing	100
6.6	Inverse cascade of KH modes	101
6.7	Development and growth of heat front	104
6.8	Summary	111
7	Conclusions	113
7.1	Results	113
7.2	Future Work	117

Appendices	119
A	120
A.1 Gaussian Thermostat	120
A.2 Berendsen Barostat	121
A.3 Ewald sums	123
Bibliography	124

List of Figures

1.1	Experimental realization of a complex plasma	2
2.1	Yukawa potential in MD units	15
2.2	Schematic diagram showing periodic boundary conditions . . .	16
2.3	The parallel cell subdivision method	20
2.4	A close up of cells	21
2.5	Path through the linked list	22
2.6	External potential V_E and corresponding force F_z	23
2.7	Phase diagram of a Yukawa system	24
2.8	Plot of Γ as a function of time at various V_0	25
2.9	Fall in the peaks of $g(r)$ at various V_0	27
2.10	Fall in lattice correlation ($ n(\mathbf{k}) $) with time at various V_0 . . .	28
2.11	Diffusion at various V_0	30
2.12	Fourier transformed velocity autocorrelation	31
2.13	Snapshots of temperature along \hat{z}	33
2.14	The profile of temperature along \hat{z}	34
2.15	Melting time (t_m) versus V_0	35
3.1	PCF vs r at various values of Γ	40
3.2	Trajectories of particles in a square region of size 40×40 . . .	41
3.3	Time evolution of perturbed kinetic energy E_k	42
3.4	Time evolution of \hat{x} independent velocity shear profile	43
3.5	Growth rate spectra of KH instability calculated from MD . . .	44
3.6	Roll up of vortices at various Γ	45
3.7	Inverse cascading of mode $m_n = 6$ at $\Gamma = 50$	46
3.8	Effect of gas friction: Vorticity snapshots	48
3.9	Effect of gas friction: MD growth rates	49
3.10	Percentage density fluctuation at $t = 40$	52
3.11	Growth rate spectra of GH model	58
3.12	Plot of η and $R = U_0 nl / \eta$ vs Γ taken from MD simulations . .	59
3.13	Viscoelastic relaxation time τ_m vs Γ	60

3.14	Comparison of growth rate spectra from MD and GH model	62
3.15	Snapshot showing shear induce heating	63
3.16	Profiles Γ as a function of y at $x = 0$	64
3.17	Effect of shear induced heating on growth rates	65
3.17	Continued	66
3.17	Continued	66
4.1	Energy conservation	71
4.2	Emergence of a tripole	72
4.3	Time evolution of tripole at various Γ	73
4.4	Time evolution of perturbed radial kinetic energy	75
4.5	Growth rate spectrum from MD and GH model	77
5.1	Evolution of a jet profile at $\nu_{dn} = 0$	83
5.2	Snapshots showing evolution of dipole vorticity at $\nu_{dn} = 0$	84
5.3	Contour plot of density fluctuation δn	85
5.4	Scatter plot of ω vs ψ	86
5.5	Time evolution of peak vorticity $\bar{\omega}_m$ and kinetic energy \bar{E}_k	87
5.6	Centered head-on collision between two dipoles	88
5.7	Time evolution of a dipole at finite gas friction $\nu_{dn} \neq 0$	90
5.7	Continued	91
5.8	Time evolution of a dipole at finite gas friction $\nu_{dn} \neq 0$	92
6.1	Snapshots showing time evolution of color coded particles	97
6.2	Vorticity field ($\omega = \nabla \times \mathbf{v}$)	98
6.3	Temporal snapshots of vorticity field	99
6.3	Continued	100
6.4	Temporal snapshots of the field of Okubo-Weiss parameter \mathcal{Q}	102
6.4	Continued	103
6.5	Power spectrum of KH modes	104
6.6	Temporal snapshots of Γ field	105
6.6	Continued	106
6.7	Time evolution of $\langle \Gamma \rangle_{xy}$	107
6.8	$\Gamma(y)_{x=0}$ at different times	107
6.9	Speed of heat front	108
6.10	$\langle \frac{\Delta n}{n_0} \rangle_{xy}$ at different times	108
6.11	Temporal snapshots of density n field	110
6.11	Continued	111

List of Publications

Journals

1. **Ashwin J.** and R. Ganesh,
“Formation and interaction of dipolar vortices in strongly coupled Yukawa liquids”,
(Under Review)
2. **Ashwin J.** and R. Ganesh,
“Coevolution of inverse cascade and nonlinear heat front in shear flows of strongly coupled Yukawa liquids”,
Phys. Plasmas (**18**), 083704 (2011)
3. **Ashwin J.** and R. Ganesh,
“Coherent vortices in strongly coupled liquids”,
Phys. Rev. Lett. (**106**), 135001 (2011)
4. **Ashwin J.** and R. Ganesh,
“Parallel shear flow instabilities in strongly coupled Yukawa liquids - A comparison of generalized hydrodynamic model and molecular dynamics results”,
Phys. Plasmas (**17**), 103706 (2010)
5. **Ashwin J.** and R. Ganesh,
“Kelvin-Helmholtz instability in strongly coupled Yukawa liquids”,
Phys. Rev. Lett. (**104**), 215003 (2010)
6. **Ashwin J.** and R. Ganesh,
“Effect of external drive on strongly coupled Yukawa systems : A nonequilibrium molecular dynamics study”,
Phys. Rev. E. (**80**), 056408 (2009)

Conferences

1. **Ashwin J.**, R. Ganesh,
“Kolmogorov Flows in Strongly Coupled Plasmas: A Molecular Dynamics Study”,
22nd International Conference on Numerical Simulation of Plasmas,
Princeton Plasma Physics Laboratory, Sep 7-9, 2011, New Jersey, USA.
2. R. Ganesh and **Ashwin J.**,
“Shear Flows in Two Dimensional Strongly Coupled Yukawa Liquids :
A Large Scale Molecular Dynamics Study”,
6th International Conference on the Physics of Dusty Plasmas, May
16-20, 2011, Garmisch-Partenkirchen, Germany.
3. **Ashwin J.**, R. Ganesh and M. Warriar,
“Calculation of transport coefficients using non-equilibrium molecular
dynamics (NEMD)”,
22nd National Symposium on Plasma Science & Technology, Nov 2007,
Ahmedabad, India.

Invited Talks

1. “Shear Flows in Strongly Coupled Yukawa liquids”,
Department of Physics, Auburn University, Alabama, USA
Host : Professor Edward Thomas Jr.
September 12-13, 2011.

Chapter 1

Introduction

Ordinary matter can exist in either solid, liquid, gaseous or a plasma state. The latter can exist either in a partially ionized state in the presence of neutral particles or a fully ionized state- an ideal case encountered in “hot” plasmas such as in fusion Tokamaks or in the interior of stars. There exists, however, a new state of matter called “complex plasma” which is qualitatively different from these ordinary states of matter ([Morfill and Ivlev, 2009](#); [Tsytoich et al., 2008](#)). A complex plasma contains mesoscopic charged grains, positive ions, electrons and neutral gas atoms. Under most circumstances, the grain-grain interaction can be well described by a Yukawa potential. As it will be seen in this chapter, such a complex plasma can exist in a state of strong coupling wherein the average potential energy per grain can significantly exceed the average kinetic energy. The behavior of component grains in this strongly coupled regime is very different from that in the weakly coupled regime. In the former, where potential energy is dominant, particle trajectories are less mobile as a “caging effect” takes place due to the neighbors, whereas in the latter, thermal effects are dominant and the particle trajectories are more mobile and hence disordered in nature. Such strong coupling effects manifest themselves in solid like behavior, such as, possessing long range crystalline order and ability to support transverse shear waves. In the present chapter, we shall first discuss some important characteristics of a strongly coupled Yukawa liquid and then present the development of

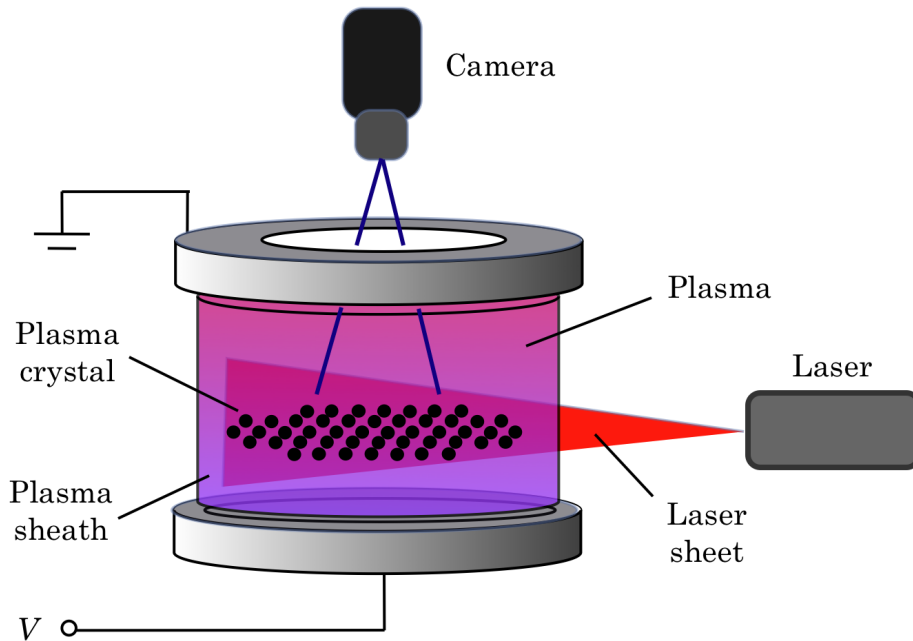


Figure 1.1: A typical experimental setup for a ground based complex plasma experiment [Figure adapted from (Donkó et al., 2009)]

a molecular dynamics code. Various diagnostics developed are discussed in detail and a phase transition study is reported.

1.1 Brief overview of complex plasma

Complex dusty plasma can be created in laboratory experiments by dispersing micron-sized particles or dust grains into an inert gas discharge [see Figure 1.1]. The discharge can be driven either by a direct current (dc) or by a radio-frequency (rf) source, and serves primarily as a charging medium for the dust grains. The grains are exposed to electron and ion currents from the discharge plasma, and a dynamic equilibrium is rapidly reached. As the impinging electrons have a much higher mobility compared to positive ions, the dust grains eventually become negatively charged. Hence, the principle components of such a laboratory produced complex plasma are electrons, positive ions, neutrals and negatively charged dust grains. These components

interact strongly with each other in such a way that the mutual influence of the components determines the physical state of the system. The two main characteristics of complex plasma are: (1) the *grain charges are very high* causing new phenomena in grain plasma as well as grain-grain interactions and, (2) the *grains strongly absorb plasma components (electrons and ions)* and hence their charges vary as a function of time. Thus complex plasmas are non-Hamiltonian systems where the energy of the system varies not only in the presence of external electric fields, but also due to mutual particle collisions. This limits the description of a complex plasma in terms of thermodynamic potentials and leaves it with a high tendency to form various types of structures often referred to as “self organized structures”. Even at low grain densities, the huge charges (sometimes upto $10^4 - 10^5$ of elementary electron charges per grain) on the grain component in a complex plasma make the grain-grain as well as grain-plasma interactions very strong (Tsytovich et al., 2008). Complex plasma can thus exist in a state of strong coupling where the average potential energy per grain can significantly exceed the average kinetic energy per grain. In such a strongly coupled complex plasma, the coupling parameter $\Gamma = Q^2/(4\pi\epsilon_0 a T_d)$ can be easily of the order 1 or larger (Q , T_d and a are the dust charge, temperature and the Wigner-Seitz radius respectively). This coupling parameter Γ can be easily controlled in experiments and a complex plasma can be made to undergo a phase transition from a liquid-like to a solid-like state, for eg., several experiments on two-dimensional (2D) and three-dimensional (3D) (under microgravity conditions) complex plasmas have been done exploring a wide variety of collective phenomena (Barkan et al., 1995; Chu et al., 1994; Khrapak et al., 2003).

Interestingly, complex plasmas can also be used as a model system to study generic strong coupling phenomena. This is mainly because the characteristic length and dynamical time scales are vastly “stretched” in comparison to atomic systems - by typically a factor of a million (atomic systems have interaction scale $\sim 0.1\text{nm}$ and complex plasma $\sim 100\ \mu\text{m}$; typical plasma frequencies $\sim 10^8\ \text{Hz}$ at $10^{12}\ \text{cm}^{-3}$ densities and complex plasma frequencies are $\sim 100\ \text{Hz}$ at similar densities) (Fortov et al., 2005). The rate of momentum exchange between dust grains can substantially exceed the damping rate due

to neutral gas friction making complex plasmas behave essentially as single phase systems (Khrapak et al., 2004). Thus complex plasma enables one to study the physics of linear, nonlinear and critical phenomena at the smallest possible length scale i.e at the “particle level”, experimentally (Morfill and Ivlev, 2009; Fortov et al., 2005).

1.2 Exact description of complex plasma

An ideal description of complex plasma amounts to modeling grain-grain interactions including the dynamics of electrons, ions and neutrals. Clearly, such a description is improbable even in the advent of modern fast computers. One can, however, construct a near ideal “exact” description of complex plasma by considering only one charged species, namely the dust grains and assuming that both the grain charge and the background plasma do not evolve in time. Such an assumption is valid as the typical charging times are at least three orders of magnitude smaller than the inverse dust plasma frequency (Morfill and Ivlev, 2009). This allows the grain dynamics to be modeled by a screened Coulomb or a Yukawa potential $U(r) = (1/r)\exp(-\kappa r)$, where $\kappa = a/\lambda_D$ and λ_D are the screening parameter and the Debye length of the background plasma respectively. The resulting N body problem is numerically solved using a classical molecular dynamics (MD) simulation. Such an MD simulation has two distinct advantages over any conventional continuum method: a.) microscopic fluctuations are included and, b.) more realistic boundaries can be handled. Owing to its gridless nature, an MD method is also unconditionally stable. Moreover, in a typical large scale MD simulation, one can easily control the interaction between dust grains, for example, making complex plasma behave as *coulomb gas* ($\kappa \rightarrow 0$) or an *ideal gas* ($\kappa \rightarrow \infty$) at the flick of a switch (κ). In past, several authors have used such MD simulations to study transport phenomena (Saigo and Hamaguchi, 2002; Liu and Goree, 2005, 2008), thermodynamics (Hamaguchi et al., 1996, 1997) and collective behavior (Ohta and Hamaguchi, 2000b) in strongly coupled complex plasmas. It should be noted that these works were performed with only a few thousands of particles and hence small scale in nature. There

exists, however, a class of problems in complex plasmas where such a “first principles” study has so far, remained elusive. These are the “hydrodynamic instabilities” - a subject traditionally studied only through continuum methods. Recently, some of these hydrodynamic instabilities have been characterized at the most fundamental level of particle motion by MD simulations of Lennard Jones fluids on the latest generation of supercomputers (Rapaport and Clementi, 1986b; Puhl et al., 1989; Dzwinel et al., 2000; Hirshfeld and Rapaport, 2000; Kadau et al., 2004). One then naturally wonders if it is possible to make quantitative investigations of large scale hydrodynamic flows in a complex “dusty” plasma using a particle level description. The implications of such a study are extremely important as one can take less than a million dust grains and simulate realistic system sizes due to the vastly stretched length scales (grain separation $\sim 100's \mu\text{m}$ (Morfill and Ivlev, 2009)) typical of a complex plasma. For example, if one takes 2.5×10^5 grains in a simulation square box of size $640a$, where $a \approx 0.4 \text{ mm}$, then this corresponds to a region of size 26cm. Such a system size is comparable to the macroscopic length scales usually seen in laboratory experiments. Thus, the present thesis offers a unique possibility of comparing highly resolved experiments with particle level simulations on large scale hydrodynamic flows in strongly coupled Yukawa liquids.

To summarize, the aim of the present thesis is to go beyond the limits of continuous media and study the onset and growth of large scale hydrodynamic instabilities in complex plasmas using “first principles” classical MD simulations. The prototype system used in the present studies is a 2D strongly coupled Yukawa liquid. It should be noted that in reality, other external forces such as ion drag and thermophoretic forces do exist in addition to grain-grain interactions. In the present thesis however, we exclude such forces and provide a simple picture of complex plasma by keeping only the grain-grain interactions via Yukawa potential. The role of gas friction on the evolution of these large scale flows is also discussed in subsequent chapters. The results reported here are exact numerical solutions to the N body problem and hence “first principles” in nature. Wherever possible, comparison between MD results and a generalized hydrodynamic (GH) model is pre-

sented. In the following, we give a content-wise break up of all the chapters forming the present thesis.

1.3 Plan of the thesis

In chapter 2, the computational methods used in the thesis are explained in full detail. The development of a Multi Potential Molecular Dynamics (MPMD) code is discussed. The code has been exhaustively benchmarked against known results (Donko et al., 2008). The modular design of the code makes the addition of new force fields very easy. Presently, the code can handle Yukawa and Lennard-Jones inter-atomic potentials. Boundaries can be implemented in both periodic or hard walls fashion. MPMD can simulate various thermodynamic ensembles such as NVT, NVE, NPT by employing a Gaussian thermostat (Evans et al., 1983) and an Andersen barostat (Andersen, 1980). To capture the underlying physics, several statistical mechanics and fluid dynamics diagnostics have been developed. Algorithms implemented to achieve high performance or speed up are discussed in detail. In realistic experiments, a strongly coupled complex plasma can exist in a 2D (ground based laboratory) or 3D (microgravity) crystalline forms (Morfill et al., 1999). It should be noted that the confinement of dust grains in such experiments is achieved through the balance of gravity and external electric fields. Hence, it is natural to expect that a complex plasma can form different structures other than the regular fcc and bcc structures under the effect of these confining forces. For eg., Totsuji (Totsuji, 2001; Totsuji et al., 1997) studied the formation of layers in a dusty plasma due to an external confining potential. This confining potential had a magnitude much larger than the average inter-particle potential energy and the simulations were done in equilibrium conditions. Melting of dusty plasma crystals in presence of spatially random and time varying external fields have been studied by Hoffman (Hoffmann and Lowen, 2000) using Fokker-Planck dynamics. In contrast to that work, we investigate, as a test problem for MPMD code, the effect of a small external drive on a Yukawa solid through nonequilib-

rium MD simulations. It should be noted that the magnitude of this drive is smaller compared to the average inter-particle potential energy. Neglecting any ion streaming effects due to external field (Kompaneets et al., 2009), a 3D Yukawa solid (bcc) near solid-liquid boundary (Hamaguchi et al., 1997) is subjected to an external drive at the largest possible scale. The external drive varies sinusoidally in space, and for a given mode k_L , it is observed that there exists a critical amplitude V_o^c of the external drive, below which the crystalline order is preserved and above which the transition from bcc to strongly coupled Yukawa liquid is observed. This critical amplitude V_o^c is sensitive to the location of the Yukawa solid in (κ, Γ) phase space and (Ashwin and Ganesh, 2009). The mechanism of heating in the transient state is attributed to the local heating of the system where the forces are maximum. It is shown that these local hot regions dissipate heat into surrounding regions ultimately leading to a uniform temperature throughout the system. Following this study, in subsequent chapters, we report “first principles” simulations of large scale hydrodynamic flows of strongly coupled Yukawa liquids.

In chapter 3, using “first principles” classical molecular dynamics simulations Kelvin Helmholtz (KH) instability is reported for the first time at the particle level in two-dimensional strongly coupled Yukawa liquids (Ashwin and Ganesh, 2010a). At a given coupling strength Γ , a subsonic shear profile is superposed on an equilibrated Yukawa liquid and KH instability is observed. Linear growth rates directly computed from MD simulations are seen to increase with strong coupling and vortex roll formation in the non-linear regime is observed. Instability growth rates are seen to increase with strong coupling. Interestingly, KH destabilized modes undergo inverse cascading in the strongly coupled regime as well. The work highlights several important questions such as the study of random perturbation (multiple modes with random amplitudes), comparison to viscoelastic hydrodynamics, shock propagation and the study of flows with resonantly unstable modes. Further, using a generalized hydrodynamic (GH) model, the growth rate spectra of Kelvin Helmholtz (KH) instability has been obtained analytically for a step shear

profile in a strongly coupled Yukawa liquid (Ashwin and Ganesh, 2010b). Within this GH model, the class of shear flows studied is assumed to be incompressible in nature. The growth rate spectra calculated exhibit viscous damping at high mode numbers, destabilization at stronger coupling and in the limit τ_m (viscoelastic relaxation time) $\rightarrow 0$, reduce to the regular Navier-Stokes growth rate spectra. A direct comparison is made with previous molecular dynamics (MD) simulations of KH instability (Ashwin and Ganesh, 2010a). It is found that for a given value of Reynolds number R and coupling parameter $1 < \Gamma < 100$, the GH and MD growth rates are in a qualitative agreement. Inclusion of the effect of shear heating as an effective coupling parameter Γ_e appears to improve the quantitative comparison as well. However, it is observed that there is a general disagreement between GH and MD growth rates at high mode numbers for all values of Γ_e . This could be due to the limitations of the GH model, especially, the uncertainties in the determination of shear viscosity $\eta(\Gamma)$ and the viscoelastic relaxation time τ_m . The emergence of coherent vortices in the nonlinear regime of KH destabilized flows motivates one to think of the stability of an isolated coherent vortex. This is the subject matter of following chapter.

In chapter 4, we report on the emergence of coherent tripolar vortices from the evolution of axisymmetric flows in a 2D strongly coupled Yukawa liquid using “first principles” MD simulations (Ashwin and Ganesh, 2011b). MD simulations reveal that the tripolar vortices persist over several turn over times and hence may be observed in strongly coupled liquids such as complex plasma, liquid metals and astrophysical systems like white dwarfs and giant planetary interiors, thereby making the phenomenon universal. Further, linear growth rates directly obtained from MD simulations are compared with a generalized hydrodynamic model. It is also seen that under certain conditions, a tripolar vortex can spontaneously decay into a pair of dipolar vortices propagating in mutually opposite directions. One then naturally wonders if it is possible to excite such dipolar vortices from generic initial conditions and study their interactions in a laboratory produced complex plasma, which is the subject matter of following chapter.

In chapter 5, we report on the formation and interaction of dipolar vortices in a two-dimensional prototype strongly coupled liquid, namely the Yukawa liquid (Ashwin and Ganesh, Under Review). As is well known, coherent dipolar vortices are a universal outcome of injecting linear momentum into a liquid. Once formed, these dipolar vortices can transport mass and momentum over large length scales and are hence a subject matter of intense research work. Using “first principles” classical molecular dynamics simulations, a dipolar vortex is seen to emerge from the self-organization of a sub-sonic jet profile. This dipole is seen to be very robust and, in general, shows a nonlinear relationship between vorticity and stream function. Starting from two jets injecting linear momentum in mutually opposite directions, we report on the centered head-on collisions between two dipolar vortices. Our work highlights the possibility of observing such dipolar vortices and their interactions in laboratory experiments on strongly coupled complex plasma. Role of gas friction is also investigated.

In all the foregoing shear flow studies (chapters 3,4,5), generation of heat is observed at the particle level close to shear layers. Such shear induced heat front development and propagation in large scale shear flows of a strongly coupled Yukawa liquid is the subject matter of the following chapter.

In chapter 6, we report on the coevolution of inverse cascade and nonlinear heat front in shear flows of strongly coupled Yukawa liquids using MD simulations (Ashwin and Ganesh, 2011a). At a given coupling strength, a subsonic shear profile is superposed on an equilibrated Yukawa liquid and Kelvin Helmholtz (KH) instability is observed. Coherent vortices are seen to emerge towards the nonlinear regime of the instability. It is seen that while inverse cascade leads to a continuous transfer of flow energy towards the largest scales, at the smallest scale there is also a simultaneous transfer of flow energy into the thermal velocities of grains. The latter is an effect of velocity shear and thus leads to the generation of a nonlinear heat front. In the linear regime, the heat front is seen to propagate at speed much lesser

than the adiabatic sound speed of the liquid. Spatio-temporal growth of this heat front occurs concurrently with the inverse cascade of KH modes.

Finally, in chapter 7, we present the conclusions of the work reported in the present thesis. It should be noted that the simulations reported here required large computing power and were carried out on a maximum of 32 nodes on a parallel Linux cluster.

Chapter 2

Molecular Dynamics

In this chapter we present the methodology of classical molecular dynamics algorithm for a Yukawa liquid. The simulation domain is a cubic region of a three-dimensional (3D) strongly coupled Yukawa liquid. Periodic boundaries have been used along all directions and the Ewald sums (see appendix [A.3](#)) are employed to handle the long range Yukawa forces. The development of a parallel **M**ulti **P**otential **M**olecular **D**ynamics (MPMD) code is discussed. Various issues such as setting up of the initial state and performing simulations under constant temperature, pressure or energy conditions are discussed. Algorithms implemented to achieve speed up are discussed in detail. When studying phase transitions, the underlying physics is captured through important statistical mechanics tools. Finally, we undertake a nonequilibrium test problem of driven Yukawa liquids to benchmark these tools.

2.1 Yukawa model for complex plasma

An ideal description of complex plasma amounts to modeling grain-grain interactions including the dynamics of electrons, ions and neutrals. Clearly, such a description is unlikely even in the presence of modern fast computers. One can, however, construct a near ideal “exact” description of complex plasma by considering only one charged species, namely the dust grains and

assuming that both the grain charge and the background plasma do not evolve in time. Such a deduction is possible because in realistic experiments, the charging time of dust grains are typically three orders of magnitude smaller than the inverse dust plasma frequency (Morfill and Ivlev, 2009; Fortov et al., 2005). In reality, the dust grains in a complex plasma can have a size (and hence charge) distribution (Verheest and Meuris, 1996), nevertheless, the size of grains are typically 2-3 orders smaller compared to Wigner Seitz radius. Thus, in the present thesis, we drop such size distribution and take point masses for grains forming the Yukawa liquid. Assuming a Boltzmann distribution of ions and electrons which provides a screening to the massively charged dust grains, the grain dynamics can then be modeled by a Yukawa (screened Coulomb) potential:

$$U(r) = \frac{Q^2}{4\pi\epsilon_0 r} e^{-r/\lambda_D} \quad (2.1)$$

where r is the radial distance between any two dust grains and Q is the charge on the dust grain. The Debye length of the background plasma is given as

$$\lambda_D = \left(\frac{q_i^2 n_i}{\epsilon_0 k_B T_i} + \frac{e^2 n_e}{\epsilon_0 k_B T_e} \right)^{-1/2} \quad (2.2)$$

where q_i, n_i and T_i are the charge, mean density and temperature of plasma ions, and $-e, n_e$ and T_e are the corresponding quantities for plasma electrons. The force corresponding to $U(r)$ is

$$\mathbf{f} = -\nabla U(r) \quad (2.3)$$

so the force that grain j exerts on grain i is

$$\mathbf{f}_{ij} = \frac{Q^2}{4\pi\epsilon_0 r_{ij}^2} \left(\frac{1}{r_{ij}} + \frac{1}{\lambda_D} \right) e^{-r_{ij}/\lambda_D} \mathbf{r}_{ij} \quad (2.4)$$

where $\mathbf{r}_{ij} = \mathbf{r}_i - \mathbf{r}_j$ and $r_{ij} = |\mathbf{r}_{ij}|$. The equations of motion follow from

Newton's second law,

$$m\ddot{\mathbf{r}}_i = \mathbf{f}_i = \sum_{\substack{j=1 \\ (j \neq i)}}^N \mathbf{f}_{ij} \quad (2.5)$$

In presence of dust neutral collisions, the above equation becomes

$$m\ddot{\mathbf{r}}_i = \sum_{\substack{j=1 \\ (j \neq i)}}^N \mathbf{f}_{ij} + m\nu_{dn}\dot{\mathbf{r}}_i \quad (2.6)$$

where ν_{dn} is the Epstein drag coefficient due to the neutral gas (Epstein, 1924). The sum is over all N dust grains in the liquid, excluding i itself, and m is the grain mass. Such an N -body problem must be numerically integrated in an MD simulation. It is easily seen from Equation 2.5 that the amount of computational work is proportional to $N(N-1)/2$, if one wishes to solve the N -body problem by a brute force method. In order to keep the computation to a reasonable level, the interaction is truncated at a distance $r_c = 20$ [in MD units, Section (2.2)]. At this cutoff distance the ratio $U(r_c)/U(1) \approx 10^{-6}$, hence, in the calculation of forces from Equation 2.4, it is reasonably justified to exclude all pairs having a separation greater than r_c . It should be noted that in order to use this cutoff distance r_c , the system size must be large enough i.e $L/r_c \geq 4$. Hence we do not use a cutoff distance for the phase transition studies reported in this chapter and use it only in subsequent chapters on large scale flows.

2.2 Dimensionless units

If n denotes the volume grain density, then in 3D, the mean intergrain separation can be expressed in terms of the Wigner-Seitz radius $a = [3/(4\pi n)]^{1/3}$. Physical quantities can then be expressed in dimensionless units by making

the following replacements for distance, energy and time:

$$r \rightarrow ra \quad (2.7)$$

$$U \rightarrow U \frac{Q^2}{4\pi\epsilon_0 a} \quad (2.8)$$

$$t \rightarrow t\sqrt{3}\Omega_{pd}^{-1} \quad (2.9)$$

where a , $[Q^2/(4\pi\epsilon_0 a)]$ and $\sqrt{3}\Omega_{pd}^{-1}$ are the MD units of length, energy and time respectively. Thus, the Yukawa potential (Equation 2.1) can be written in MD units as

$$U(r) = \frac{e^{-\kappa r}}{r} \quad (2.10)$$

and the corresponding equation of motion (Equation 2.5) becomes

$$\ddot{\mathbf{r}}_i = \sum_{j \neq i} \left(\frac{1}{r_{ij}} + \kappa \right) \frac{\mathbf{r}_{ij}}{r_{ij}^2} e^{-r_{ij}\kappa} \quad (2.11)$$

where $\kappa = a/\lambda_D$ is the screening parameter. The parameter κ governs the nature of interaction between the dust grains; i.e complex plasma can behave like a *Coulomb gas* ($\kappa \rightarrow 0$) or like an *ideal gas* ($\kappa \rightarrow \infty$). The dimensionless kinetic and potential energies per grain can thus be written as

$$E_k = \frac{1}{2N} \sum_{i=1}^N \mathbf{v}_i^2 \quad (2.12)$$

$$E_{pot} = \frac{1}{N} \sum_{1 \leq i < j \leq N} \frac{e^{-\kappa r_{ij}}}{r_{ij}} \quad (2.13)$$

where \mathbf{v}_i is the velocity. The functional form of Yukawa potential (Equation 2.10) for various values of screening parameter is shown in Figure 2.1. The unit of temperature is $Q^2/(4\pi\epsilon_0 a k_B)$, and since each translational degree of freedom contributes to $k_B T/2$ to the kinetic energy, the temperature of a

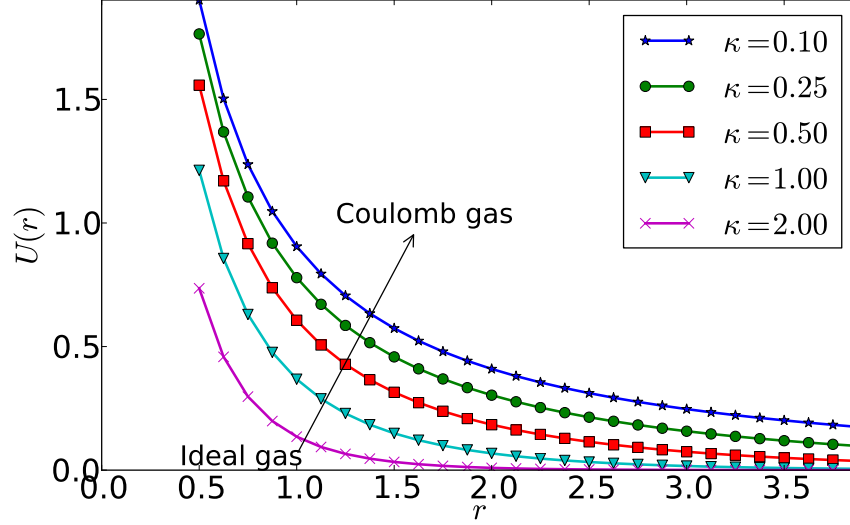


Figure 2.1: Yukawa potential in MD units for various values of screening parameter κ . As κ decreases, grain interaction becomes long ranged and one can observe Coulomb gas behavior. At higher κ , one recovers the short ranged ideal gas behavior.

d -dimensional ($d = 2$ or 3) system is

$$T = \frac{1}{d(N-1)} \sum_i^N \mathbf{v}_i^2 \approx \frac{1}{dN} \sum_i^N \mathbf{v}_i^2 \quad (2.14)$$

Strictly speaking, of the total dN degrees of freedom, d are eliminated because of momentum conservation, but if N is large, this detail can be safely ignored. The extent of strong coupling is quantified by the coupling parameter $\Gamma = Q^2/(4\pi\epsilon_0 k_B T)$. Hence, $\Gamma \gg 1$ denotes the strong coupling regime and $\Gamma \rightarrow 1$ denotes the weak coupling regime. The thermodynamic state of a Yukawa liquid can be fully described by the two dimensionless parameters: κ and Γ . In the following section we discuss the boundary conditions used in a typical MD simulation of the present thesis.

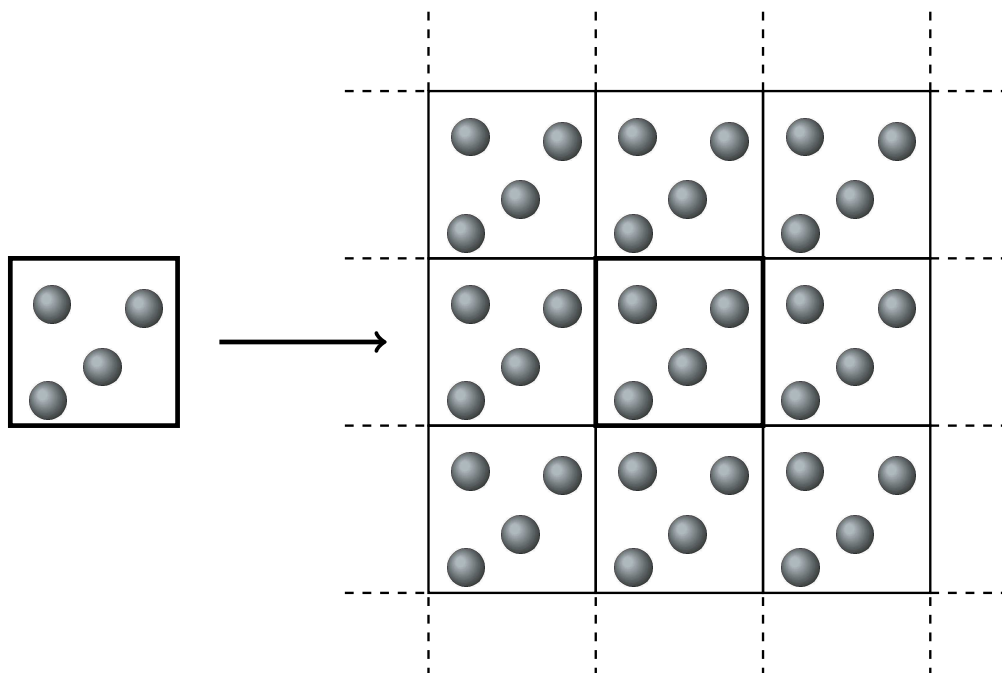


Figure 2.2: A schematic diagram showing the implementation of periodic boundary conditions (for clarity, the two-dimensional case is shown)

2.3 Boundary conditions

Finite and infinite systems can behave in a very different manner (Salacuse et al., 1996). In a realistic experimental scenario, boundary effects such as particle-wall collisions can play an important role in the overall dynamics. Nevertheless, in systems of macroscopic size, only a very small fraction of the particles is close to a wall to experience any deviation from the bulk in the interior of the system. For example, in a 3D system with N particles, the number of particles close to the walls is rough $N^{2/3}$. In a typical small scale MD simulation, with $N = 1000$, roughly 500 atoms are immediately close to the walls, leaving only a few in the interior. Thus the simulation fails to capture the typical state of particles in the bulk and results obtained are no longer valid.

One can construct a bounded system but free of physical walls by implementing periodic boundary conditions (PBC) as shown in Figure 2.2. The

introduction of PBC is equivalent to considering an infinite space-filling array of identical copies of the bounded simulation region. The consequences of implementing such PBC are twofold: (a) Any particle which leaves the simulation region through a particular face immediately reenters the region through the opposite face, and (b) Any particle in the simulation region interacts only with the closest periodic images of the other $N - 1$ particles, an effect called minimum image convention (MIC) (Rapaport, D. C., 1995; Allen and Tildesley, 1999). Hence, by implementing PBC, one essentially removes all physical boundaries and effectively simulates a spatially homogeneous system. A typical pseudo code for implementing PBC along \hat{x} on any particle i is given below,

$$x[i] = x[i] - L * \mathbf{rint}(x[i]/L)$$

where \mathbf{rint} is a ‘‘C’’ function which rounds the argument to an integer value in floating-point format. The pseudo code for implementing MIC for an i, j pair is given as follows

$$r = (x[i] - x[j]) - L * \mathbf{rint}((x[i] - x[j])/L)$$

It should be noted that in presence of PBC, long range forces resulting from the Yukawa potential need to be properly handled as the forces cannot be truncated without incurring serious error; they continue to act between the periodic replicas as well. The Ewald technique (see appendix A.3) eliminates the discontinuity arising from truncated long-range forces in presence PBC and is used in MPMD whenever necessary.

2.4 Initial state

A particularly simple choice for an initial state is to start with particles on the sites of a regular lattice (face centered cubic fcc, body centered bcc or simple cubic scc). The site spacing needs to be adjusted to generate the desired density. The initial velocities are then assigned random directions

with a fixed magnitude based on the initial temperature. Care needs to be taken such that the center of mass of the whole system is at rest thereby eliminating any overall flow (Rapaport, D. C., 1995). Once the initial state is generated, the simulation can be performed under either “microcanonical” (N, V, E) or “canonical” (N, V, T) conditions. The latter being the case when the system is connected to a thermostat (see appendix A.1) throughout the simulation.

2.5 Integration

Integration of the equations of motion can be achieved by various numerical techniques. We have used a Leapfrog integrator which calculates positions and velocities at interleaved time points, in such a way that they “leapfrog” over each other. For example, the position is known at integer time steps and the velocity is known at integer plus half time steps.

If $h = \Delta t$ denotes the size of the timestep used for numerical integration, then the integration formulae applied to each components of a particle’s position and velocity are:

$$v_{xi}(t + h/2) = v_{xi}(t - h/2) + ha_{xi}(t) \quad (2.15)$$

$$r_{xi}(t + h) = r_{xi}(t) + hv_{xi}(t + h/2) \quad (2.16)$$

It is clear from Equation 2.16 that if the velocity of a particle is required at a time t when the positions are already known, then Equation 2.17 can be used.

$$v_{xi}(t) = v_{xi}(t - h/2) + (h/2)a_{xi}(t) \quad (2.17)$$

It should be noted that the local errors introduced at each timestep due to the truncation of the infinite series are of order $O(h^4)$ for the coordinates and $O(h^2)$ for the velocities. Having discussed the basic elements of a MD algorithm, we now present a discussion on the MD code used in the present thesis. Several diagnostics are developed and elucidated through a nonequilibrium

test problem.

2.6 MPMD code

Multi **P**otential **M**olecular **D**ynamics (MPMD) code is a parallel MD code capable of simulating both pair-wise and many body force fields. Presently the modules available are Lennard Jones, Yukawa and Tersoff-Brenner potentials. When the system size is small, Ewald sums (see appendix A.3) are employed to handle long ranged forces in presence of periodic boundaries. MPMD can simulate various thermodynamic ensembles such as NVT , NVE and NPT by employing a Gaussian thermostat (see appendix A.1) and a Andersen barostat (see appendix A.2). Before we discuss the test problem, it is worthwhile to discuss some algorithms implemented in MPMD for achieving speed up.

2.6.1 Performance

It was seen from Equation 2.5 that the computation of force goes as N^2 . Thus it becomes extremely important to look for algorithmic improvements over the traditional brute force method. The simplest way to speedup force computation is to implement the Verlet neighbor list (Verlet, 1967), which basically amounts to computing pair interactions only when the interparticle separation is within a certain value r_l (r_l is little more than the “cut-off” distance r_c). This is done by generating, for each particle, a list of particles that are within a spherical shell. The list is updated at frequent intervals whenever sum of the magnitudes of the two largest displacements exceeds $r_l - r_c$ (Fincham and Ralston, 1981). Even with such a neighbor list, the performance saturates once the system size increases towards 1000 particles as the conventional neighbor list becomes too large to store easily, and the logical testing of every pair in the system is inefficient. As an alternative, one can consider the cell subdivision method for large systems. The cubic periodic box is divided into a lattice of $M_1 \times M_2 \times M_3$ cells. A two dimensional analog of this is shown in Figure 2.3. The size of each cell is chosen such

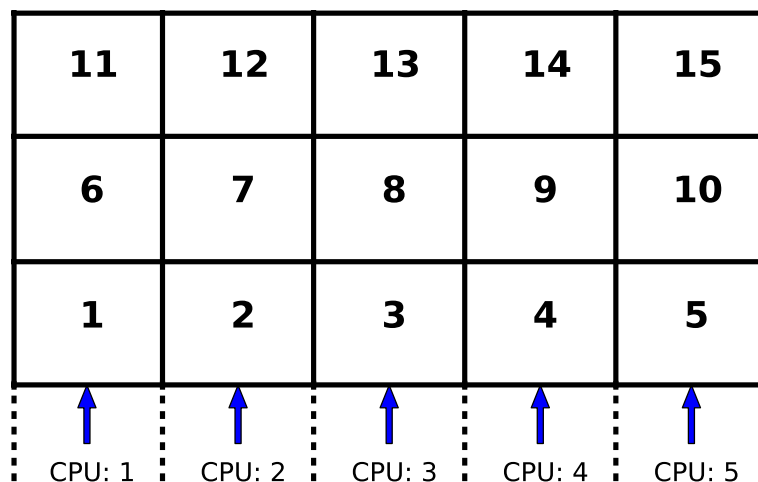


Figure 2.3: The parallel cell subdivision method. For simplicity, we show the method in two dimensions (can be easily extended for three dimensional case). Parallelism is achieved by first decomposing the simulation domain into $M_1 \times M_2$ cells ($M_1 = 5, M_2 = 3$). After this, each column (containing 3 cells) is then allocated to a single CPU. In the example shown here, we thus require only 5 CPU to implement parallelism.

that $(L/M_{1,2,3})$ is greater than the cut-off distance for the Yukawa forces. For the two dimensional case as shown in Figure 2.3, the neighbors of any particle in cell 8 are to be looked at the cells 2, 3, 4, 7, 8, 9, 12, 13 and 14. For the two dimensional case shown in Figure 2.3, there are approximately $N_c = N/(M_1 M_2)$ particles in each cell and thus we need to only examine $9NN_c$ pairs. This contrasts with the brute force (N^2) approach shown in Equation 2.5. Parallelization is easily achieved through a domain decomposition technique. Here each column containing three cells is loaded onto a separate CPU (processor) and the updated particle coordinates after the trajectory integration are broadcasted to all the slave CPU's at the end of a given time step.

This cell structure can be used by the method of linked lists (Knuth, 1973; Hockney and Eastwood, 1992; Allen and Tildesley, 1999). The first part of the method involves sorting all the molecules into their appropriate cells at every timestep. One creates two arrays namely the “head-of-chain”

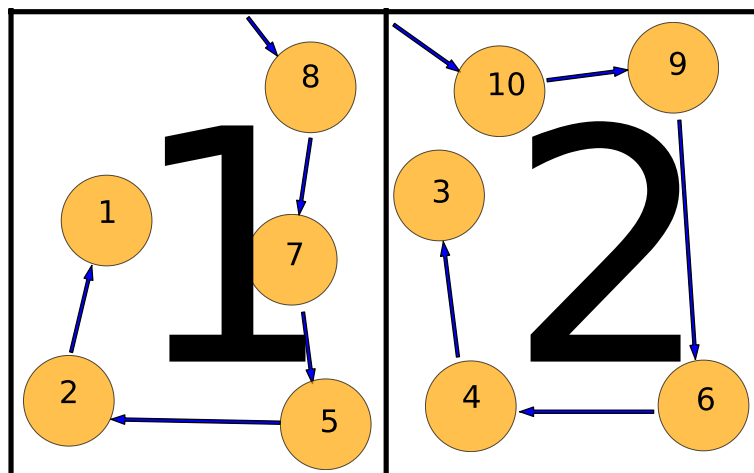


Figure 2.4: A close up of cells 1 and 2, showing the molecules and the linked list structure (Allen and Tildesley, 1999)

array **HEAD** and the “linked-list” array **LIST**. Each element of the array **HEAD** corresponds to a specific cell. This element basically contains the index number of one of the particles in that cell. This index number is then used to address the element of the array **LIST**, which contains the index number of the next molecule in that cell. Thus, the **LIST** array element for that particle is the index of the next molecule in that cell, and so on. Upon following the path of linked-list targets, one will eventually reach an element of **LIST** which is zero. This indicates that there are no further particles in that cell, and we move on to the head-of-chain particle for the next cell. To illustrate this searching mechanism, we choose two cells namely ‘1’, containing particles: 1, 2, 5, 7, 8 and the cell ‘2’ containing particles: 10, 9, 6, 4, 3 (see Figure 2.4). The schematic allocation of the arrays **HEAD** and **LIST** for referencing particles in cell ‘2’ is shown in Figure 2.5. The parallel cell subdivision discussed here is incorporated in the MPMD code. In the following subsection we undertake a test problem, namely, to study the effect of a small external drive on a strongly coupled Yukawa solid (Ashwin and Ganesh, 2009).

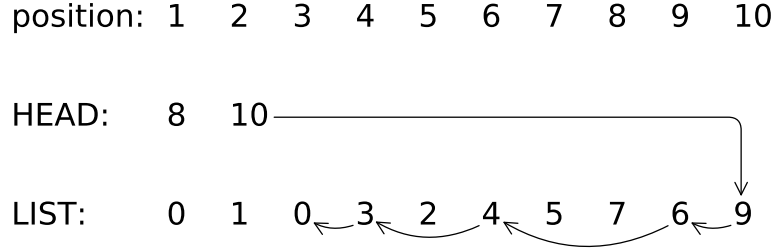


Figure 2.5: For cell 2, $\text{HEAD}(2) = 10$, and the entire path through the linked list is indicated with the help of arrows (Allen and Tildesley, 1999)

2.6.2 Driven Yukawa system

In a ground based laboratory experiment, a strongly coupled complex plasma can exist in a two dimensional crystalline form (Morfill and Ivlev, 2009). It should be noted that the confinement of dust grains in such an experiment is achieved through the balance of gravity and external electric fields. Hence, it is natural to expect that a complex plasma can form different structures other than the regular fcc and bcc structures under the effect of these confining forces. In the past, melting of dusty plasma crystals in presence of spatially random and time varying external fields have been studied by (Hoffmann and Lowen, 2000) using Fokker-Planck dynamics. In contrast to that work, we investigate, as a test problem for MPMD code, the effect of a small external drive on a Yukawa solid through nonequilibrium MD simulations. It will be seen in the following sections that such a small perturbation on a physical system near a solid-liquid phase boundary can lead to drastic changes in its structure. Thus, neglecting ion streaming effects and dust neutral collisions ($\nu_{dn} = 0$), a 3D Yukawa solid (bcc) at $\kappa = 1.0, \Gamma = 210$ is subjected to a small external drive at the largest possible scale (see Figure 2.6). This drive has the general form

$$V_E = V_0 \cos(k_L z) \Theta(t - t_0) \quad (2.18)$$

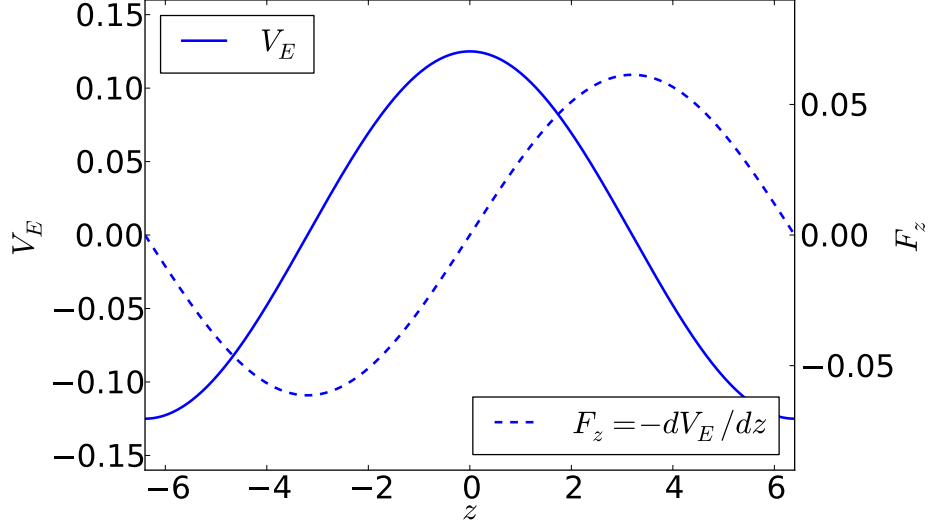


Figure 2.6: The external potential V_E applied along \hat{z} direction, and the corresponding force $F_z = -\frac{dV_E}{dz}$: The cubic simulation box is centered at the origin with the edge length $L = 12.8$. The spatial profile of potential drive is such that the force acting on any particle is always away from the center. Left y-axis shows the potential drive and right y-axis shows the force in reduced units. It should be noted that $V_0/E_{pot} \leq 0.25$, hence the external drive is much smaller compared to average intergrain potential energy.

where $\Theta(t - t_0)$ is a Heaviside step function in time at $t = t_0$ and $k_L = 2\pi/L$, L being the size of the system; V_0 is considered small compared to average inter-particle potential energy. The resulting force from this drive acts along \hat{z} and is given as

$$F = -\frac{dV_E}{dz} \hat{z} = V_0 k_L \sin(k_L z) \Theta(t - t_0) \hat{z} \quad (2.19)$$

For the present study, we have chosen the value of $\Gamma = 210$ as it is close to the liquid-solid phase boundary [see Figure 2.7]. We recall that the length, energy and time are normalized to a , $[Q^2/(4\pi\epsilon_0 a)]$ and $\sqrt{3}\Omega_{pd}^{-1}$ respectively. The number of particles taken in the 3D simulation is 432 and the cubic box has an edge length $L = 12.8$. This gives us a mean number density $n = 0.206$. The time step taken in the MD simulation $\Delta T = 0.001$. As the system taken is smaller compared to the typical cutoff distance $r_c \approx 20$ for a Yukawa

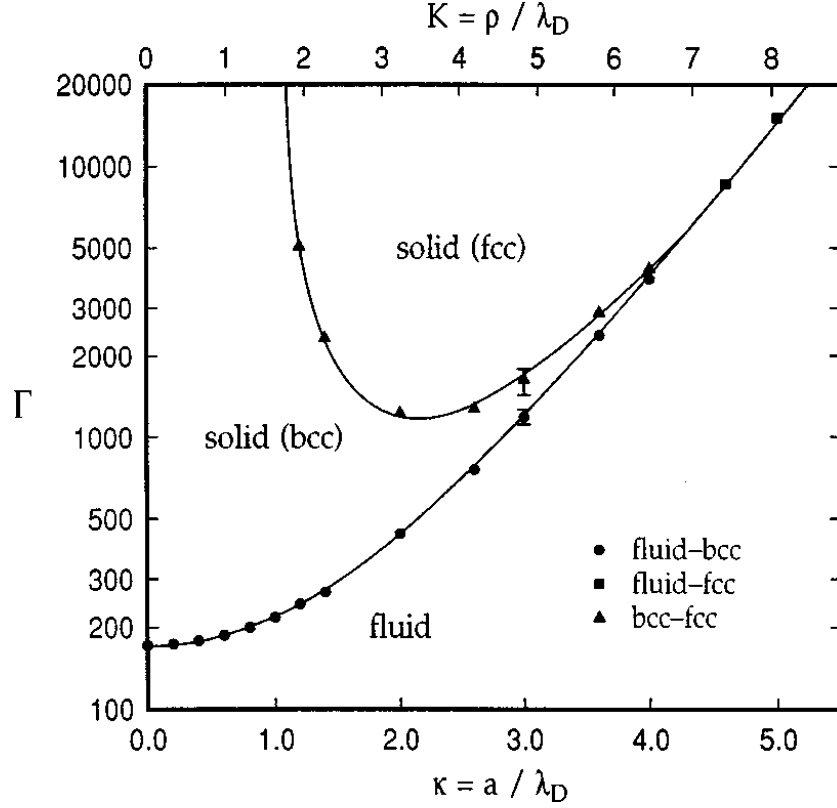


Figure 2.7: Phase diagram of a Yukawa system (Hamaguchi et al., 1997). It is clear that our chosen value of bcc solid at $\Gamma_0 = 210$, $\kappa = 1$ is close to the liquid-solid phase boundary.

potential at $\kappa = 1$, we avoid using the cutoff distance and calculate forces between all pairs. Such a brute force method corresponds to evaluating forces between $N(N - 1)/2$ pairs for an N particle system. Due to the small size of the system, we have used the serial version of the MPMD code for the present problem. The simulation is carried out in following steps (shown in Figure 2.8):

- (a.) *Canonical Run* ($0 \leq t < 350$): First we perform canonical ensemble M.D. for $3.5 \times 10^5 \Delta t$ to take the system to a thermal equilibrium at required $\Gamma = 210$, by connecting it to a Gaussian thermostat (see appendix A.1).
- (b.) *Micro-canonical Run* ($350 \leq t < 700$): After step (a), we remove the thermostat and do a micro-canonical M.D. for $3.5 \times 10^5 \Delta t$ where the system

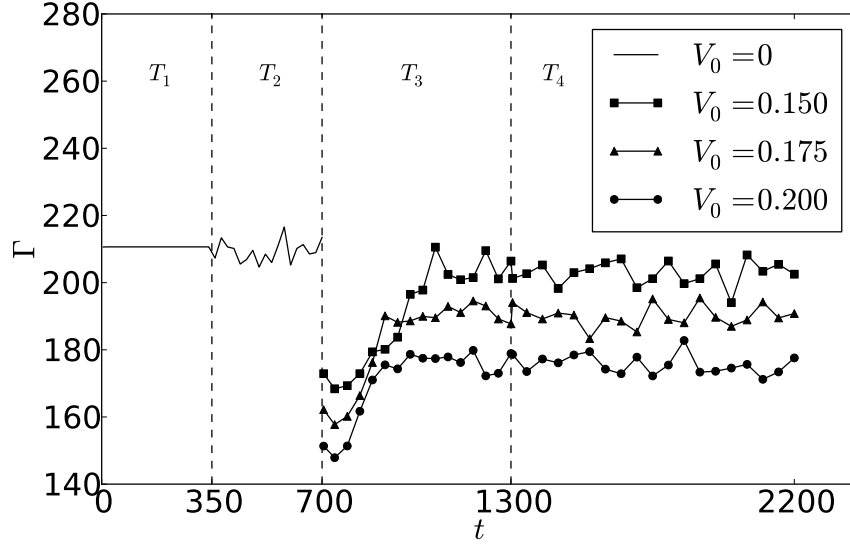


Figure 2.8: The plot of Γ as a function of time for various values of V_0 . It should be noted that the solid-liquid phase boundary line for $\kappa = 1$ is around $\Gamma \sim 185$ (Hamaguchi et al., 1997). Timezones shown are, T_1 : Canonical Run, T_2 : Micro-canonical Run, T_3 : Transient Phase and T_4 : Final Equilibrium.

finds a new thermal equilibrium very close to the Γ set in step (a). At this stage measurements with $V_0 = 0$ are taken.

(c.) *Transient Phase* ($700 \leq t < 1300$): At the end of step (b) (and the thermostat decoupled), the external drive is turned on and the system goes through transient phase where the temperature of the system changes. Measurements in non-equilibrium conditions is done during this phase.

(d.) *Final Equilibrium* ($1300 \leq t < 2200$): We continue the simulations after step (c) till the transients die and the final equilibrium is reached. At this stage equilibrium measurements with $V_0 \neq 0$ are taken. In the following subsections we will present some important diagnostics to reveal the phase transition of Yukawa solid due to the external drive.

2.6.3 Radial distribution function

As is well known, fluid state is characterized by the lack of permanent structure. Structural correlations can be measured in laboratory experiments and

such details can provide important information about the average molecular organization in a liquid (McQuarrie, D. A., 1976). One such structural correlation is the pair-distribution function:

$$g(\mathbf{r}_1, \mathbf{r}_2) = \frac{N(N-1) \int \exp[-U(\mathbf{r}_1, \dots, \mathbf{r}_N)/(k_B T)] d\mathbf{r}_3 \dots d\mathbf{r}_N}{n^2 \int \exp[-U(\mathbf{r}_1, \dots, \mathbf{r}_N)/(k_B T)] d\mathbf{r}_1 \dots d\mathbf{r}_N} \quad (2.20)$$

where the integral in the denominator is just the partition function and the integral in the numerator differs only in that the coordinates \mathbf{r}_1 and \mathbf{r}_2 are excluded from the integration. For spatially homogeneous systems only the relative separation between the particles is meaningful, which readily leads to the sum over atom pairs:

$$g(\mathbf{r}) = \frac{2V}{N^2} \left\langle \sum_{i < j} \delta(\mathbf{r} - \mathbf{r}_{ij}) \right\rangle \quad (2.21)$$

For isotropic systems, Equation 2.21 can be averaged over all angles (radially) without any loss of information. The result is the radial distribution function (RDF) - a function which describes the spherically or radially averaged local organization around any given particle. Hence $ng(r)d\mathbf{r}$ is proportional to the probability of finding a particle in the volume element $d\mathbf{r}$ at a distance \mathbf{r} from a given particle. RDF plays a fundamental role in liquid state physics, mainly in describing the observables depending only pair separation such as potential energy and pressure. In the study of phase transitions, RDF plays an additional important role as it can show the onset of solid state with the introduction of additional peaks in its profile.

Following Equation 2.21, one can deduce a histogram representation of $g(r)$ using discrete pair separations (Rahman, 1964). If h_k is the number of pairs (i, j) for which $(k-1)\Delta r \leq r_{ij} < k\Delta r$ and $r_k = (k-1/2)\Delta r$, then assuming that Δr is sufficiently small, we have

$$g(r_k) = \frac{V h_k}{2\pi N^2 r_k^2 \Delta r} \quad (2.22)$$

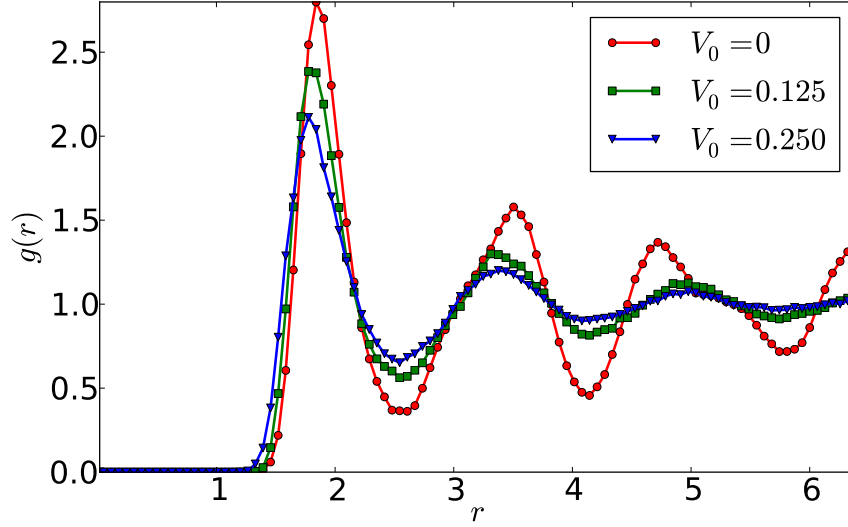


Figure 2.9: RDF or $g(r)$: The fall in the peaks of $g(r)$ is clearly seen with varying amplitudes of external drive V_0 . The oscillations in $g(r)$ even for larger values of V_0 indicate that the transition is from solid state to a strongly coupled liquid state.

where $r_k = (k - 1/2)\Delta r$. The two dimensional version is

$$g(r_k) = \frac{Ah_k}{\pi N^2 r_k \Delta r} \quad (2.23)$$

The normalization factors ensure that $g(r \rightarrow \infty) = 1$, even though in presence of periodic boundaries, one cannot measure $g(r)$ beyond half the smallest edge of the simulation box (Rapaport, D. C., 1995). Spherically averaged $g(r)$ for various values of external drive V_0 is shown in Figure 2.9. For $V_0 = 0$, $g(r)$ is measured after the system has reached equilibrium, and for $V_0 \neq 0$, measurements are taken when the system has reached equilibrium in the presence of the external drive. As V_0 increases, the peaks in $g(r)$ decrease which shows the loss of long-range positional order as the system goes towards the liquid state. For $V_0 = 0.125$ the first peak in $g(r)$ falls by about 18 %, and at $V_0 = 0.250$ it falls by 25%. In the following we discuss this solid-liquid phase transition from the viewpoint of lattice correlation.

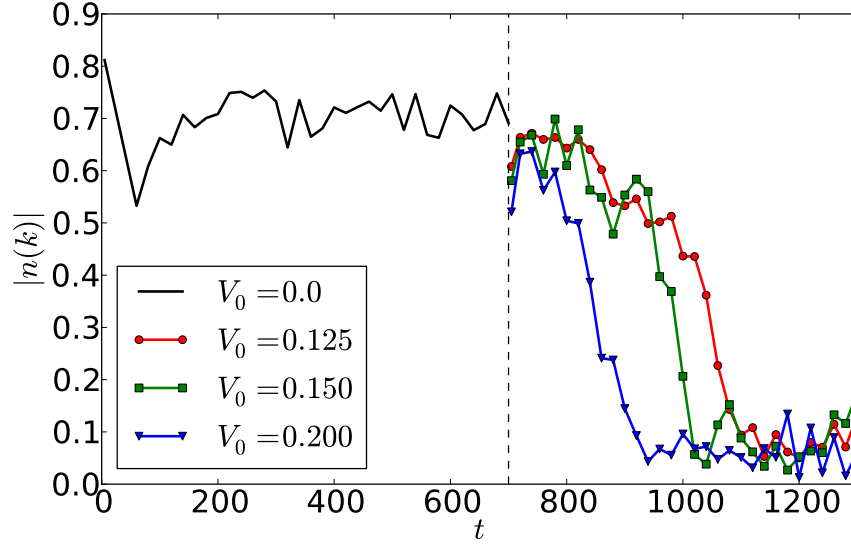


Figure 2.10: Lattice correlation ($|n(\mathbf{k})|$) as a function of time: The drive is switched on at $t = 700$. The fall in lattice order is clearly faster with increasing V_0 . The value of \mathbf{k} chosen is $(2\pi/l_u)(1, 0, 1)$ which corresponds to a bcc lattice

2.6.4 Lattice correlation

The RDF discussed so far gives us only a spherically averaged local organization around any particle. The drop in peak values of RDF as the external drive is applied, indirectly indicates a phase transition to a liquid state. For a direct extraction of crystalline order one needs to construct the lattice correlation which can be measured through X-ray scattering in crystalline materials (McQuarrie, D. A., 1976; Hansen and McDonald, 2006). For this, we first express the local density at a point \mathbf{r} as a sum over all atoms:

$$n(\mathbf{r}) = \sum_{j=1}^N \delta(\mathbf{r} - \mathbf{r}_j) \quad (2.24)$$

and its Fourier transform

$$n(\mathbf{k}) = \frac{1}{N} \sum_{j=1}^N \exp(-i\mathbf{k} \cdot \mathbf{r}_j) \quad (2.25)$$

To calculate $|n(\mathbf{k})|$, we take the values of \mathbf{k} as $(2\pi/l_u)(1, -1, 1)$, $(2\pi/l_u)(1, 0, 1)$ and $(2\pi/l_u)(1, 0, 0)$ for fcc, bcc and simple cubic lattices respectively. Here, l_u is the unit cell edge. In the ideal or the fully ordered case, $|n(\mathbf{k})| = 1$, but deviations $O(N^{-1/2})$ can be expected in the disordered case. The melting of the system and the loss of crystalline order with the application of external drive is seen in Figure 2.10. In the following section, we discuss the transport properties of Yukawa system in the presence of an external drive. As the system undergoes a solid to liquid transition, important changes begin to appear in transport characteristics.

2.6.5 Diffusion

In the continuum limit, mass flux is related to the density gradient by the Fick's law (McQuarrie, D. A., 1976)

$$n\mathbf{u} = -D\nabla n \quad (2.26)$$

where D is the diffusion coefficient, $\mathbf{u}(\mathbf{r}, t)$ is the local velocity and $n(\mathbf{r}, t)$ is the local density. One can then write the time evolution of the density as

$$\frac{\partial n}{\partial t} = D\nabla^2 n \quad (2.27)$$

The self diffusion coefficient in the long time limit (longer than collision intervals) is given by Einstein relation (McQuarrie, D. A., 1976)

$$D = \lim_{t \rightarrow \infty} \frac{1}{6Nt} \left\langle \sum_{j=1}^N [\mathbf{r}_j(t) - \mathbf{r}_j(0)]^2 \right\rangle \quad (2.28)$$

For systems with periodic boundaries, one needs to compute true particle displacements by removing the effects of periodic wraparound (Rapaport, D. C., 1995). There exists another route to calculate D namely through the Green-Kubo formalism (McQuarrie, D. A., 1976) which is based on the

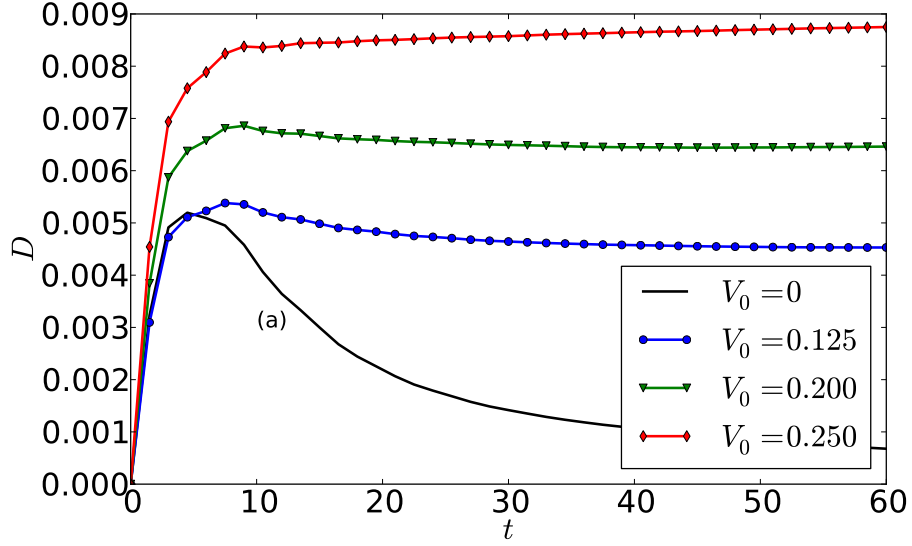


Figure 2.11: For V_0 there is no diffusion, but higher values of V_0 show that the diffusion asymptotes to larger values.

integration of velocity auto-correlation function:

$$D = \frac{1}{3N} \int_0^\infty \left\langle \sum_{j=1}^N \mathbf{v}_j(t) \cdot \mathbf{v}_j(0) \right\rangle dt \quad (2.29)$$

From Equation 2.28 we define mean-squared displacement (MSD) as

$$\langle \Delta r^2 \rangle = \frac{1}{N} \left\langle \sum_{j=1}^N [\mathbf{r}_j(t) - \mathbf{r}_j(0)]^2 \right\rangle \quad (2.30)$$

Then from 2.28 and 2.30, we get

$$\langle \Delta r^2 \rangle = 6Dt \quad (2.31)$$

The angular brackets $\langle \dots \rangle$ denote an ensemble average over 400 ensembles at equilibrium. All the measurements were done after step (b.) for $V_0 = 0$ and step (d.) for $V_0 \neq 0$ as mentioned in section 2.6.2. For liquids and gases at long times, $\langle \Delta r^2 \rangle$ goes as t and hence D asymptotes to a constant value. This constant value is called the diffusion coefficient of the system. In Figure

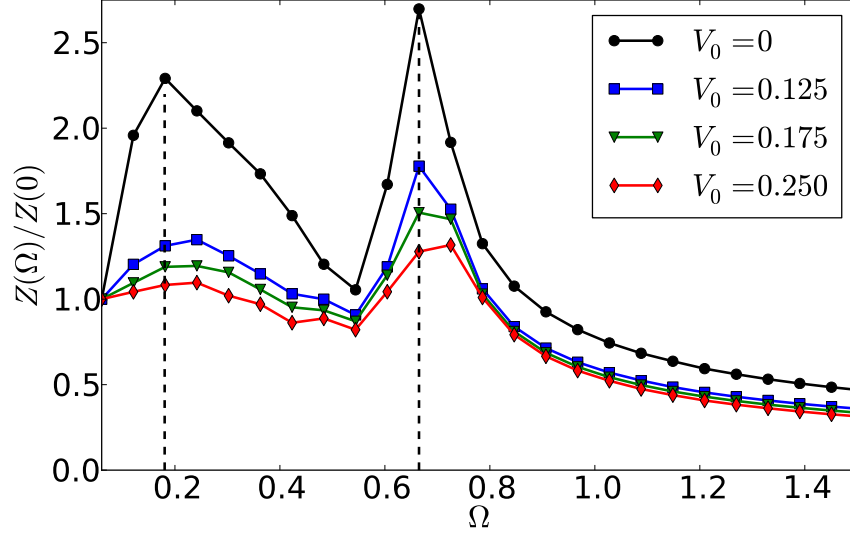


Figure 2.12: As V_0 increases the longitudinal peak at $\Omega \approx 0.67\Omega_{pd}$ (Donko et al., 2008) begins to fall. There is also a clear fall in the low frequency transversal shear peak as V_0 increases.

2.11 we show the plot of D for the Yukawa system at equilibrium. It is clear from these figures that for smaller values of V_0 , D drops close to zero (there is no diffusion). This is a characteristic of solid state. At higher values of V_0 , D asymptotes to higher values. This asymptotic nature of D is a typical characteristic of liquid state. In the following section we discuss the velocity auto-correlation and its Fourier transforms.

2.6.6 Velocity autocorrelation

Information on collective behavior (Donko et al., 2008) is contained in the velocity auto-correlation function, shown below:

$$Z(t) = \left\langle \sum_{j=1}^N \mathbf{v}_j(t) \cdot \mathbf{v}_j(0) \right\rangle / \left\langle \sum_{j=1}^N \mathbf{v}_j(0) \cdot \mathbf{v}_j(0) \right\rangle \quad (2.32)$$

The behavior of $Z(t)$ of 3D Yukawa liquids was studied at several values of Γ and κ parameters by (Ohta and Hamaguchi, 2000a). At constant κ , they found a transition from a monotonically decreasing $Z(t)$ into an oscillating

type when Γ was increased. The Fourier transform of $Z(t)$ is given below:

$$Z(\Omega) = \frac{1}{2\pi} \int_{-\infty}^{\infty} Z(t) \exp(i\Omega t) dt \quad (2.33)$$

The above integral is approximated as a discrete sum and calculated via fast Fourier transform (FFT) of $Z(t)$

$$Z(\Omega) = \sum_{n=0}^{N-1} Z(t_n) \exp(i\Omega t_n) \Delta t \quad (2.34)$$

The power spectrum of $Z(\Omega)$ for various values of V_0 are plotted in Figure 2.12. In the strong coupling regimes ($\Gamma = 210$), the power spectrum of $Z(\Omega)$ shows a collective peak near plasmon frequency at $\Omega \approx 0.67\Omega_{pd}$ as shown in previous works (Donko et al., 2008). There is another prominent peak near a low, non zero frequency. To explain this peak Hansen, Mc Donald and Pollock attempted to give a unified description of the velocity auto-correlation function in the liquid regime using the memory function formalism (Hansen et al., 1975). A more general approach using a mode coupling model was investigated by (Gould and Mazenko, 1975). It was shown for Coulomb liquids (Schmidt et al., 1997) that this low frequency peak at strong coupling is associated with the occurrence of transversal acoustic excitations (or shear modes) in the system. We notice two important trends here : First, the collective peak near the plasmon frequency Ω_{pd} starts to fall and second, the broad peak at low frequency which corresponds to shear modes starts to disappear. Both these observations confirm the approach to the liquid state as the external drive V_0 increases. In the following section we discuss the melting mechanism of Yukawa solid in the presence of an external drive.

2.6.7 Mechanism of melting

The applied external drive results in a force along \hat{z} with a sinusoidally varying magnitude. It is interesting to note that work done due to this directed force is being converted into random kinetic energy of particles due to collisions with nearest neighbors. Here, we attempt to give a qualitative

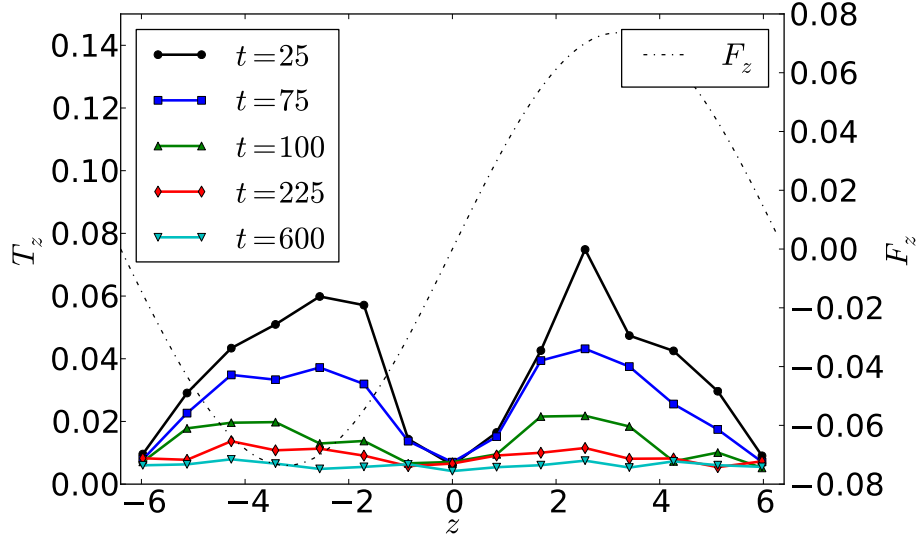


Figure 2.13: Snapshots of Temperature along \hat{z} taken at different times for $V_0 = 0.150$. The z -component of force F_z (taken on right y -axis) is plotted on top. The figure explains initial local heating in regions where magnitude of F_z is maximum.

explanation for the melting mechanism. As the external force acts only along \hat{z} (Equation 2.19), the distribution of temperature remains uniform along \hat{x} and \hat{y} directions and becomes a function of \hat{z} only. We thus define the temperature profile along \hat{z} as follows

$$T_z = \left\langle \frac{1}{N_z} \sum_i^{N_z} \frac{1}{2} v_i^2 \right\rangle \quad (2.35)$$

where N_z is the number of particles in one of the slabs along \hat{z} and $\langle \dots \rangle$ denotes the time average. At the instant when the external drive is turned on local hot zones are created where the magnitude of forces is maximum (see Figure 2.13). These hot zones give heat to the neighboring region and the system heats up. At the beginning of the transient phase the two humps in the temperature are clearly seen. These humps vanish towards the end of the transient phase. In Figure 2.13, we show the temperature profile (T_z) along \hat{z} for the case $V_0 = 0.150$. It was shown in the Figure 2.10 that the fall of lattice correlation ($|n(\mathbf{k})|$) is rapid as we increase the value of

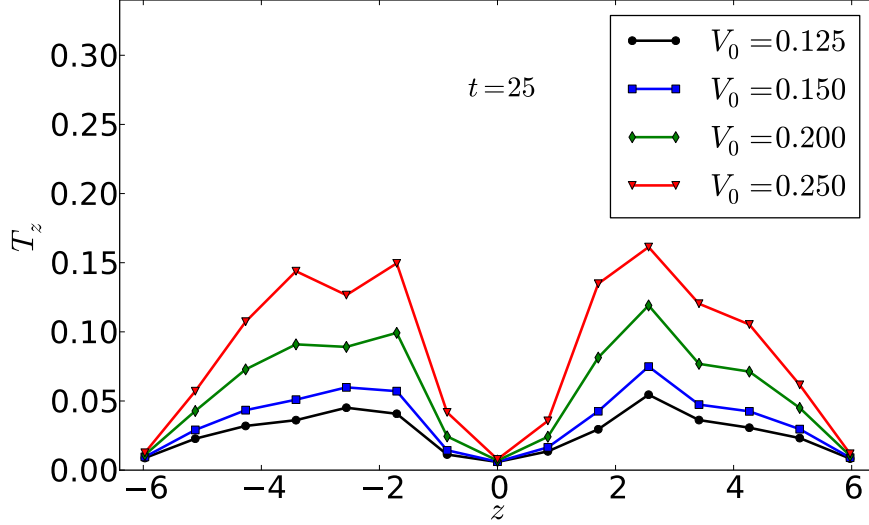


Figure 2.14: The profile of temperature along \hat{z} (T_z) very early in the run ($t = 25$) for various values of V_0 .

V_0 . We define the melting time t_m as the time in which $|n(\mathbf{k})|$ falls by an efold ($\approx 37\%$). In Figure 2.14, for a given initial temperature ($\Gamma = 210$) we show the temperature profile along \hat{z} very early in the run ($t = 25$) for different values of V_0 . The increased local heating is clearly seen with increasing values of V_0 . This qualitatively explains the decrease in melting times with increasing V_0 . In Figure 2.15, we show V_0 versus melting times for different values of initial temperatures ($\Gamma = 210$, and $\Gamma = 240$). At higher Γ , the correlations in the Yukawa system get stronger and hence it may be expected that the critical amplitude (V_0^c) is larger. This feature is clearly seen in Figure 2.15.

2.7 Summary

For the first time, through extensive equilibrium and non-equilibrium MD simulations, we studied the effect of a small external drive on 3D Yukawa systems near a solid-liquid phase boundary. Periodic boundary conditions are used along \hat{x} , \hat{y} and \hat{z} . The form of the drive chosen is $V_E = V_0 \cos(k_L z) \Theta(t -$

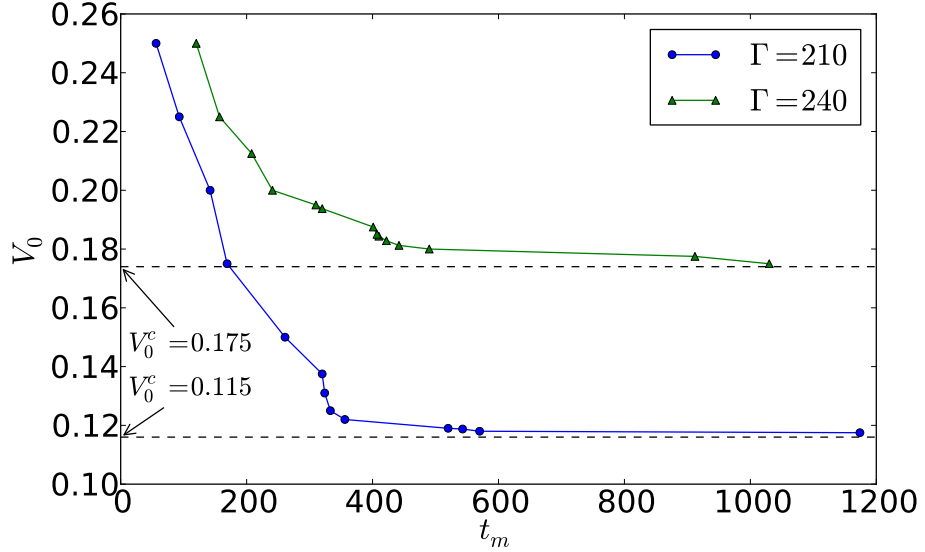


Figure 2.15: The melting time (t_m) versus V_0 for two values of initial Γ . t_m is the time during which the lattice correlation $|n(\mathbf{k})|$ fall by an efold ($\approx 37\%$). From this graph we compute V_0^c as the value at which the Yukawa solid takes infinite time to melt into a liquid. Dashed lines cut the x-axis at V_0^c . At higher Γ , value of V_0^c is higher (Ashwin and Ganesh, 2009).

t_0), where $\Theta(t - t_0)$ is a Heaviside step function in time and $k_L = 2\pi/L$, L being the size of the system. The long-range nature of the force and the periodic boundaries were properly handled by including Ewald sums (see appendix A.3). The initial state of the system of 432 particles is a regular bcc state. We then apply a small external drive and observe the melting of the system. After the initial transients die down we measure statistical properties like the self diffusion coefficient, mean square displacement and Fourier transformed velocity auto-correlation functions. The solid to liquid melting is discussed on the basis of these statistical properties and a mechanism for melting is proposed based on local heating in the system in regions where the magnitude of forces are maximum. We also qualitatively explain the decrease in melting times with the increase in magnitude of external drive V_0 . For a given (Γ, κ) pair we have found a critical amplitude of external drive V_0^c below which there is no transition. This critical amplitude (V_0^c) depends on the location of the Yukawa system in the (κ, Γ) phase space. For larger

Γ , the value of V_0^c is larger. There are several open questions such as, the effect of the external drive at multiple k_L , scaling of V_0^c with the screening parameter κ and characterizing the nature of solid to liquid transition of a strongly coupled Yukawa system. As a comparison, more rigorous potential models, such as the asymmetric Yukawa potential ([Kompaneets et al., 2009](#); [Ivlev et al., 2008](#)) can be employed to study similar phenomena.

Having studied the phase transition of a Yukawa solid into liquid state, we now focus our attention to the study of some fundamental hydrodynamic phenomena in the liquid complex plasmas. We begin our study on the fluid state with a well known hydrodynamic instability, namely the Kelvin Helmholtz instability. As, it will be seen in the following chapter, such an instability occurs when there is a sufficient velocity shear between two layers of a liquid.

Chapter 3

Parallel Shear Flows

Using “first principles” molecular dynamics simulations Kelvin-Helmholtz instability has been observed for the first time at the particle level in two-dimensional (2D) strongly coupled Yukawa liquids. We employ periodic boundary conditions as before but do not use Ewald sums as the system size is kept sufficiently large. At a given coupling strength Γ , a subsonic shear profile is superposed on an equilibrated Yukawa liquid and instability is observed. Linear growth rates computed directly from MD simulations are seen to increase with strong coupling. Vortex roll formation in the non-linear regime is reported. It is seen that at higher values of neutral gas friction, KH instability is rapidly quenched. Finally, we compare the results of “first principles” MD simulations with a generalized hydrodynamic fluid model. We now begin this chapter with a survey of fluid dynamics studies in complex plasmas and discuss some open questions therein.

3.1 Introduction

Complex plasmas can behave as essentially single phase systems when the interactions between dust grains dominate over interactions with the background medium (Khrapak et al., 2004). Thus they offer a perfect testbed for numerous fluid dynamics studies (Morfill et al., 2004; Nosenko and Goree, 2004). Some of the earliest flow studies were done by (D’Angelo and Song,

1990) who investigated the effect of static charged grains on the stability of magnetized plasma flow. Recently (Birk and Wiechen, 2002) and (Wiechen, 2006) used the conventional two fluid model and investigated the stabilizing effect of dust mass and charge on KH dust modes. As is well known, for strongly coupled liquids, kinetic theories, let alone their conventional hydrodynamic derivatives suffer from convergence and closure problems (Montgomery D.C. and Tidman D.A, 1964; Ichimaru S., 1973). As an alternative, memory dependent visco-elastic models (Berkovsky, 1992; Kaw and Sen, 1998) have been proposed which attempts to describe strongly coupled Yukawa liquids. However the validity of these models across a wide range of screening parameter and coupling strength is still an open problem (Gabor J. Kalman and Paul Carini (Eds.), 1977; G J. Kalman, M. P. Rommel and K. B. Blagoev (Eds.), 1998). Hence in order to correctly describe these systems it becomes imperative to invoke “first principles” MD simulations which amounts to numerically solving the N-body problem. In past, such exact MD simulations on short ranged Lennard-Jones systems have been carried out to obtain crucial insights into the onset, growth, non-linear saturation and transition to turbulence in Rayleigh-Taylor (Kadav et al., 2008) and Rayleigh-Bennard (Rapaport, 1988) instabilities. To our knowledge, no such “first principles” study has been undertaken in complex plasma to explore such hydrodynamic phenomena, let alone the subject of shear flows.

In this chapter we present one such study of Kelvin Helmholtz (KH) instability in a two-dimensional (2D) strongly coupled Yukawa liquid for a step shear profile. The length, time and energy are normalized are follows

$$r \rightarrow ra \tag{3.1}$$

$$U \rightarrow U \frac{Q^2}{4\pi\epsilon_0 a} \tag{3.2}$$

$$t \rightarrow t\Omega_{pd}^{-1} \tag{3.3}$$

where the a is 2D Wigner-Seitz radius given as $a = 1/\sqrt{n\pi}$, Q is the dust charge, $\Omega_{pd} = [Q^2 n / (4\epsilon_0 m a)]^{1/2}$ is dust plasma frequency, n and m are the areal number density and mass of particles respectively. For a given step

shear profile and coupling parameter ranging from $\Gamma = 1$ (weak coupling) to $\Gamma = 100$ (strong coupling), we obtain linear growth rates directly from MD simulations and observe non-linear saturation and vortex-roll formation. It should be noted that for a un-driven (flow-less) Yukawa system crystallization occurs around $\Gamma \approx 140$ at $\kappa = 0.5$ (Hartmann et al., 2005).

3.2 Initial state

We performed large scale MD simulations on a 2D system of 2.5×10^5 particles interacting via Yukawa potential. Periodic boundary conditions are employed along \hat{x} and \hat{y} . The number density of system n is 0.61, which gives us a square region of size $L = 640$. We take a cut off distance for force calculation as $r_c = 20$. Hence, we divide the 2D simulation region into $(L/r_c) \times (L/r_c)$ cells. For the present study, we use the parallel version of the MPMD code and parallel cell decomposition is implemented by loading (L/r_c) cells onto each CPU as shown in section 2.6.1. For an experimental value of $a = 0.4$ mm (Nosenko and Goree, 2004), our system size corresponds to $26 \text{ cm} \times 26 \text{ cm}$, which is typical of laboratory experiments. Hence the flows studied in the present thesis are large scale in nature. The value of screening parameter κ in all our simulations is 0.5. The initial state is prepared by first connecting the system to a Gaussian thermostat (see appendix A.1) and letting it evolve *canonically* (NVT) for $250\Omega_{pd}^{-1}$. After this we remove the thermostat and let the system evolve for another $250\Omega_{pd}^{-1}$ *micro-canonically* (NVE) at the end of which it attains a thermal equilibrium corresponding to the desired Γ . A Leap-Frog integrator with a time step $\Delta t = 0.01$ is used such that the fluctuation in total energy without the thermostat is $< 10^{-3}\%$ over an interval of $1000\Omega_{pd}^{-1}$. In Figure 3.1 we show the pair correlation function PCF or $g(r)$ obtained by MD simulations, which contains strong coupling information of the system. At higher values of coupling parameter, amplitude of the peaks increase, clearly indicating stronger coupling. The fluid limit (absence of long range order) of the system is obtained as $\Gamma \rightarrow 1$ i.e no peaks at all in $g(r)$. This increase in ordering with Γ is also confirmed by plotting particle trajectories at various Γ . In Figure 3.2, we show trajectories of 4096 particles

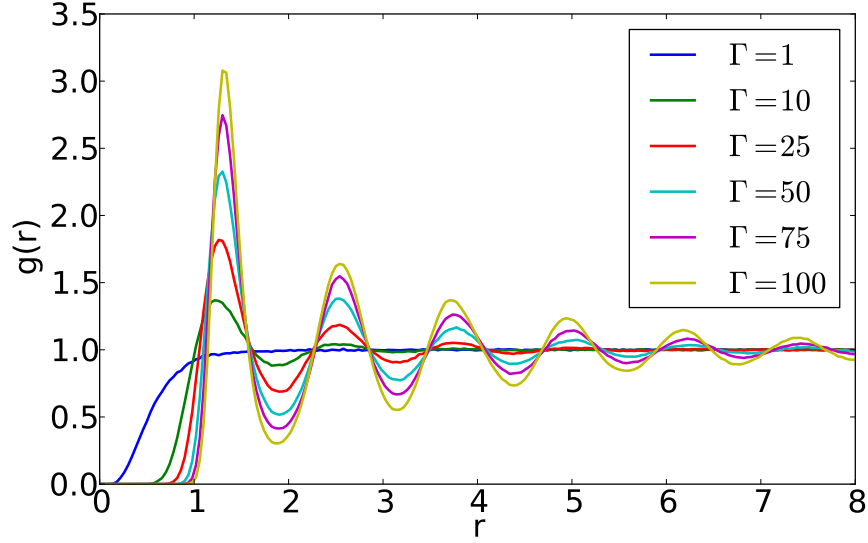


Figure 3.1: PCF vs r . Higher values of Γ show stronger coupling.

recorded over a period of $10 \Omega_{pd}^{-1}$ in a region of size 40×40 . Here one can clearly see that at the highest temperature ($\Gamma=1$), particle trajectories are diffused and the typical disordered nature of a liquid state is observed. As Γ is increased, trajectories become less diffused and the structure becomes more and more ordered.

A shear flow U is superposed on particle velocities along \hat{x} which has the following form

$$U = \begin{cases} +U_0[1 + \Delta \cos(k_x x)], & |y| \geq L/4 \\ -U_0[1 + \Delta \cos(k_x x)], & |y| < L/4 \end{cases} \quad (3.4)$$

where x, y are the components of the position vector of any particle, L is the size of the system centered at the origin $(0, 0)$ and U_0 is the magnitude of the shear velocity. In our normalized units, $U_0 = 1$, amplitude of perturbation Δ is 0.1 and $k_x = 2\pi m_n/L$, where m_n is the mode number of perturbation. The sound speed computed for our system for the entire range of Γ varies between 1.5 to 1.6. Hence the flow speed U_0 is sub-sonic and our shear flow studies can be thought of as “incompressible” in nature. To understand the

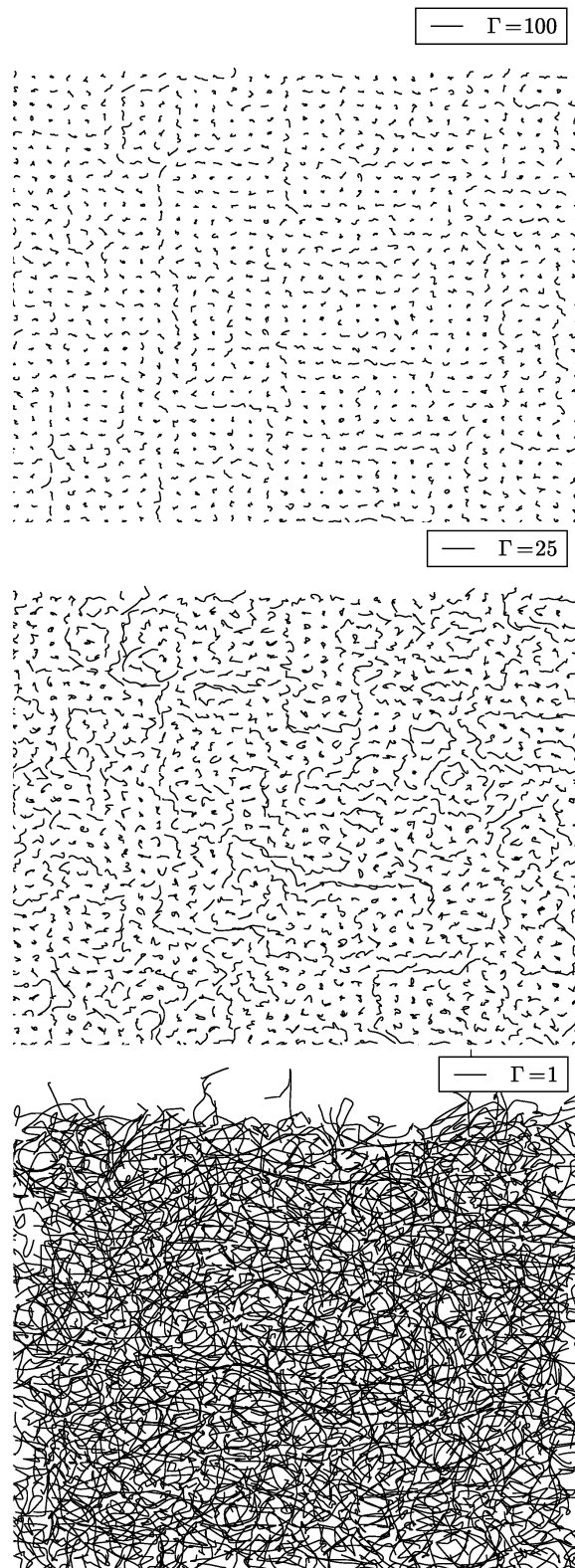


Figure 3.2: Trajectories of particles in a square region of size 40×40 (Length in units of a) at various values of Γ . At higher Γ , trajectories become more localized and solid like features are seen [Figure 3.1]

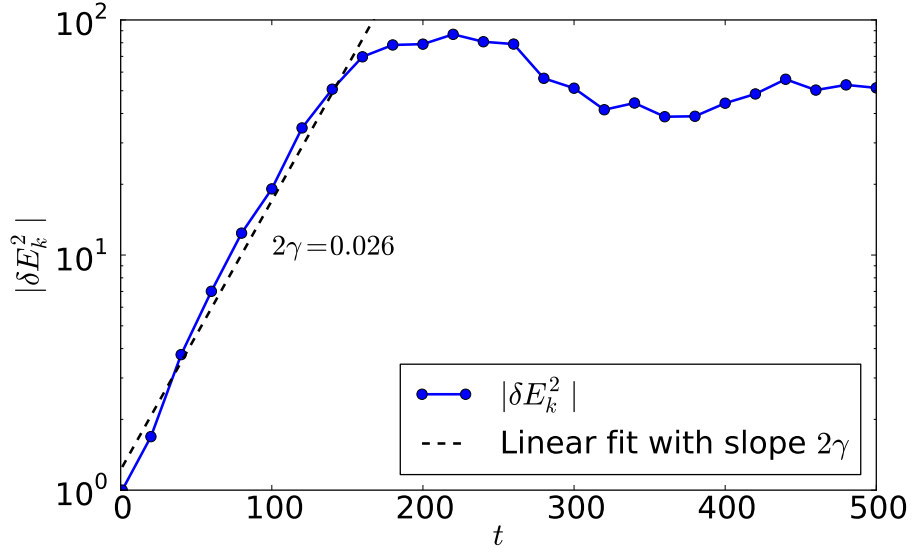


Figure 3.3: time evolution of perturbed kinetic energy along \hat{y} (Equation 3.5) on a log-linear scale for $m_n = 4$ and $\Gamma = 25$. Dashed line shows a fit to the initial linear growth regime.

growth characteristic of a particular mode m_n we study the time evolution of the perturbed kinetic energy along \hat{y} normalized to its initial value :

$$|\delta E_k^2| = \frac{\int \int (v_y(t)^2 - v_y(0)^2) dx dy}{\int \int v_y(0)^2 dx dy} \quad (3.5)$$

Figure 3.3 shows the growth of this perturbed kinetic energy for $m_n = 4$ for an initial state $\Gamma = 25$ on a log-linear scale. It is clear that the logarithm of the perturbed kinetic energy grows linearly in time leading to non-linear saturation at late times. The dashed line shows a fit to this linear growth regime. In Figure 3.4, we show the time evolution of \hat{x} independent flow velocity defined by:

$$\bar{v}_x(y) = \frac{1}{L} \int_{-L/2}^{L/2} v_x dx \quad (3.6)$$

At $t = 20$, $\bar{v}_x(y)$ has a form close to a double step profile. We then see a subsequent flattening of the step shear profile with time. The saturation of

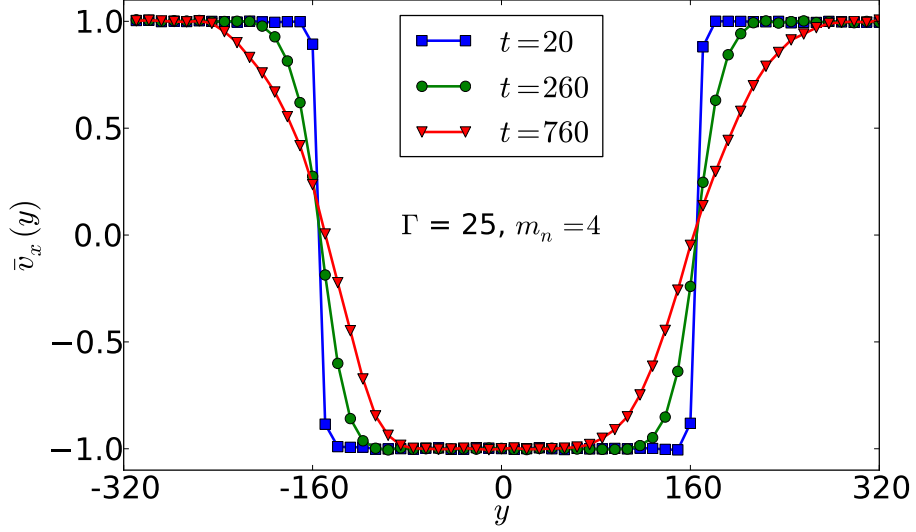


Figure 3.4: Time evolution of \hat{x} independent velocity shear profile. As the mode grows [Figure 3.3], it backreacts on the shear profile thereby flattening it. Thus the free energy source for the instability gets quenched and the mode saturates. System size $L = 640$.

the instability shown in Figure (3.3) can be interpreted from this flattening of the profile. As the mode grows, it draws energy from the free energy stored in the shear profile thereby flattening it. Thus at late times ($t \sim 200$) the free energy source for the instability gets quenched and the mode saturates.

3.3 Comparison with hydrodynamics

Analytic solution for the viscous growth rate in KH instability for a step shear profile is well known in hydrodynamics (Drazin, 1961). In our notation it reads as :

$$\gamma = \frac{k_x U_0}{3} \left[\sqrt{3} - 2 \frac{k_x}{R_E} - 2 \left[\left(\frac{k_x}{R_E} \right)^2 + 2\sqrt{3} \frac{k_x}{R_E} \right]^{1/2} \right] \quad (3.7)$$

where k_x is the dimensionless wave-number and U_0 is the dimensionless shear velocity. The Reynolds number R_E is defined as $R_E = U_0 d n / \eta$, where d is the shearing length scale and η is the shear viscosity. Using equilibrium

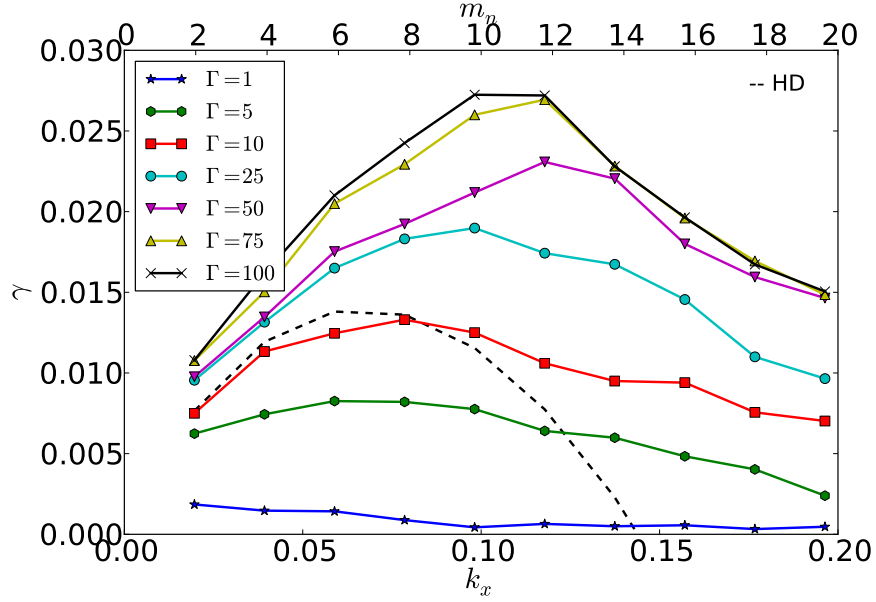


Figure 3.5: Growth rate spectra of KH instability calculated from MD. Each point on a given curve is obtained from the slope of the straight line fit to linear growth of perturbed kinetic energy. For comparison, the growth rates calculated from hydrodynamics (HD) (see Equation 3.7) at $R_E = 1$ is shown as the dashed line. Viscous stabilization is clearly seen at higher modes for all Γ .

MD simulations (Saigo and Hamaguchi, 2002) we calculate η for our system and find it to vary between 0.7 at $\Gamma = 1$ to 0.9 at $\Gamma = 100$ with a minimum ($\eta \approx 0.2$) close to $\Gamma \approx 30$. Our results for η are qualitatively similar to earlier works (Liu and Goree, 2005) (although with a different density n). Since the shearing length scale d is of the order of the inter-particle distance i.e 1 and $n = 0.61$, the conventional Reynolds number for our problem is $R_E \approx 1$. In Figure 3.5, growth rates γ (normalized to Ω_{pd}) calculated directly from MD are plotted as a function of m_n for various values of initial Γ . For comparison, the hydrodynamic growth rates calculated from Equation 3.7 at $R_E = 1$ is shown as the dashed line. As can be expected, we observe viscous stabilization at higher modes for all Γ . From Figure 3.5, it is clearly seen that growth rates at higher modes are much higher than those predicted by Equation 3.7. We believe this is due to the presence of strong correlation

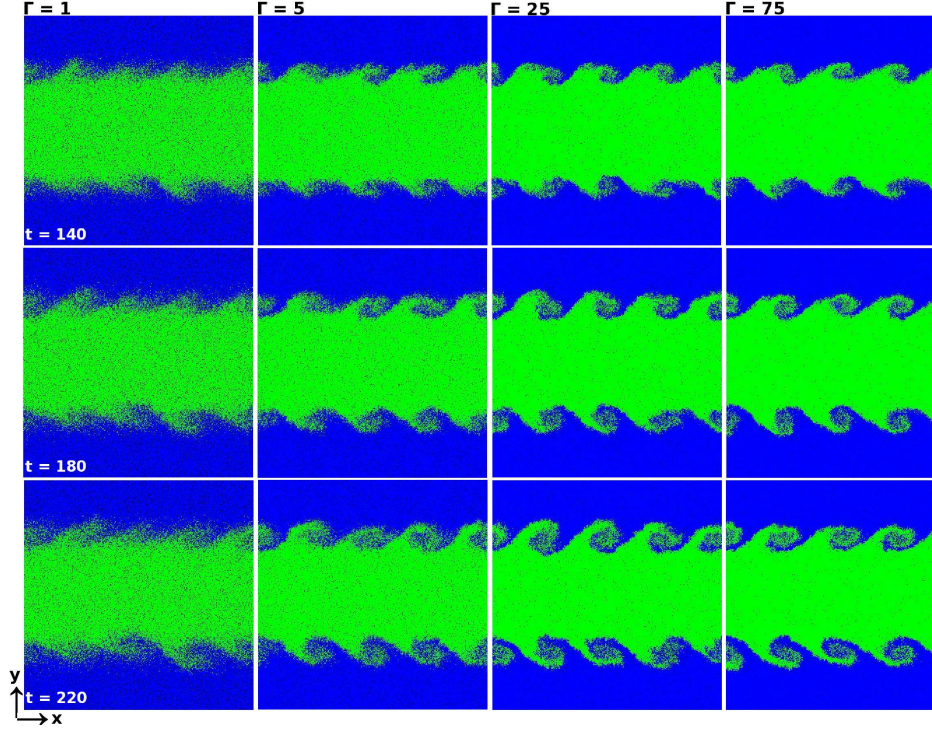


Figure 3.6: Blue colored fluid moves in the $+\hat{x}$ and green one moves in $-\hat{x}$. The snapshots are shown for the full system ($\pm L/2, \pm L/2$) at times $t = 140, 180, 220$ for four different values of Γ namely $\Gamma = 1, 5, 25, 75$ when a given mode ($m_n = 4$) is excited. Horizontal and vertical rows show snapshots at constant t and Γ respectively. At higher Γ 's, the mode structures are more prominent. It is interesting to note that at the highest temperature $\Gamma = 1$, mode structures are weak and look diffusive due high thermal agitation.

effects which manifest themselves in not only viscosity, but also long range order (oscillations in PCF as seen in Figure 3.1) and hence deviations from viscous hydrodynamics (Equation 3.7) can be expected. We also see that the maximum growth rates tend to saturate as Γ increases towards the solid regime. It will be interesting to study KH instability close to and across the liquid-solid regime ($\Gamma \approx 140$) but is beyond the scope of present work. It is interesting to note that at the weakest coupling studied i.e. $\Gamma = 1$, MD growth rates are very small ($\approx 10^{-3}$). This happens because the ratio $U_0/v_{\text{th}} \approx 0.71 < 1$. It should be noted that while U_0 is “streaming” in nature, the thermal velocity $v_{\text{th}} = \sqrt{2/\Gamma}$ is “random”. For growth rates to become

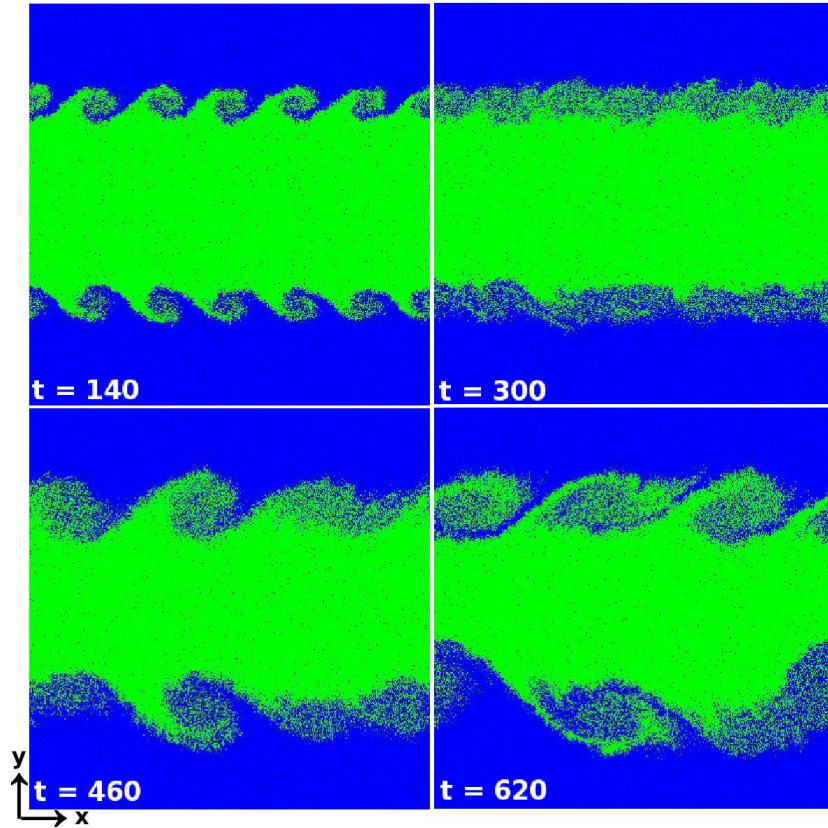


Figure 3.7: Inverse cascading of mode $m_n = 6$ starting from an initial state of $\Gamma = 50$. At $t = 140$, $m_n = 6$ appears eventually becoming $m_n = 3$ at $t = 460$. Snapshot at $t = 300$ shows an intermediate state when the initial mode $m_n = 6$ has already collapsed. Finally at $t = 620$, the definite features of mode structures are lost and the turbulent behavior of the liquid is qualitatively seen.

significant U_0/v_{th} should be > 1 . It is clearly seen from Figure 3.5 that the strong coupling effects increase the instability growth rates. This is mainly because at low temperatures (high Γ) the “streaming” effects dominate over “random” effects. It should be noted that a single run of time interval $1000\Omega_{pd}^{-1}$ takes about 28 hours on a 32 CPU parallel Linux cluster making it computationally expensive and Figure 3.5 shows the linear growth rates computed from 70 such runs.

The development of KH instability leads to the formation of vortices which eventually leads to turbulent mixing of Yukawa liquid. Figure 3.6 shows the

instantaneous snapshots of the particle coordinates to illustrate the formation of vortices. The particles are colored according to the initial shear velocity imposed on them (Equation 3.4). A particle at time $t = 0$ (when the shear is imposed) is colored blue if $|y| \geq L/4$, else colored green. A given mode $m_n = 4$ is excited for four values of $\Gamma = 1, 5, 25, 75$ and instantaneous snapshots at three different times are taken for each Γ . One can easily notice that for higher values of Γ , the KH rolls at any given time are clearer and more pronounced. It is interesting to note that for $1 < \Gamma < 10$ ($U_0/v_{th} \sim 0.7 - 2.3$) the collective effects are seen even at the particle level. The evolution of nonlinear coherent structures ultimately results into formation of giant vortices. Such a mechanism where energy is transferred from small scales to large scale is known as inverse cascade, a process which is typical of 2D turbulence.

In Figure 3.7 we show the inverse cascading of the mode $m_n = 6$ in a Yukawa liquid at $\Gamma = 50$. At $t = 140$, the mode $m_n = 6$ (six rolls) appears which collapses at $t = 300$ before re-emerging as $m_n = 3$ at $t = 460$. The snapshot at $t = 300$ shows the transition of m_n from $6 \rightarrow 3$. By $t = 620$, one can see that the well defined mode structures are lost and the transition to turbulence is qualitatively seen. Using typical experimental parameters (Nosenko and Goree, 2004) $m \approx 4 \times 10^{-13}$ kg, $Q \approx 12000e$ where e is electronic charge and $a = 0.4$ mm we get $\Omega_{pd} \approx 50s^{-1}$. A typical growth rate in our study $\gamma = 0.02\Omega_{pd}$ corresponds to approximately $1s^{-1}$ in physical units and hence should be observable in laboratory experiments. In the following section we report the effect of neutral gas friction on the KH instability of complex plasmas.

3.4 Role of gas friction

Laboratory dusty plasma exist under finite neutral gas friction. The condensation of liquid “dusty” plasmas into a solid like state is routinely achieved by increasing the neutral gas pressure in ground based laboratory experiments. In Figure 3.8, we show the vorticity snapshot at time $t = 400$, starting from an initial value of $\Gamma_0 = 120$. The magnitude of local vorticity ($\boldsymbol{\omega} = \nabla \times \boldsymbol{v}$)

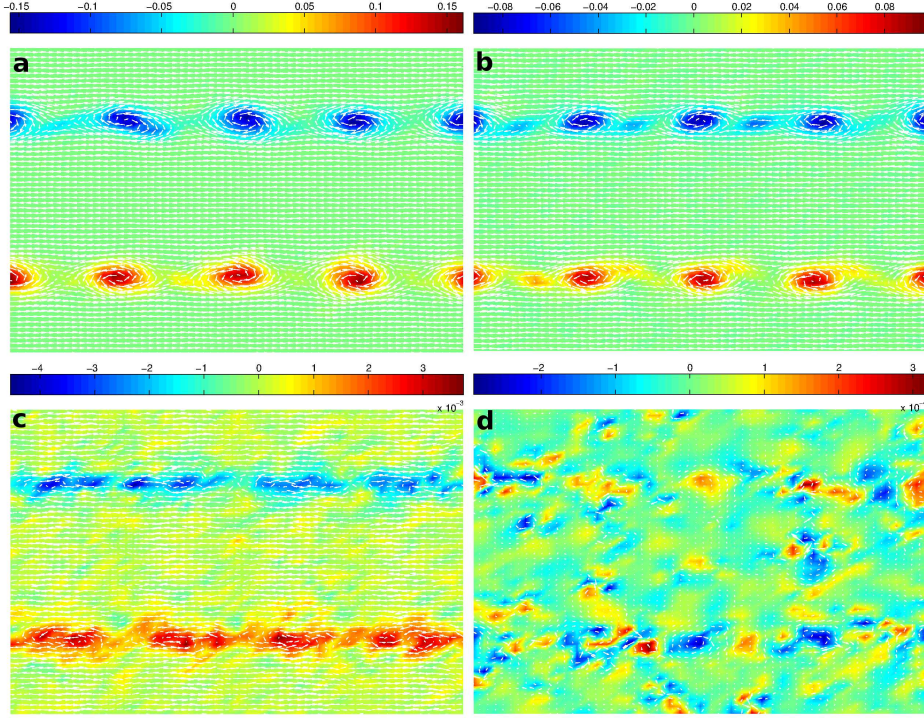


Figure 3.8: Vorticity snapshot at time $t = 400$ starting from an initial $\Gamma_0 = 120$ for different values of neutral gas drag: (a.) $\nu_{dn} = 0.001$, (b.) $\nu_{dn} = 0.005$, (c.) $\nu_{dn} = 0.025$, (d.) $\nu_{dn} = 0.125$. It is easily seen that at higher gas friction, the instability is rapidly quenched and the mode structures are lost.

is indicated on a vertical color-map label. To construct ω , the local velocity \mathbf{v} in the region is obtained by “fluidizing” the grain velocities over a 45×45 grid which amounts to averaging particle velocities locally to obtain fluid velocity at a grid point. The superposed “white” arrows indicating the local flow direction are obtained similarly from a 60×60 grid. One can easily see that gas friction has a quenching effect on the instability and hence there is no roll formation at $\nu_{dn} = 0.125$. This is confirmed from Figure 3.9, where we plot the growth rates extracted from MD as a function of gas friction. At higher values of gas friction the growth rates are negative and the instability is stabilized. A typical $\nu_{dn} = 0.025$ where KH instability is observed corresponds to 1.25 s^{-1} in physical units and hence the phenomena may be observed in laboratory experiments on dusty plasma. It will be interesting

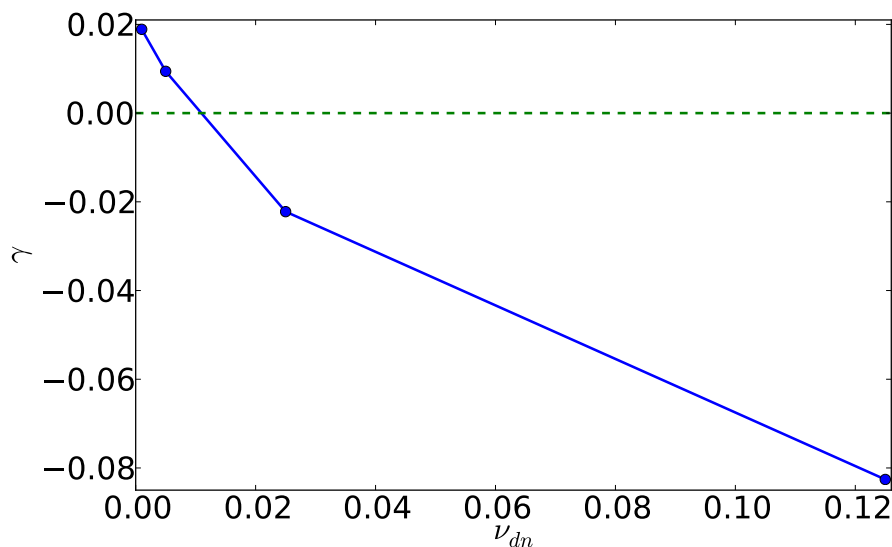


Figure 3.9: Effect of gas friction on MD growth rates. It is easily seen that the growth rates decrease with increasing values of gas friction.

to see if a lower dimensional fluid model can capture some of the underlying physics of this KH instability atleast in the linear regime. In the following section, we present a comparison of the frictionless ($\nu_{dn} = 0$) MD results obtained so far with a generalized hydrodynamics (GH) fluid model.

3.5 Generalized hydrodynamics

Conventional kinetic theories used to describe Yukawa liquids suffer from Bogoliubov-Born-Green-Kirkwood-Yvon (BBGKY) hierarchy issues (Montgomery D.C. and Tidman D.A, 1964; Ichimaru S., 1973) in the limit of strong coupling. This hierarchy is a set of equations describing the dynamics of a system of a large number of interacting particles. The equation for an s -particle distribution function in the BBGKY hierarchy includes the ($s +$

1)-particle distribution function thus forming a coupled chain of equations:

$$\begin{aligned} & \left[\frac{\partial}{\partial t} + \sum_i^s \mathcal{L}(i) - \sum_{i \neq j}^s \mathcal{V}(i, j) \right] F_s(1, \dots, s-1, s) \\ & = \sum_i^s \int d\mathbf{X}_{s+1} \mathcal{V}(i, s+1) F_{s+1}(1, \dots, s, s+1) \end{aligned} \quad (3.8)$$

Here, the single particle operator $\mathcal{L}(i)$ acting upon the i th particle under the influence of externally applied fields is given as

$$\mathcal{L}(i) = \mathbf{v}_i \cdot \frac{\partial}{\partial \mathbf{r}_i} + \frac{Q}{m} \left[\mathbf{E}_{ext}(\mathbf{r}_i, t) + \mathbf{v}_i \times \mathbf{B}_{ext}(\mathbf{r}_i, t) \right] \cdot \frac{\partial}{\partial \mathbf{v}_i} \quad (3.9)$$

and the two particle operator arising from the Yukawa interaction is given as

$$\mathcal{V}(i, j) = \frac{Q^2}{m} \left[\frac{\partial}{\partial \mathbf{r}_i} \frac{\exp(-\kappa|\mathbf{r}_i - \mathbf{r}_j|)}{|\mathbf{r}_i - \mathbf{r}_j|} \right] \cdot \frac{\partial}{\partial \mathbf{v}_i} \quad (3.10)$$

The BBGKY hierarchy (Equation 3.8) has a structure that it does not close in itself. The equation for a single-particle distribution depends on the two particle distribution, the equation for two-particle in turn requires knowledge of three-particle distribution, and so on. To proceed further, we must find a method of truncating this infinite series of equations. Such a truncation may be achieved if one approaches the fluid limit (Rostoker and Rosenbluth, 1960). Mathematically speaking, this implies, that the discreteness parameter $\Delta = 1/N_D = (3\Gamma)^{3/2} \ll 1$, where, N_D is the number of particles within the Debye sphere. Thus, in this fluid limit, the BBGKY hierarchy may be truncated through a power series expansion with respect to the the discreteness parameter Δ . Such a truncation of hierarchy becomes very hard as the coupling parameter $\Gamma = [Q^2/(4\pi\epsilon_0 a k_B T)]$ increases beyond 1. Thus, in the limit of strong coupling (low temperature or high density), Yukawa liquids are generally not amenable by kinetic theories (Ichimaru et al., 1987). As an alternative, a memory dependent generalized hydrodynamic (GH) model (Berkovsky, 1992; Ichimaru et al., 1987) has been proposed which attempts

to describe strongly coupled Yukawa liquids. This phenomenological model provides a simple picture of the effects of strong correlations through the introduction of memory dependent viscoelastic coefficients. The GH model is generally believed to be valid over a large range of the coupling parameter Γ , all the way from the weakly coupled fluid phase ($\Gamma \ll 1$) to the strongly coupled liquid regime ($1 < \Gamma < \Gamma_c$), where Γ_c is the critical value at which crystallization occurs in the dusty plasma. The model breaks down in the crystalline state where formation of lattice structure can lead to both long range and short range order in the system. Typically, these memory dependent viscoelastic coefficients are functions of the coupling parameter Γ . When Γ is small enough, i.e. in the weakly coupled regime, these coefficients simply lead to viscous damping of collective modes. As Γ increases, these coefficients provide a restoring force leading to elasticity effects. As is well known, in the limit $\Gamma \rightarrow 0$, the GH model reduces to standard Navier-Stokes (NS) hydrodynamics. Using this GH model, the existence of shear waves in strongly coupled plasmas has been theoretically predicted ([Berkovsky, 1992](#); [Kaw and Sen, 1998](#)) and observed in both numerical simulations ([Ohta and Hamaguchi, 2000b](#)) and lab experiments ([Pramanik et al., 2002](#)). The phenomenological GH model also has several limitations, such as the absence of a critical wave vector for transverse mode dispersion below which the modes are damped, failure to capture the dynamical phenomena in the long wave-number (kinetic) limit and uncertainties in the determination of viscosity $\eta(\Gamma)$ and viscoelastic relaxation time $\tau_m(\Gamma)$ ([Murillo, 2000](#)).

Here we report a linear stability analysis of parallel shear flows in strongly coupled Yukawa fluids using the GH model and compare our results with the MD simulations discussed so far. It will be shown later that the growth rate spectrum computed from GH model shows similar qualitative behavior such as viscous damping at higher modes and destabilization at strong coupling as observed in MD simulations. It is seen that close to regions of flow reversal, heat is generated which alters the local Γ . It will be shown that including this shear heating effect (see section [3.10](#) and chapter [6](#)) as an effective coupling parameter Γ_e improves the quantitative comparison as well.

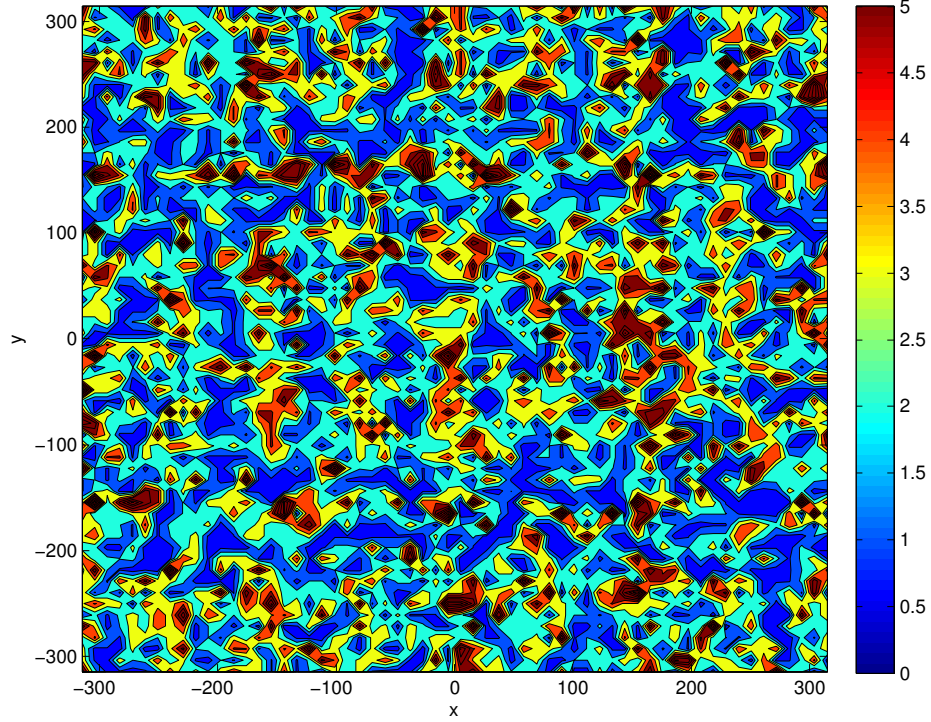


Figure 3.10: Contour plot of density fluctuation $\left| \frac{n(x,y,t) - n_0}{n_0} \right| \times 100$ at time $t = 40$ (within the linear time scale) taken from MD simulations. The initial state of the liquid is $\Gamma = 25$ at a mean density $n_0 = 0.61$. The peak value of density fluctuation (as seen from the color scale) is $\approx 5\%$. Thus at the linear time scales the system remains “incompressible” to a good approximation.

3.6 Basic assumptions

Recall that the basic equilibrium flow taken was a step shear velocity profile (Equation 3.4). As the magnitude of normalized shear velocity U_0 was smaller than the sound speed of the system, thus the shear flows studied in MD simulations can be thought of as “incompressible” in nature. In Figure 3.10, we show a snapshot of density fluctuation contour taken from MD simulations starting from an initial state of $\Gamma = 25$. The snapshot is taken at $t = 40$, which is within the linear time scale. One can easily notice that the percentage fluctuations in the density $\left| \frac{n(x,y,t) - n_0}{n_0} \right| \times 100 \leq 5\%$, which we

assume to be small enough for the system to remain incompressible. It should be noted in the MD simulations presented in (Ashwin and Ganesh, 2010a) did not include dust-neutral collisions. Following inputs from these MD simulations, we proceed to carry out the linear stability analysis of the GH model equations under the following assumptions: (a.) The dust fluid remains incompressible. (b.) The dust-neutral collisions are absent. With these assumptions we now proceed on to the next section to present the linear stability analysis of the GH model equations.

3.7 Model equations

We use the standard fluid description of dusty plasmas for studying the low frequency phenomena, where only the dust dynamics is important ($\omega \ll kv_{Te}, kv_{Ti}$) where ω is the wave frequency, k is the wave-number and v_{Te}, v_{Ti} are the electron and ion thermal speeds respectively. We will take electrons and ions as a light fluid which can be modeled by a Boltzmann distribution and take the full set of hydrodynamic equations to describe the dynamics of dust fluid. We will also assume that electrons and ions are in the weak coupling regime and only the dust fluid is in the strongly coupled regime. Thus, we write, using the GH model (Berkovsky, 1992; Kaw and Sen, 1998), the linear momentum equation for the incompressible dust fluid in the absence of dust-neutral collisions

$$\begin{aligned} (1+\tau_m\partial_t) \left[(\partial_t + \mathbf{v}\cdot\nabla)\mathbf{v} + \frac{Ze}{M}\nabla\phi + \frac{1}{\rho}\nabla P \right] \\ = \nu\nabla^2\mathbf{v} + \frac{1}{\rho}\left(\zeta + \frac{\eta}{3}\right)\nabla(\nabla\cdot\mathbf{v}) \end{aligned} \quad (3.11)$$

the equation of state, in terms of compressibility μ_d

$$\mu_d = \frac{1}{T_d} \left(\frac{\partial P}{\partial n} \right)_T = 1 + \frac{u(\Gamma)}{3} + \frac{\Gamma}{9} \frac{\partial u(\Gamma)}{\partial \Gamma} \quad (3.12)$$

with the excess internal energy of system given as (Rosenberg and Kalman, 1997; Hamaguchi et al., 1996)

$$u(\Gamma) = a(\kappa)\Gamma + b(\kappa)\Gamma^{1/3} + c(\kappa) + d(\kappa)\Gamma^{-1/3} \quad (3.13)$$

where the values of the coefficients are

$$\begin{aligned} a(\kappa) &= -0.89 + 0.5\kappa - 0.103\kappa^2 + 0.003\kappa^4, \\ b(\kappa) &= +0.565 - 0.026\kappa^2 - 0.003\kappa^4, \\ c(\kappa) &= -0.207 - 0.086\kappa^2 + 0.018\kappa^4, \\ d(\kappa) &= -0.031 + 0.042\kappa^2 - 0.008\kappa^4 \end{aligned} \quad (3.14)$$

and the equation of continuity (for an incompressible dust fluid)

$$\nabla \cdot \mathbf{v} = 0 \quad (3.15)$$

where ρ , v and Ze are the dust mass density, dust fluid velocity and dust charge, P is the dust pressure and η and ζ are the coefficients of shear and bulk viscosity respectively. Kinematic viscosity $\nu = \eta/\rho$ and ϕ is the electrostatic potential. The viscoelastic relaxation time τ_m is a measure of how memory effects due to strong coupling will influence the growth of shear instability in the medium. T_d is the dust temperature. The above momentum equation in the xy -plane can be perturbed by assuming the velocities in the \hat{x} and \hat{y} directions to be

$$U_0(y) + u(x, y, t), \quad v(x, y, t) \quad (3.16)$$

respectively, and the pressure and electric field perturbations to be

$$P + p(x, y, t), \quad \nabla\phi \quad (3.17)$$

where the lower-case symbols indicate perturbed quantities. The introduction of (3.16) and (3.17) into the GH equation (4.4) and linearization leads

to the following two partial differential equations

$$\begin{aligned} (1+\tau_m\partial_t) \left[\partial_t u + U_0\partial_x u + v\frac{dU_0}{dy} + \frac{1}{\rho}\partial_x p + \frac{Ze}{M}\partial_x\phi \right] \\ = \nu\nabla^2 u + \frac{1}{\rho}\left(\zeta + \frac{\eta}{3}\right)\partial_x(\partial_x u + \partial_y v) \end{aligned} \quad (3.18)$$

$$\begin{aligned} (1+\tau_m\partial_t) \left[\partial_t v + U_0\partial_x v + \frac{1}{\rho}\partial_y p + \frac{Ze}{M}\partial_y\phi \right] \\ = \nu\nabla^2 v + \frac{1}{\rho}\left(\zeta + \frac{\eta}{3}\right)\partial_y(\partial_x u + \partial_y v) \end{aligned} \quad (3.19)$$

Linearization of the continuity equation (3.15) leads to

$$\partial_x u + \partial_y v = 0 \quad (3.20)$$

Differentiating (3.18) with respect to y , and (3.19) with respect to x and subtracting the resulting equations yields the following vorticity equation

$$(1 + \tau_m\partial_t) \left[(\partial_t + U_0\partial_x)(\partial_y u - \partial_x v) + v\frac{d^2U_0}{dy^2} \right] = \nu\nabla^2(\partial_y u - \partial_x v) \quad (3.21)$$

From (3.20), we define the stream function ψ as,

$$u = \partial_y\psi, \quad v = -\partial_x\psi \quad (3.22)$$

Putting (3.22) in (3.21), we get the vorticity equation in the stream function formulation within the GH model.

$$(1 + \tau_m\partial_t) \left[(\partial_t + U_0\partial_x)\nabla^2\psi - \partial_x\psi\frac{d^2U_0}{dy^2} \right] = \nu\nabla^4\psi \quad (3.23)$$

Taking normal mode ansatz :

$$\psi(x, y, t) = \xi(y)e^{ik(x-ct)} \quad (3.24)$$

and using it in Equation 3.23, we obtain

$$\left(\frac{d^2}{dy^2} - k^2\right)^2 \xi(y) = \frac{ik}{\nu}(1 - i\tau_m kc) \left[(U_0 - c) \left(\frac{d^2}{dy^2} - k^2\right) \xi(y) - \frac{d^2 U_0}{dy^2} \xi(y) \right] \quad (3.25)$$

Equation 3.25 is the GH Orr-Sommerfeld equation. If the basic flow is characterized by some equilibrium shear length scale l and velocity scale U_0 , then the Reynolds number may be defined as

$$R = U_0 l / \nu \quad (3.26)$$

and Equation 3.25 can be written in the dimensionless form as

$$\left(\frac{d^2}{dy^2} - k^2\right)^2 \xi(y) = ikR(1 - i\tau_m kc) \left[(U_0 - c) \times \left(\frac{d^2}{dy^2} - k^2\right) \xi(y) - \frac{d^2 U_0}{dy^2} \xi(y) \right] \quad (3.27)$$

The GH Orr-Sommerfeld equation (3.27) has exponential solutions given by

$$\xi(y) = e^{\pm ky}, e^{\pm \beta y} \quad (3.28)$$

where

$$\beta = \left[k^2 - ikR(1 - i\tau_m kc)(c - U_0) \right]^{1/2} \quad (3.29)$$

For a basic step shear profile with the interface at $y = 0$, we have

$$U_0 = y/|y| \quad (-\infty < y < \infty) \quad (3.30)$$

and using the following boundary conditions for $\xi(y)$ and its derivatives following (Drazin, 1961),

$$\begin{aligned} [\xi] &= 0 \\ \left[\frac{d\xi}{dy} \right] &= 0 \\ \left[\left(\frac{d^2}{dy^2} + \beta^2 \right) \xi \right] &= 0 \\ \left[\left(\frac{d^2}{dy^2} - \beta^2 \right) \frac{d\xi}{dy} \right] &= 0 \end{aligned} \quad (3.31)$$

where the brackets are used to denote the jump or difference across the discontinuity, of their contents. The most general solution of the GH Orr-Sommerfeld equation satisfying the boundary conditions at infinity has the following form

$$\xi = \begin{cases} Ae^{-ky} + Be^{-\beta_1 y} & (y > 0), \\ Ce^{ky} + De^{\beta_2 y} & (y < 0) \end{cases} \quad (3.32)$$

where A, B, C, D are some constants and

$$\begin{aligned} \beta_1 &= \left[k^2 - ikR(1 - i\tau_m kc)(c - 1) \right]^{1/2} \\ \beta_2 &= \left[k^2 - ikR(1 - i\tau_m kc)(c + 1) \right]^{1/2} \end{aligned} \quad (3.33)$$

Using the boundary conditions (Equation 3.31) at $y = 0$, we get four homogeneous linear equations in A, B, C, D . A non-zero solution exists if and only if their discriminant is zero; thus the eigen value relation is

$$0 = \begin{vmatrix} 1 & 1 & 1 & 1 \\ -k & -\beta_1 & k & \beta_2 \\ \beta_1^2 + k^2 & 2\beta_1^2 & \beta_2^2 + k^2 & 2\beta_2^2 \\ k(\beta_1^2 - k^2) & 0 & -k(\beta_2^2 - k^2) & 0 \end{vmatrix} \quad (3.34)$$

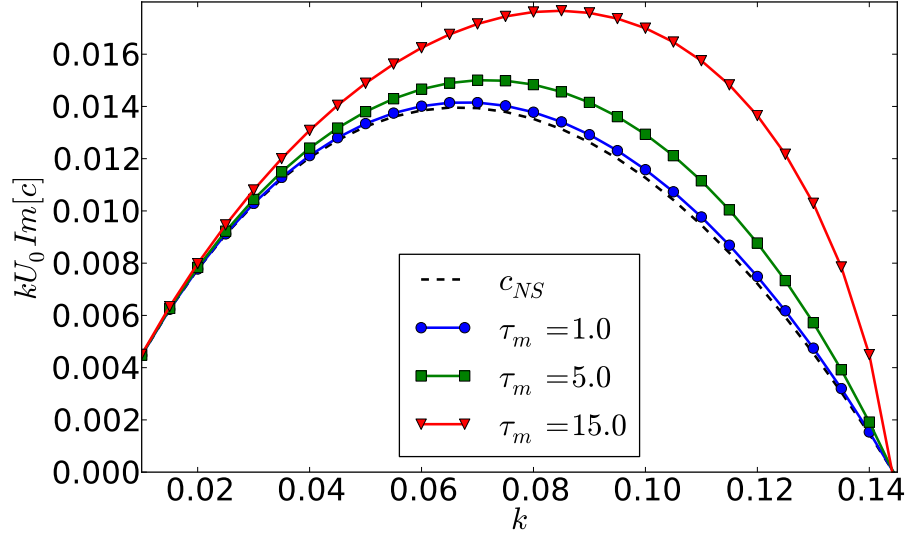


Figure 3.11: Growth rate spectra of GH model obtained from Equation 3.36 are numerically plotted (solid lines) for $\tau_m = 1, 5$ and 15 at $R = 1$. For comparison, NS growth rates from Equation 3.39 are also plotted (line-symbols) at the same value of $R = 1$. It is clearly seen that the GH growth rate spectra obtained from solutions of Equation 3.36 converges to NS growth rates in the limit $\tau_m \rightarrow 0$.

Following (Drazin, 1961), we evaluate the above determinant and obtain the following dispersion relation

$$\frac{R(1 - i\tau_m kc)}{k} = \frac{-4i(c - \sqrt{3}i)}{3c^2 - 1 - 2\sqrt{3}ci} \quad (3.35)$$

Equation 3.35 is similar to Drazin's result except for the viscoelastic correction term $(1 - i\tau_m kc)$. We write down Equation 3.35 as a polynomial equation in c as follows:

$$p_0 c^3 + p_1 c^2 + p_2 c + p_3 = 0 \quad (3.36)$$

with the coefficients of the polynomial given as

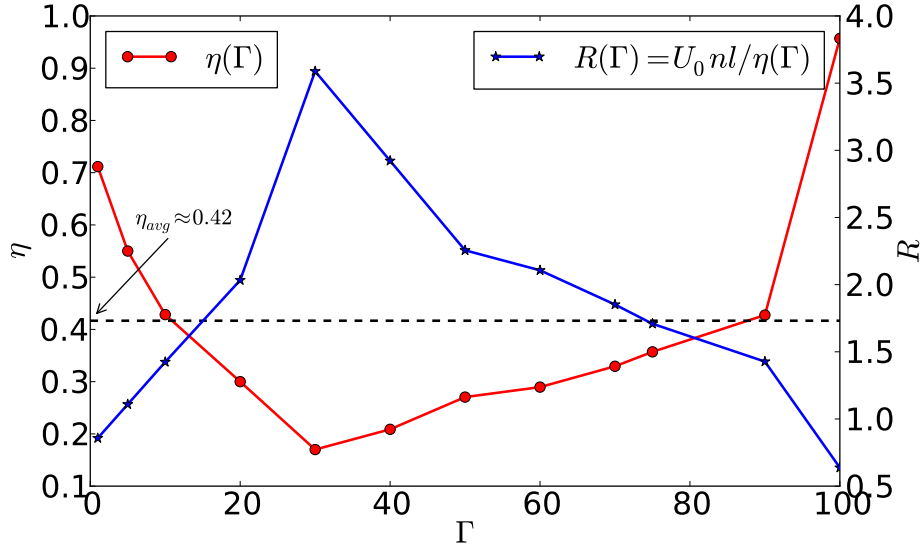


Figure 3.12: Plot of normalized shear viscosity and Reynolds number $R = U_0nl/\eta$ vs coupling parameter Γ taken from MD simulations (Ashwin and Ganesh, 2010a). Physical parameters are : $l = 1, U_0 = 1$ and $n = 0.61$. It is clearly seen that η and hence R have a non-monotonic nature in the interval $1 < \Gamma < 100$. The average value of viscosity in the entire range of Γ is $\eta_{avg} \approx 0.42$.

$$\begin{aligned}
p_0 &= 3Ri\tau_mk \\
p_1 &= (2\sqrt{3}\tau_mk - 3)R \\
p_2 &= (2\sqrt{3}R - 4k - R\tau_mk)i \\
p_3 &= R - 4k\sqrt{3}
\end{aligned} \tag{3.37}$$

The appropriate root from of Equation 3.36 is one which converges to the NS growth rate in the limit $\tau_m \rightarrow 0$, i.e

$$\lim_{\tau_m \rightarrow 0} c = c_{NS} \tag{3.38}$$

where the NS growth rate is given by (Drazin, 1961)

$$c_{NS} = \frac{i}{3} \left\{ \sqrt{3} - 2\frac{k}{R} - 2 \left[\left(\frac{k}{R} \right)^2 + 2\sqrt{3} \left(\frac{k}{R} \right) \right]^{1/2} \right\} \tag{3.39}$$

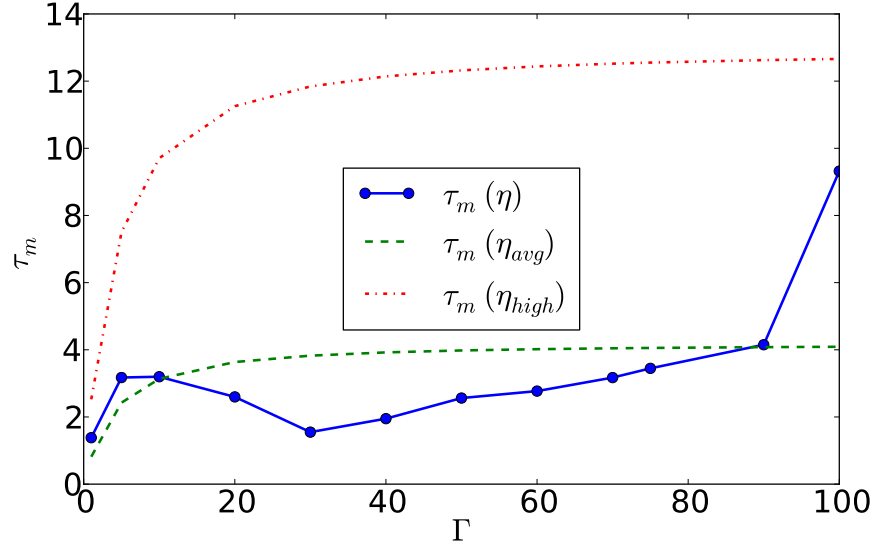


Figure 3.13: Viscoelastic relaxation time τ_m plotted as a function of Γ using Equation 3.40. We take the one component plasma (OCP) approximation for bulk viscosity: $\zeta = 0$. The rise in τ_m is clearly evident towards higher values of Γ . As is well known, for $\Gamma \rightarrow 0$, it follows that $\tau_m \rightarrow 0$ (no memory effects) and the GH model reduces to the standard Navier-Stokes hydrodynamics. Dashed lines show τ_m obtained by taking an average value: $\eta_{avg} = 0.42$ and a higher value $\eta_{high} = 1.3$ as shown in (Ashwin and Ganesh, 2010b).

The condition (Equation 3.38) is satisfied by only one of the roots of Equation 3.36 which is shown in Figure 3.11, where we plot the GH growth rate spectra for various values of τ_m . The NS growth rate spectra obtained from Equation 3.39 is also plotted with line-symbols. It is clearly seen that in the limit $\tau_m \rightarrow 0$, GH spectra converges to the standard NS spectrum. We now proceed to the next section to present the effect of coupling parameter Γ on shear viscosity η and viscoelastic relaxation time τ_m .

3.8 Effect of coupling parameter on shear viscosity and relaxation time

As it is evident now from the preceding section, the growth rates calculated analytically from GH model (Equation 3.36) and NS hydrodynamics

(Equation 3.39) depend crucially on Reynolds number R . Hence it becomes imperative to estimate R for the Yukawa liquid under consideration before any comparison can be made. In Figure 3.12, we plot the values of shear viscosity as a function of coupling parameter Γ from previous MD simulations (Ashwin and Ganesh, 2010a). Equation 3.36 contains strong coupling corrections to Equation 3.39 which are manifested in the viscoelastic relaxation time τ_m . Typically τ_m depends on coupling parameter Γ and is given as (Berkovsky, 1992)

$$\tau_m = \frac{(4\eta/3 + \zeta)\Gamma}{(3 - \Upsilon\mu_d)n + 4u/15} \quad (3.40)$$

where Υ is the adiabatic index, which for a 2D system is taken as 2, n is the number density ≈ 0.61 in MD simulations (Ashwin and Ganesh, 2010a) and μ_d is the compressibility given by Equation 3.12. Using Equation 3.12, 3.13, 3.14 and 3.40, the viscoelastic relaxation time τ_m is computed for values of Γ in the range $1 < \Gamma < 100$ and plotted in Figure 3.13. It should be noted that the estimation of τ_m within the GH model is prone to uncertainties (Murillo, 2000) due to the presence of various thermodynamic parameters (Equation 3.40). We now move on to the next section to discuss the effect of Γ on GH growth rates.

3.9 Effect of coupling parameter on GH growth rates

To obtain growth rate spectra of KH instability at a given Γ under the GH model one needs to first extract the corresponding value of τ_m from Figure 3.13 (line-symbols). Using this value of τ_m , the growth rate spectra under the GH model can then be obtained from Equation 3.36. In Figure 3.14, we plot the GH growth rates by individually picking the values of R from Figure 3.12. Here we find that the growth rates do not match everywhere for a given value of R , and find that the comparison between GH model and MD simulations is at best only qualitative. In the next section, we discuss

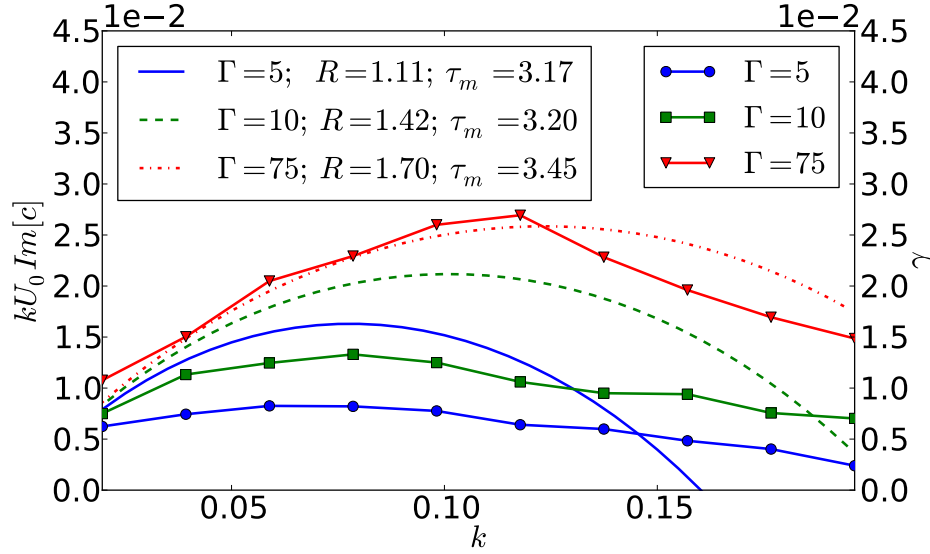


Figure 3.14: Comparison of growth rate spectra calculated from GH model [Equation 3.36 and solid lines] and MD simulations (Ashwin and Ganesh, 2010a) (line-symbols). The value of R and τ_m at each Γ are picked up from Figures 3.12 and 3.13 respectively. It is clearly seen that MD growth rates do not match with the GH growth rates for all values of Γ and that there is only qualitative agreement at best.

the shear heating effects on the GH growth rates.

3.10 Effect of shear induced heating on growth rates

Shear flows also lead to “particle heat generation” (Rapaport, D. C., 1995). Such shear induced heat generation has been known to cause solid to liquid phase transition in soft materials (Ackerson and Clark, 1981; Delhomme, 2004) and complex plasmas (Nosenko and Goree, 2004). Shear induced heating in viscous flows has been studied analytically (Landau and Lifschitz, 2007) and observed in laboratory experiments on dusty plasmas (Nosenko et al., 2008). We observe similar heating effect in MD simulations of strongly coupled Yukawa liquids (Ashwin and Ganesh, 2010a) (shown in Figure 3.15), where close to regions of flow reversal, heat is generated and local Γ is al-

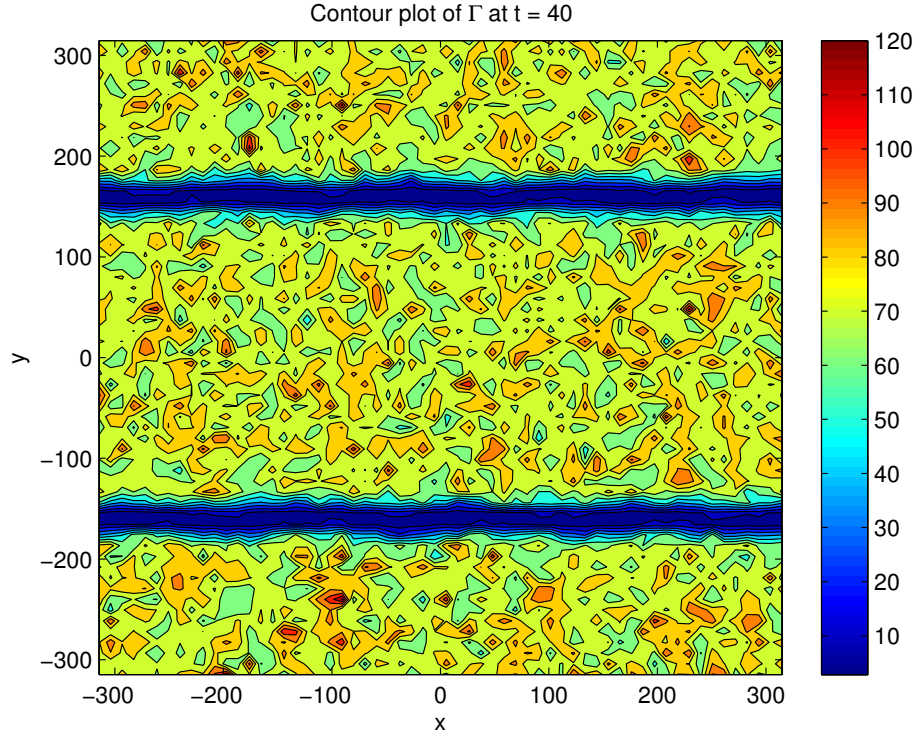


Figure 3.15: Snapshot showing contour plot of Γ at $t = 40$ taken from MD simulations (Ashwin and Ganesh, 2010a) starting from an initial uniform background coupling parameter $\Gamma = 75$. The sheared flow leads to heat generation close to the regions of flow reversal at $y = \pm L/4$, where $L = 640$. As a result two strips parallel to \hat{x} are formed at lower effective coupling parameter Γ_e .

tered. To illustrate this, in Figure 3.15, a snapshot of temperature contour at time $t = 40$ is presented starting from an initial thermal equilibrium of $\Gamma = 75$. Shear induced Γ profile develops at much faster time scales than the linear growth time scales as shown in Figure 3.16, where we have plotted Γ as a function of y ($x = 0$) at different times within the linear regime. Hence we can think of a quasi-static local thermal equilibrium within the shear layer in the form of an effective coupling parameter Γ_e . Using this value of Γ_e within the shear layer one can then compute the value of local relaxation time τ_m and local Reynolds number R . In Figure 3.17, we plot the MD growth rate spectra at various values of Γ_e and the corresponding GH growth

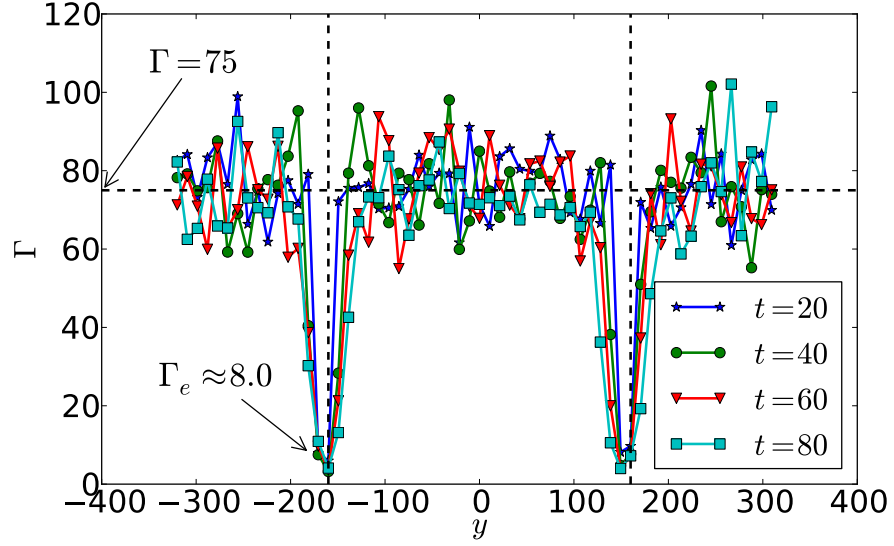


Figure 3.16: Profiles of coupling parameter Γ as a function of y at $x = 0$ taken from MD simulations. The initial state is a uniform $\Gamma = 75$. These profiles are plotted at various times during the linear regime. Vertical dashed lines represent the location of shear layers. We clearly see that the shear induced Γ profile develops at $t \leq 20$, which is much smaller than the linear growth time scales ($t \sim 100$) and appears to remain almost stationary. Hence we can think of quasi-static thermal equilibrium within the shear layer in the form of an effective coupling parameter Γ_e . For the initial state of $\Gamma = 75$ (shown by the horizontal dashed line), the effective $\Gamma_e \approx 8.0$.

rates computed from local values of R and (a.) τ_m using values of Γ_e , (b.) $\tau_m(\eta_{avg})$ and (c.) $\tau_m(\eta_{high})$. Inclusion of shear induced heating in the form of Γ_e appears to improve comparison between GH and MD growth rates. It should be noted that the quasi-static temperature gradient formed due to shear heating effects does not alter the stability analysis of the GH model carried out in Section(3.7). At lower values of effective coupling parameter i.e $\Gamma_e < 8.0$, the agreement is again only qualitative.

3.11 Summary

Using “first principles” MD simulations, we observed Kelvin Helmholtz instability in strongly coupled Yukawa liquids at the particle level for the first

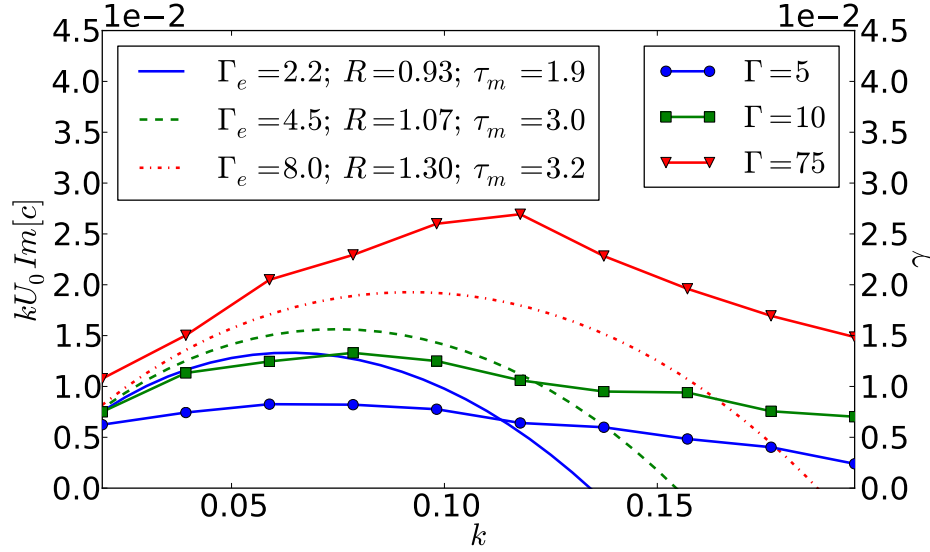


Figure 3.17: (a.) Comparison of growth rate spectra directly obtained from MD simulations (Ashwin and Ganesh, 2010a) (line-symbols) and GH model [Equation 3.36]. The GH growth rates are calculated using the values of local τ_m and R . It is clearly seen that the MD and GH growth rates agree both qualitatively and quantitatively at $\Gamma_e = 8.0$. At lower value of coupling parameter, the growth rates again do not match because the random motion of particles dominate over streaming motion and hence the KH instability is stabilized. This molecular effect is not captured by the GH model and growth rate spectra for GH and MD do not agree at low Γ_e .

time. A double step velocity shear profile is used to study this instability. The linear growth rates (γ) are directly computed from MD simulations and vortex roll formation in the non-linear regime is reported. The most interesting feature we notice here is the increase of instability growth rate with strong coupling. We also observe inverse cascading of the modes in time. For a comparison, we performed a linear stability analysis of the GH model equations using the assumption of incompressibility. We find that the growth rates calculated from GH model match only qualitatively with the MD results. Inclusion of the effect of shear heating as an effective coupling parameter Γ_e appears to improve the quantitative comparison. However, we find a general disagreement between GH and MD growth rates at high mode numbers for all values of Γ_e . This could be due to the limitations of the

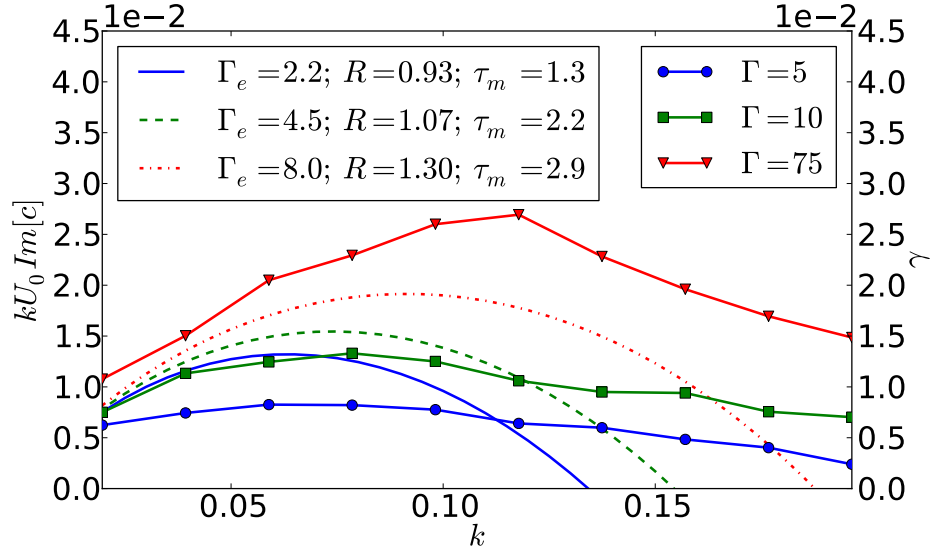


Figure 3.17: (b.) The values of τ_m are calculated using an average value of η , i.e. $\eta_{avg} = 0.42$ (see Figure 3.13).

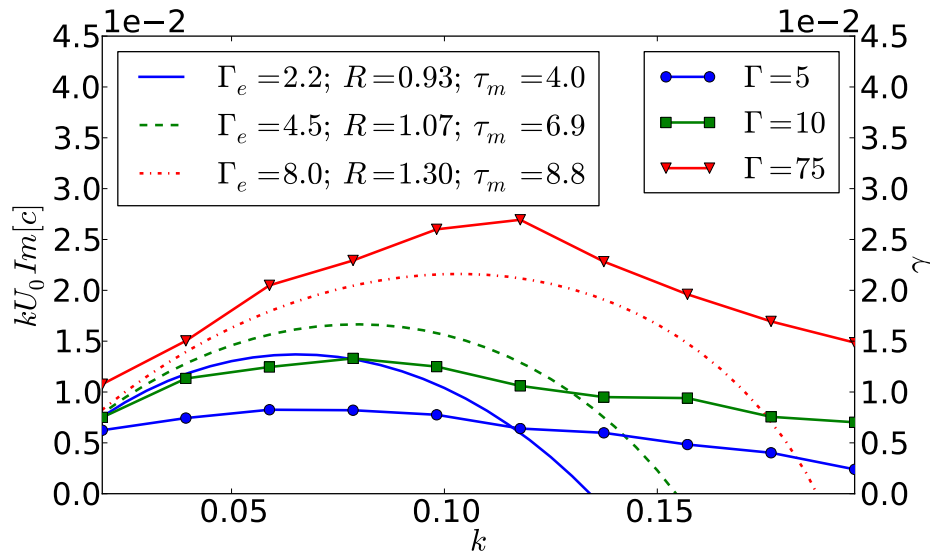


Figure 3.17: (c.) The values of τ_m are calculated using a high value of η , i.e. $\eta_{high} = 1.30$ (see Figure 3.13) (Ashwin and Ganesh, 2010b). From (a.), (b.) and (c.), one can clearly see that the agreement between MD and GH growth rates are at best only qualitative.

GH model especially the uncertainties in the determination of viscosity $\eta(\Gamma)$ and viscoelastic relaxation time τ_m . Some open questions can be addressed in the context of the present work such as shock propagation (super sonic U_0), stability analysis of nonlinear GH model ([Frenkel, 1946](#)), detailed study of transition to turbulence, instability across liquid-solid regime ($\Gamma \approx 140$) and study of flows with resonantly unstable modes ([S. Chandrasekhar, 1998](#)). The emergence of coherent vortices in the nonlinear regime of KH destabilized flows motivates one to think of the stability of an isolated coherent vortex. In the following chapter, the emergence and stability of an isolated axisymmetric vortex is studied through classical MD simulations.

Chapter 4

Centrifugal Flows

In the present chapter, using “first principles” molecular dynamics (MD) simulations, we report for the first time, the emergence of isolated coherent tripolar vortices from the evolution of axisymmetric or centrifugal flows in a prototype two-dimensional (2D) strongly coupled liquid, namely the Yukawa liquid. It is shown through MD simulations that the tripolar vortices persist over several turn over times and hence may be observed in strongly coupled liquids such as complex plasma, liquid metals and astrophysical systems like white dwarfs and giant planetary interiors, thereby making the phenomenon universal. Linear growth rates directly obtained from MD simulations are compared with a generalized hydrodynamic model.

4.1 Introduction

Emergence of coherent structures is a preeminent feature of both freely decaying and forced two-dimensional (2D) Navier-Stokes turbulence - a subject that has been of great interest to the physics community for the past three decades ([McWilliams, 1984](#); [Legras et al., 1988](#); [Kukharkin, 1995](#)). For decades, physicists have been fascinated by two main characteristics of these isolated coherent vortices, first, they are long-lived, which implies that they can last for several eddy turnover times and second, their ability to remarkably enhance transport length scales. A thorough understanding of the evo-

lution and dynamics of these coherent structures is extremely important because of their relevance to large scale planetary fluid dynamics (Pedlosky, 1987), astrophysical flows (Balbus and Hawley, 1998) and turbulent transport in fusion plasmas (Lin et al., 1998), to mention a few. In their seminal experimental work, Van Heijst and Kloosterziel showed the emergence of a coherent structure, the tripole, from an unstable cyclonic vortex in a homogeneously rotating fluid (Van Heijst and Kloosterziel, 1989). They found that the tripole was a very stable structure which could persist even in a highly sheared environment. Later (Carton et al., 1989) studied the generation of tripoles from the instability of axisymmetric monopoles through numerical simulations of barotropic equations. Since then, a great amount of work has been done to show the emergence of coherent vortices in the decay of an unstable axisymmetric vortex (Orlandi and van Heijst, 1992; Barba and Leonard, 2007). However, their emergence in such weakly coupled systems raise a few very important questions : Can coherent structures like tripoles emerge in strongly coupled liquids like complex plasmas, condensed matter systems and astrophysical systems such as white dwarfs, thereby making this phenomenon universal ? Can we study the growth and saturation of these structures in laboratory experiments ? What determines the lifetime of these vortices in such strongly coupled liquids ? In chapter 3, a study of Kelvin-Helmholtz (KH) instability in strongly coupled Yukawa liquids was reported using large scale molecular dynamics (MD) simulations (Ashwin and Ganesh, 2010a), wherein, coherent vortices were seen to evolve in the non-linear regime. An important question which immediately follows is the emergence and stability of isolated coherent vortices in strongly coupled liquids, which is the subject matter of the present work.

4.2 Molecular dynamics

We have performed large scale MD simulations to study the emergence and evolution of coherent structures in a 2D strongly coupled Yukawa liquid. As before, the Yukawa liquid can be fully characterized by two dimensionless numbers: (i) the coupling parameter Γ , and (ii) the screening parameter $\kappa =$

a/λ_D . The length, time and energy are normalized to a , Ω_{pd}^{-1} and $Q^2/(4\pi\epsilon_0a)$, respectively. The plasma frequency is given by $\Omega_{pd} = [Q^2n/(2\epsilon_0ma)]^{1/2}$, where n and m are the 2D dust number density and mass of the dust grain, respectively. We take a total of 2.304×10^5 grains for the 2D Yukawa liquid and periodic boundary conditions are employed along \hat{x} and \hat{y} . The number density n of the Yukawa liquid is taken to be 1, which gives us a square region of size $L = 480$, centered at origin $(0,0)$. The value of screening parameter κ in all our simulations is taken to be 0.5. The initial state is prepared by first connecting the 2D system to a Gaussian thermostat (Evans et al., 1983) and letting it evolve canonically for $200\Omega_{pd}^{-1}$. We then remove the thermostat and let the system evolve for another $50\Omega_{pd}^{-1}$ micro-canonically. A standard leapfrog integrator with a time-step $\Delta T = 0.01\Omega_{pd}^{-1}$ is employed such that the fluctuation in total energy is less than $10^{-4}\%$ (shown in Figure 4.1) over a typical run duration of $1000\Omega_{pd}^{-1}$. The initial equilibrium is a thermally equilibrated Yukawa liquid at a desired Γ along with the following azimuthal velocity profile superposed on grain velocities (only once at time $t = 0$). Thus, we have, in polar coordinates (r, θ) :

$$V_r = 0, \quad V_\theta = V_0(1 + \Delta\cos(m_n\theta)) \quad (4.1)$$

where V_0 is the basic azimuthal velocity profile given by

$$V_0 = 2.25\left(\frac{r}{l}\right)\exp\left(-\left(\frac{r}{l}\right)^5\right) \quad (4.2)$$

m_n is the mode number excited, Δ is the perturbation amplitude taken as 0.1 and l is the scale length of vorticity variation which is taken to be 50. The corresponding basic vorticity profile is given as $\omega_0 = \nabla \times V_0 = -(4.5/l)[2.5(r/l)^5 - 1]\exp(-(r/l)^5)$. Clearly this basic vorticity profile exhibits two regions of oppositely signed vorticity from the center to the periphery. This profile has a zero net circulation ($\int_0^\infty \omega_0 r dr = 0$) and such vortices are also known as ‘‘shielded vortices’’. Our choice of velocity profile as seen in Equation 4.1 is physically motivated by extensive laboratory experiments (Van Heijst and Kloosterziel, 1989) and numerical simulations

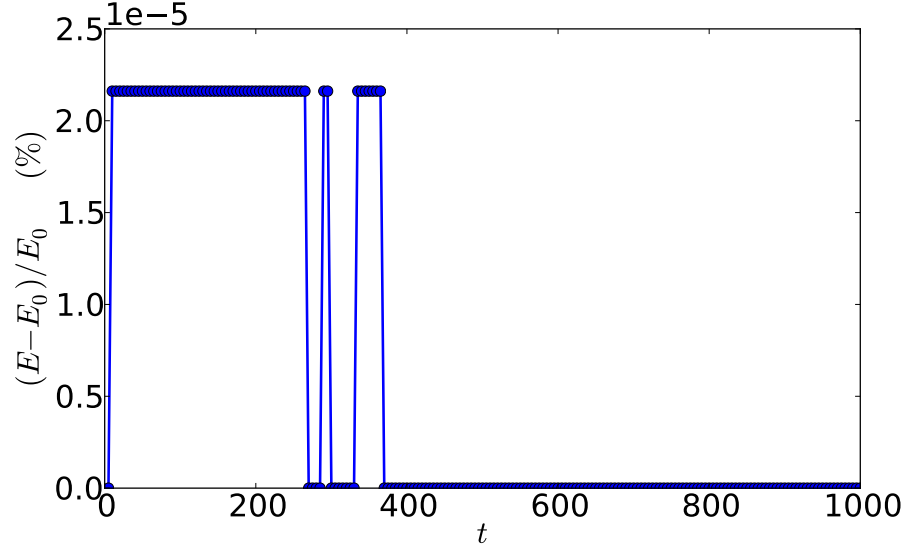


Figure 4.1: Energy conservation: Fluctuation in total energy is less than $10^{-4}\%$ over a typical run duration of $1000\Omega_{pd}^{-1}$ without the thermostat.

(Carton et al., 1989) in fluid dynamics. We define an eddy turnover time for the vortex as $T = 2\pi r_m / V_0(r=r_m)$, where r_m is the distance at which V_0 becomes maximum. Setting $(dV_0/dr)|_{r=r_m} = 0$, we get $r_m = (1/5)^{1/5}l$ and hence the turnover time $T \approx 170\Omega_{pd}^{-1}$. In the following section, we report the results obtained from our MD simulations.

4.3 Evolution of a tripole

At a time $t \approx 2.82 T$ into the simulation, with initial $\Gamma = 50$ and $m_n = 2$ excited, a tripole vortex has emerged from the centrifugal instability as seen in Figure 4.2. It will be shown later in Figure 4.5 that $m_n = 2$ is the fastest growing mode, thus leading to the formation of a tripole. The snapshot shows the vorticity profile for the partial system $(\pm 175, \pm 175)$ and one can clearly see the compact region having three aligned patches (a central core and the two accompanying satellites containing cyclonic and anti-cyclonic vorticity respectively). The total circulation within the satellites is equal and opposite to the circulation within the central core. The tripole also exhibits

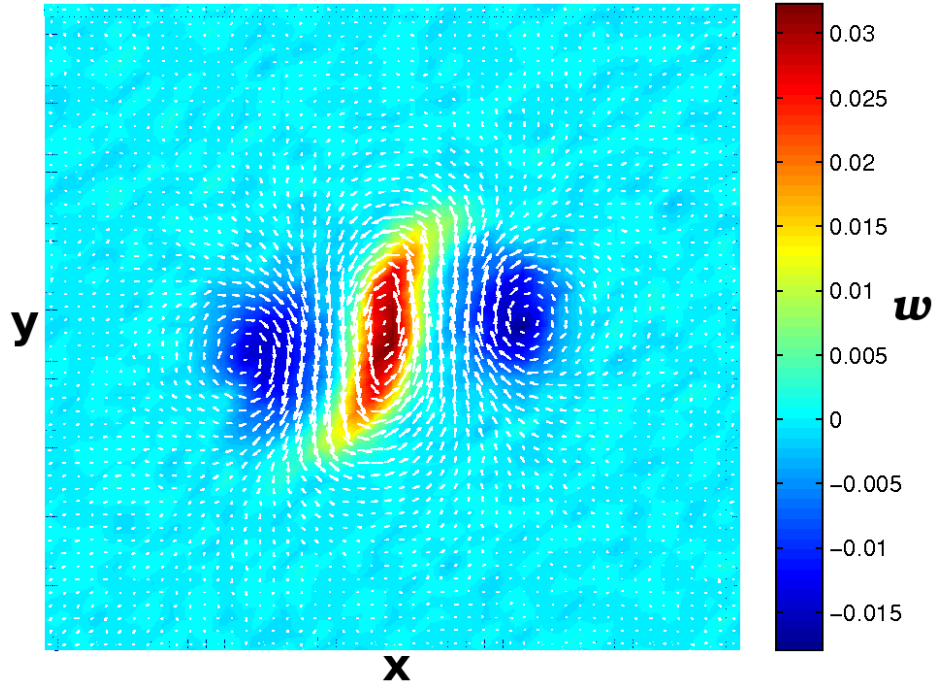


Figure 4.2: Tripole emerging at time $t = 2.82 T$, starting from an initial $\Gamma = 50$. The snapshot shows vorticity ($\omega = \nabla \times \mathbf{v}$) plot for only a partial system ($\pm 175, \pm 175$). Grain velocities in the region are fluidized through a 45×45 grid to construct local vorticity. Blue and red regions correspond to negative and positive vorticity respectively and the color-map label shows the magnitude of local vorticity. Arrows indicating direction of local velocity are obtained by fluidizing the grain velocities over a 60×60 grid.

a cyclonic rotation around the central core and is seen to be a very stable structure, sometimes persisting up to several turnover times. The magnitude of local vorticity ($\omega = \nabla \times \mathbf{v}$) is indicated on a vertical color-map label. The local velocity \mathbf{v} in the region is obtained by “fluidizing” the grain velocities over a 45×45 grid which amounts to averaging particle velocities locally to obtain fluid velocity at a grid point. At $\Gamma = 50$, the thermal velocity $v_{th} = \sqrt{2/\Gamma} = 0.2$ and the ratio $v_{th}/V_{0(r=r_m)} \approx 0.15$. It should be noted that the value of Γ close to the vortex boundaries decreases gradually in time due to shear induced heating (see chapters 3 and 6). The superposed arrows indicating the local flow direction are obtained similarly from a 60×60 grid.

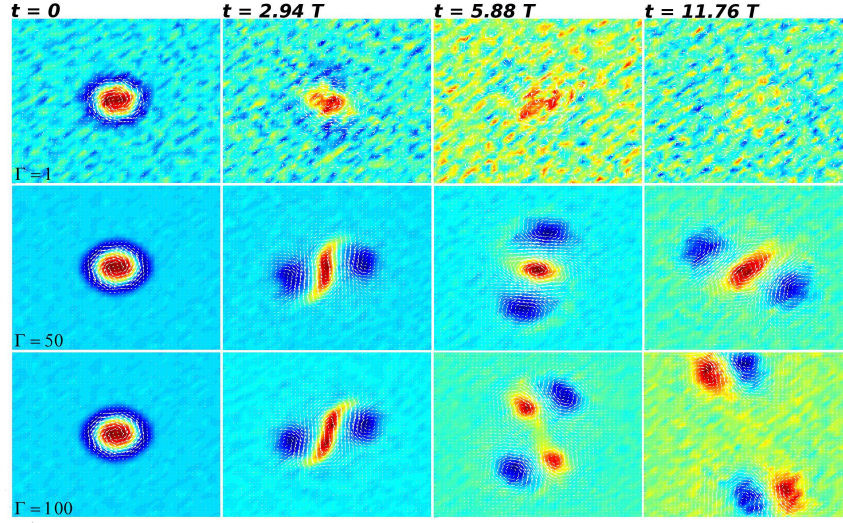


Figure 4.3: Time evolution of the vorticity profile for different values of initial Γ . The individual snapshots are shown for the full system ($\pm 240, \pm 240$) at times $t = 0, 2.94 T, 5.88 T$ and $11.76 T$ for three values of initial Γ , namely $\Gamma = 1, 50$ and 100 when a given mode ($m_n = 2$) is excited. Rows and columns show snapshots at constant Γ and t respectively. Blue and red regions correspond to negative and positive vorticity respectively. At higher Γ 's, the mode structures are more prominent and at the lowest Γ (highest temperature), the mode structures are weak and look diffused due to random thermal collisions between grains. It is interesting to note that for $\Gamma = 50$, a tripole persists (though rotating) throughout the total run duration, whereas, at $\Gamma = 100$, the tripole breaks into two propagating dipoles moving in opposite directions until $t = 11.76$ when the periodic boundaries come into play [see bottom-right].

4.4 Effect of strong coupling

We have performed 2D MD simulations for the centrifugal instability of the profile given by Equation 4.1 at three different values of initial coupling parameter Γ , namely $\Gamma = 1, 50, 100$. A given mode $m_n = 2$ is excited and coherent tripolar vortices are seen to emerge close to the end of the linear regime (Figure 4.3). It is interesting to note the following facts: At strongest coupling ($\Gamma = 100$), the tripole vortex decays into two dipoles propagating in opposite directions, whereas, at $\Gamma = 50$, the tripole vortex is very stable and persists up to the entire duration of MD simulation ($11.76 T$). Such stable

tripolar structures have been reported in early fluid simulations of barotropic equations (Carton et al., 1989; Orlandi and van Heijst, 1992). Those fluids, however, were uncorrelated and without any strong coupling effects. At the highest temperature ($\Gamma = 1$), the mode structures are weak and look diffused due to random thermal collisions between grains. At higher Γ , the collective effects are more pronounced and can be seen even at the particle level.

To understand the growth characteristic of a particular mode m_n , we study the time evolution of the perturbed kinetic energy along radial direction ($\hat{\mathbf{r}}$) normalized to its initial value:

$$|\delta E_r| = \frac{\int \int (\hat{\mathbf{r}} \cdot \mathbf{v}(t))^2 dx dy}{\int \int (\hat{\mathbf{r}} \cdot \mathbf{v}(0))^2 dx dy} \quad (4.3)$$

Starting from an initial state of $m_n = 2$ and $\Gamma = 50$, we plot this perturbed kinetic energy as a function of time and observe a linear growth eventually leading to a nonlinear saturation at late times (Figure 4.4). The dashed line shows a fit to the initial linear growth regime. The slope (2γ) of this fit gives the growth rate of the centrifugal instability (γ). One clearly sees the onset of nonlinear saturation close to $t \approx 2.82T$ as shown by the vertical dashed line.

4.5 Comparison with viscoelastic model

Although MD simulation results presented so far are an exact numerical solution to the N body problem and hence “first principles” in nature, it will be interesting to see if a lower dimensional fluid model can capture some of the underlying physics of the centrifugal instability as described in chapter 3. A well known phenomenological fluid model for complex plasmas is the generalized hydrodynamic (GH) model (Ichimaru et al., 1987; Berkovsky, 1992; Kaw and Sen, 1998) which attempts to describe strong coupling effects through the introduction of memory dependent viscoelastic coefficients. The GH model also has several limitations (Murillo, 2000) and in the case of parallel shear flows, the comparison between MD simulations and GH model is at best only qualitative (Ashwin and Ganesh, 2010b). However, in light

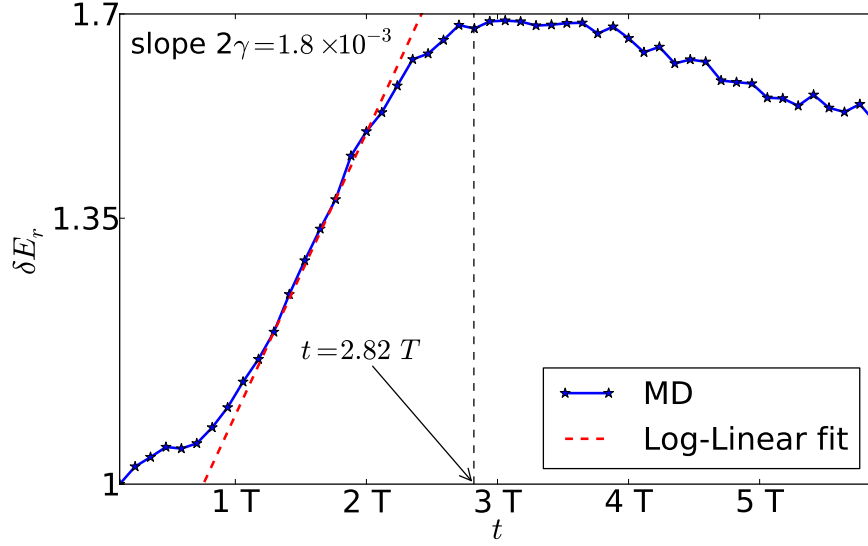


Figure 4.4: Time evolution of perturbed kinetic energy along \hat{r} on a log-linear scale for $m_n = 2$ and $\Gamma = 50$. The red dashed line shows a fit to the initial linear growth regime having slope 2γ . The vertical dashed line shows the onset of nonlinear saturation regime at $t = 2.82T$ which also coincides with the emergence of the fully developed tripole (Figure 4.2).

of the foregoing discussion, we obtain an analytical estimate of the linear growth rate of the centrifugal instability using the GH model. Thus, we write, the linear momentum equation for the incompressible dust fluid in the absence of dust-neutral collisions as

$$(1 + \tau_m \partial_t) \left[(\partial_t + \mathbf{v} \cdot \nabla) \mathbf{v} + \frac{Ze}{M} \nabla \phi + \frac{1}{\rho} \nabla P \right] = \nu \nabla^2 \mathbf{v} + \frac{1}{\rho} \left(\zeta + \frac{\eta}{3} \right) \nabla (\nabla \cdot \mathbf{v}) \quad (4.4)$$

where ρ , \mathbf{v} , Ze and P are the mass density, fluid velocity, charge and pressure of the dust grains respectively. Coefficients of shear and bulk viscosity are η and ζ respectively. Kinematic viscosity is given by $\nu = \eta/\rho$ and ϕ is the electrostatic potential. The viscoelastic relaxation time τ_m is a measure of how memory effects due to strong coupling will influence the growth of instability in the medium. Taking curl of Equation 4.4, we get the generalized

hydrodynamic vorticity equation

$$(1 + \tau_m \partial_t)(\partial_t \omega + (\mathbf{v} \cdot \nabla) \omega) = \nu \nabla^2 \omega \quad (4.5)$$

Equation 4.5 can be perturbed by writing velocity and the vorticity in $(\hat{r}, \hat{\theta})$ as

$$\mathbf{v} = (v'_r, V_0 + v'_\theta), \quad \omega = \omega_0 + \omega' \quad (4.6)$$

where the quantities with primes are perturbed quantities. Using Equation 4.6, the linearized z-component of Equation 4.5 becomes,

$$(1 + \tau_m \partial_t) \left[\left(\partial_t + \frac{V_0}{r} \partial_\theta \right) \omega' + v'_r \frac{d\omega_0}{dr} \right] = \nu \nabla^2 \omega' \quad (4.7)$$

Assuming continuity of mass ($\nabla \cdot \mathbf{v} = 0$), we introduce the stream-function $\Psi' = (0, 0, \Psi')$ and write the perturbed velocities as $v'_r = (1/r) \partial_\theta \Psi'$ and $v'_\theta = -\partial_r \Psi'$. Using Equation 4.7 and along with the fact that $\omega' = -\nabla^2 \Psi'$, we get

$$(1 + \tau_m \partial_t) \left[\left(\partial_t + \frac{V_0}{r} \partial_\theta \right) \nabla^2 \Psi' - \frac{1}{r} \partial_\theta \Psi' \frac{d\omega_0}{dr} \right] = \nu \nabla^4 \Psi' \quad (4.8)$$

Taking normal mode ansatz: $\Psi' = \Phi' \exp(\gamma t + im_n \theta)$, it is easily seen that Equation 4.8 becomes

$$(1 + \tau_m \gamma) \left[\left(\gamma + \frac{im_n V_0}{r} \right) \left(D_* D - \frac{m_n^2}{r^2} \right) - \frac{im_n}{r} \frac{d\omega_0}{dr} \right] \Phi' = \nu \left(D_* D - \frac{m_n^2}{r^2} \right)^2 \Phi' \quad (4.9)$$

where $D = d/dr$ and $D_* = d/dr + 1/r$. Equation 4.9 is an eigen value equation and can be numerically solved for the eigen value γ . Typically, the viscoelastic relaxation time τ_m (Berkovsky, 1992) depends on Γ and is given as

$$\tau_m = \frac{(4\eta/3 + \zeta)\Gamma}{(3 - \Upsilon \mu_d)n + 4u/15} \quad (4.10)$$

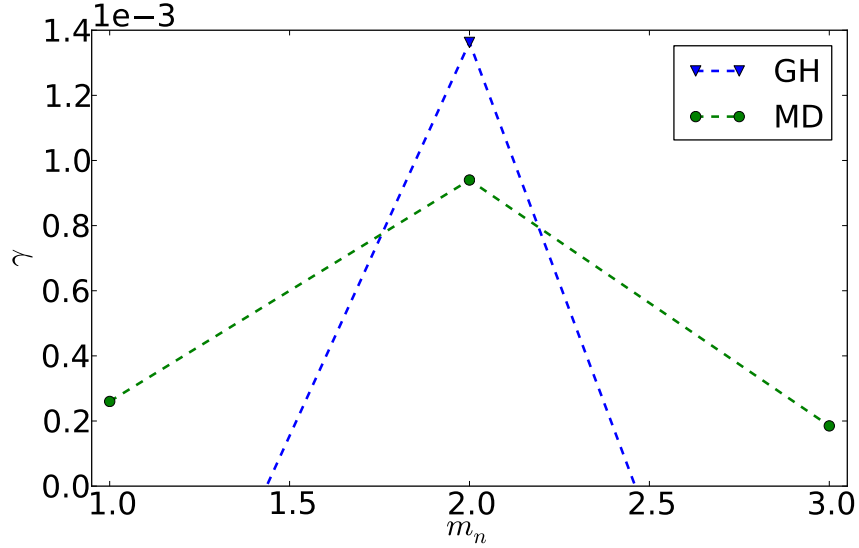


Figure 4.5: Growth rate spectrum (solid circles) of centrifugal instability calculated from MD simulations at $\Gamma = 50$. Each point on the curve is obtained from the slope of the straight line fit to linear growth of the perturbed radial kinetic energy (Figure 4.4). For comparison, the growth rates calculated from GH model (Equation 4.9) at $\nu(\Gamma) = 0.56$ and $\tau_m = 2.56$ (see Figures 3.12 and 3.13 line-symbols).

where, Υ is the adiabatic index, which for a 2D system is taken as 2 and μ_d is the compressibility. Thus, we find the value of $\tau_m \approx 2.56$ at $\Gamma = 50$ (see Figures 3.12 and 3.13 line-symbols). In Figure 4.5, we show a comparison between the linear growth rate spectrum of the centrifugal instability directly obtained from MD simulations at $\Gamma = 50$ (solid circles) and the spectrum obtained from GH model (Equation 4.9 and solid triangles). We find that for the profile given by Equation 4.2, the GH model (solid triangles) predicts only two unstable modes namely $m_n = 2, 3$. The GH growth rates though larger in magnitude appear to be in qualitative agreement with MD growth rates. It will be interesting to extend the present GH model by including a convective term ($\tau_m \mathbf{v} \cdot \nabla$) in the viscoelastic memory operator ($1 + \tau_m \partial_t$) as proposed by (Frenkel, 1946) and compare with MD results. This will be described in the future work section.

4.6 Summary

In summary, we have demonstrated for the first time, through large scale MD simulations, the emergence of isolated coherent tripolar vortices from the decay of unstable axisymmetric flows in strongly coupled Yukawa liquids. Linear growth rates of the instability are directly obtained from “first principles” MD simulations and emergence of coherent tripolar vortices in the non-linear regime is reported. The tripoles formed are very robust and persist for several eddy turnover times. An attempt is made to compare the growth rates obtained from MD simulations with the GH fluid model. Several important questions can be addressed in the context of the present work such as the enhancement of transport length scales due to these coherent tripolar vortices, inertial power laws and inverse cascade phenomena in 2D turbulent strongly coupled liquids. Our work expands the possibility of observing such tripolar vortices in laboratory experiments on complex plasmas, condensed matter systems and astrophysical systems such as white dwarfs thereby vastly extending the generality of the phenomenon.

In the foregoing chapter it was seen that a tripolar vortex under certain conditions can spontaneously decay into a pair of dipolar vortices propagating in mutually opposite directions (see Figure 4.3, bottom-right). One naturally wonders if it is possible to excite such dipolar vortices from generic initial conditions and study their interactions in a laboratory produced complex plasma. In the following chapter, the emergence of dipolar vortices from the self organization of an initial jet profile in a 2D strongly coupled Yukawa liquid is discussed in detail.

Chapter 5

Formation and Interaction of Dipoles

Coherent dipolar vortices are a universal outcome of injecting linear momentum into a liquid. Once formed, these dipolar vortices can transport mass and momentum over large length scales and are hence a subject matter of intense research work. In the present chapter, using “first principles” classical molecular dynamics simulations, we report for the first time, formation and collision of dipolar vortices in a two-dimensional prototype strongly coupled liquid, namely the Yukawa liquid. A dipolar vortex is seen to emerge from the self-organization of a sub-sonic jet profile. This dipole is seen to be very robust and, in general, shows a nonlinear relationship between vorticity and stream function. Starting from two jets injecting linear momentum in mutually opposite directions, we report on the centered head-on collisions between two dipolar vortices. Effect of neutral gas friction on the evolution of dipole is also investigated.

5.1 Introduction

Dipolar vortices are well known steady state solutions of the two-dimensional (2D) Euler equation ([Lamb, 1932](#)). They are one of the most fundamental vortical structures of 2D flows and display a remarkable ability to trans-

port both mass and momentum (Couder and Basdevant, 1986). A typical dipolar vortex consists of two closely packed monopolar vortices of opposite circulation and can be excited in laboratory experiments and numerical simulations of 2D flows of ordinary liquids (Van Heijst and Flor, 1989; Nielsen and Rasmussen, 1997). In turbulent conditions, dipolar vortices are generally seen to be less stable than monopolar vortices observed in the sub-mesoscale studies of oceans (McWilliams, 1985) and numerical simulations of 2D turbulence (McWilliams, 1984). Dipolar vortices generated by a short fluid impulse were first studied by (Duc and Sommeria, 1988), who showed that a dipole once formed, can travel the entire system length and, in general, has a nonlinear relation between vorticity ω and stream function ψ . Subsequent experiments on dipole formation and collisions in a stratified liquid confirmed this fact (Van Heijst and Flor, 1989). Interestingly, a sinh relation [i.e $\omega = A \sinh(B\psi)$] has also been observed in the temporal evolution of Lamb dipoles (Van Geffen and Van Heijst, 1998). This has led to a great amount of research on the formation and evolution of the dipolar structures in ordinary liquids (Kramer et al., 2007).

To the best of our knowledge, the emergence of coherent dipolar vortices in such strongly coupled liquids is a new paradigm and as such poses several fundamental questions: Is it possible to form dipolar vortices by injecting momentum? Once formed, how do these dipolar vortices interact? Do they exchange mass? What is the typical lifetime of a dipolar vortex in such strongly coupled liquids? In chapter 4, we studied the evolution of axisymmetric flows in strongly coupled Yukawa liquids through classical molecular dynamics (MD) simulations. Coherent tripolar vortices were seen to emerge in the nonlinear regime. It was also shown that under certain conditions, a tripole can spontaneously decay into a pair of dipolar vortices propagating in mutually opposite directions. One naturally wonders if it is then possible to excite such dipolar vortices from generic initial conditions and study their interactions in a laboratory produced complex plasma. Using “first principles” classical MD simulations, the present paper reports on the emergence of such dipolar vortices from the self organization of a jet velocity profile in a prototype 2D strongly coupled liquid, namely, the Yukawa liquid. In the

following section we present a discussion on the MD simulations used in the present study.

5.2 Molecular dynamics

As is well known, a typical Yukawa liquid or a laboratory produced complex plasma consists of weakly ionized gas and charged dust grains and can be efficiently modeled by the Yukawa potential (Equation 2.1). In such a strongly coupled complex plasma, the coupling parameter $\Gamma = Q^2/(4\pi\epsilon_0 a T_d)$ can be easily of the order 1 or larger (T_d and a are the dust temperature and the Wigner-Seitz radius respectively). Complex plasma offer a natural testbed for several fluid dynamics studies and various authors have investigated the flows in complex plasma by theoretical (Ashwin and Ganesh, 2010a, 2011b; D'Angelo and Song, 1990) and experimental methods (Nosenko and Goree, 2004). The state of strong coupling in complex plasma is manifested through the introduction of memory dependent viscoelastic coefficients - a generalized hydrodynamic approach followed by some authors (Kaw and Sen, 1998). However, the validity of these models across a wide range of coupling parameter remains unclear (Ashwin and Ganesh, 2010b; G. J. Kalman, M. P. Rommel and K. B. Blagoev (Eds.), 1998). Hence, for an “exact” description of these strongly coupled liquids, one should invoke “first principles” classical MD simulations and numerically solve the N body problem.

In the present paper, we report on the emergence, evolution and interaction of coherent dipolar vortices in a 2D strongly coupled Yukawa liquid. As defined in chapter 2, when dust-neutral collisions are included, the particle motion is modeled by the following coupled equations:

$$m\ddot{\mathbf{r}}_i = \mathbf{f}_i + m\nu_{dn}\dot{\mathbf{r}}_i \quad (5.1)$$

where ν_{dn} is the friction coefficient arising due to neutral gas and \mathbf{f}_i is the

Yukawa force,

$$\mathbf{f}_i = -\frac{Q^2}{4\pi\epsilon_0} \sum_{j \neq i}^N \nabla \left(\frac{\exp(-r_{ij}/\lambda_D)}{r_{ij}} \right) \quad (5.2)$$

The length, time, velocity and energy are normalized to a , Ω_{pd}^{-1} , $a\Omega_{pd}$ and $Q^2/(4\pi\epsilon_0 a)$, respectively. The 2D plasma frequency is given by

$$\Omega_{pd} = [Q^2 n / (4\epsilon_0 m a)]^{1/2} \quad (5.3)$$

where n and m are the 2D dust number density and mass of the dust grain, respectively. We take a total of 2.304×10^5 grains for the 2D Yukawa liquid and periodic boundary conditions along \hat{x} and \hat{y} . The number density n of the Yukawa liquid is taken to be 1, which gives us a square region of size $L = 480$, centered at origin $(0,0)$. This corresponds to a system of size of $19.2 \text{ cm} \times 19.2 \text{ cm}$ in physical units for a typical $a = 0.4 \text{ mm}$. The value of screening parameter $\kappa = a/\lambda_D = 0.5$ in all our simulations. The initial state is prepared by connecting the 2D system to a Gaussian thermostat (Evans et al., 1983) and letting it evolve canonically for $200\Omega_{pd}^{-1}$. Onto this thermally equilibrated Yukawa liquid, the following jet velocity profile is superposed on grain velocities (only once at time $t = 0$):

$$V_x = 0.5V_0 \exp(-(y/y_0)^M) [1 - \tanh(\alpha(x - x_0))] \quad (5.4)$$

where, V_0 is the magnitude of the maximum velocity of the dust grains in the jet, x_0 is the parameter which controls the length the jet. The parameters y_0 and M control the fall of V_x along \hat{y} direction. The fall of V_x at $x = x_0$ is controlled by the parameter α . Parameter values are listed as follows: $V_0 = 1.3$, $M = 2$, $y_0 = 30$, $x_0 = 150$ and $\alpha = 0.25$. In normalized units, the adiabatic sound speed measured for the system $c_s \approx 2.4$ and the typical thermal speed $v_{th} = \sqrt{(2/\Gamma)} \approx 0.13$, at $\Gamma = 120$. Hence, one may think of the present study as ‘‘incompressible’’ in nature. Our choice of the jet velocity profile is physically motivated by extensive laboratory experiments on ordinary fluids (Van Heijst and Flor, 1989; Duc and Sommeria, 1988).

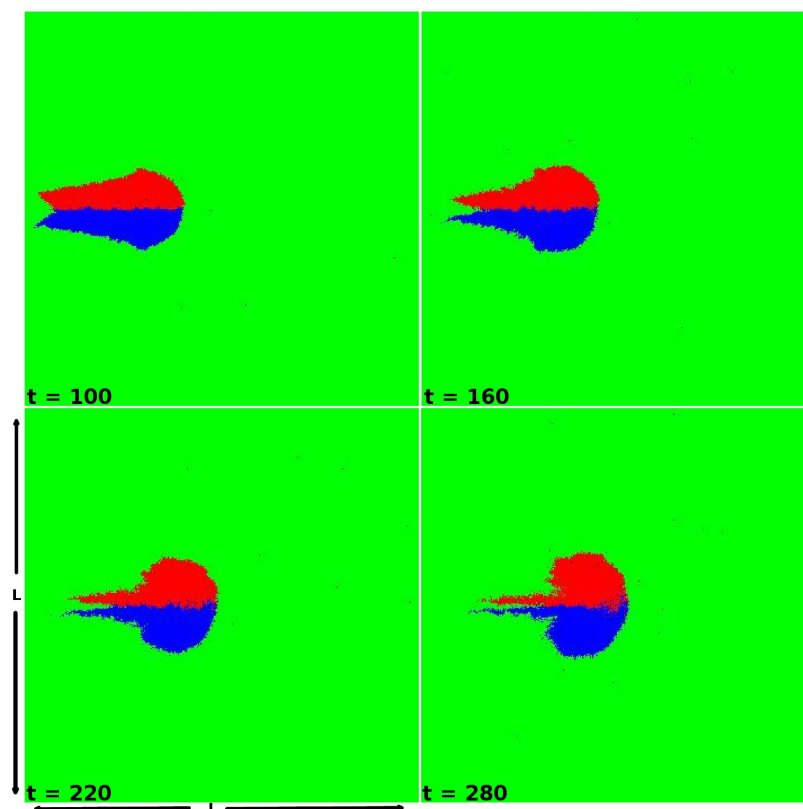


Figure 5.1: Sequence of images showing the evolution of a jet profile (Equation 5.4) when $\nu_{dn} = 0$. Grains inside the jet are colored red if the local vorticity is positive and colored blue if the local vorticity is negative. Grains in the background fluid are colored pale green. It should be noted here that only grains with horizontal velocity greater than $20\%V_x$ are considered to be inside the jet, remaining contribute to the background fluid [$L = 480$].

Such a jet profile given by Equation 5.4 may also be produced in a strongly coupled complex plasma by driving a laser beam under controlled laboratory conditions (Nosenko and Goree, 2004).

In Figure 5.1, we provide a sequence of images showing the evolution of the jet profile [Equation 5.4] in the absence of dust neutral collisions ($\nu_{dn} = 0$). Each snapshot in Figure 5.1 is shown for the full system ($\pm 240, \pm 240$). Grains forming the jet and the background are appropriately color coded (see caption for details). At a time $t = 220$ into the simulation, with initial $\Gamma = 120$, a dipole is seen to emerge from the self organization of an initial jet profile.

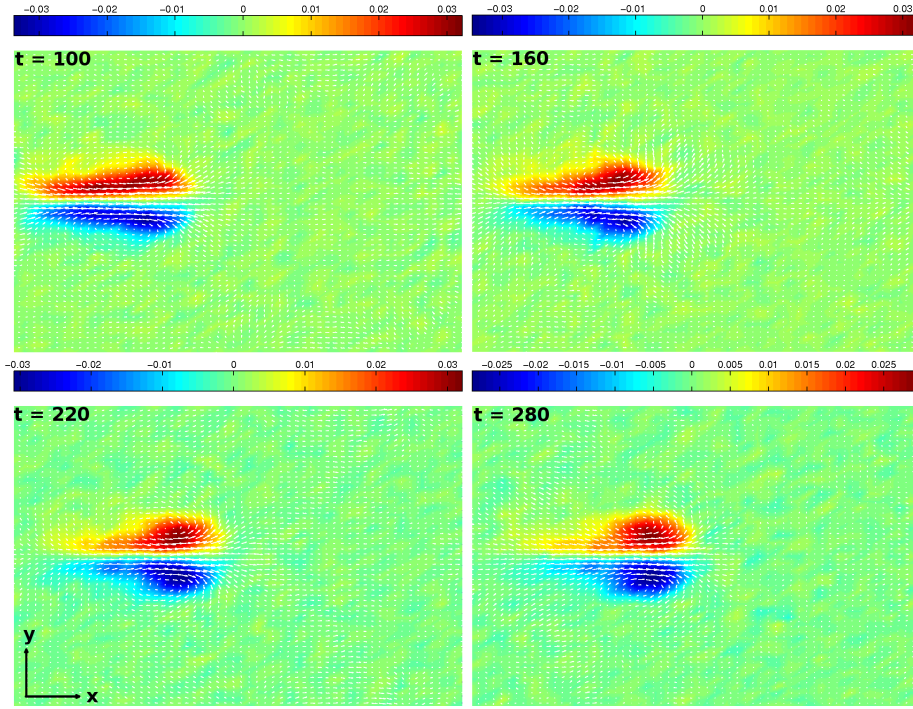


Figure 5.2: Snapshots showing evolution of a dipole with $\nu_{dn} = 0$ starting from an initial $\Gamma = 120$. Grain velocities in the region are fluidized through a 45×45 grid to construct local velocity (shown as white arrows) and local vorticity ω (see color-bar).

Once formed, it propagates horizontally through the entire system, with only minor changes in its shape.

In Figure 5.2, we show the corresponding vorticity contour plot at various times in the absence of gas friction. The snapshots are shown for the full system and one can clearly see a compact region having two patches of oppositely signed vorticities. The net circulation of the dipole is zero and it is seen to be a very robust structure, persisting long enough to travel the entire length of the system. The magnitude of local vorticity $\omega = \nabla \times \mathbf{v}$ (see vertical color-bar) is obtained by “fluidizing” the grain velocities over a 45×45 grid. This amounts to a local averaging of grain velocities to obtain fluid velocity at a grid point. The superposed arrows indicating the local flow direction are obtained similarly from a 60×60 grid. For the case $\nu_{dn} = 0$, the peak density fluctuation in the system $\delta n = |[n(x, y) - n_0]/n_0| \times 100 \approx 7\%$

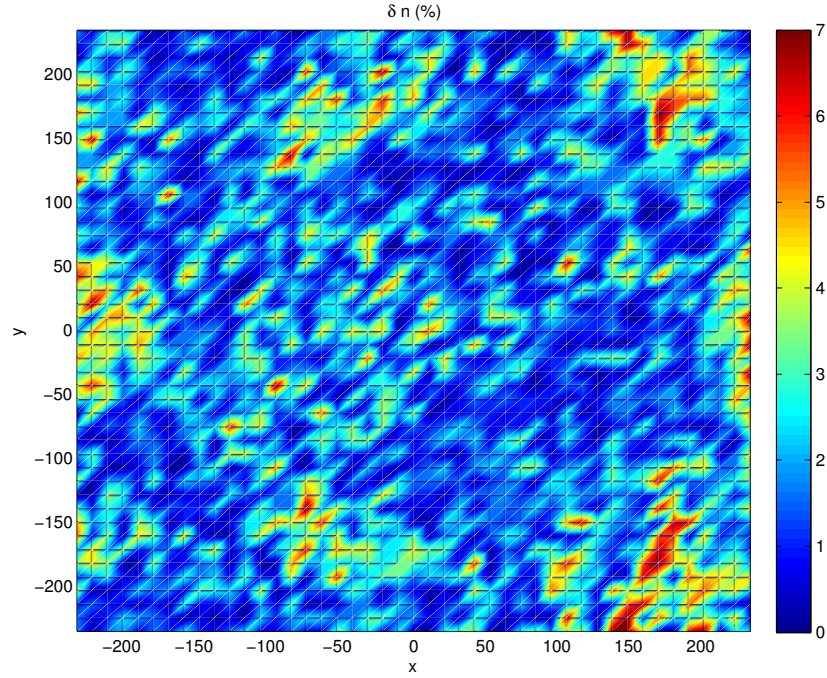


Figure 5.3: Contour plot of density fluctuation $\delta n = |[(n(x, y) - n_0)/n_0] \times 100| \approx 7\%$ at $t = 220$. Here $n_0 = 1$.

at $t = 220$ [see Figure 5.3]. Neglecting density variation (assuming “incompressibility”), we then calculate the stream function ψ from the following line integral : $\psi(\mathbf{r}) = \int (v_x dy - v_y dx)$. In Figure 5.4, we present a typical scatter plot at $t = 220$ for the flow field in the entire system for the case $\nu_{dn} = 0$. The nonlinear relationship between ω and ψ is clearly evident from the polynomial fit (solid line). Similar nonlinear relationship has been observed in past experimental studies on dipolar structures in ordinary liquids (Duc and Sommeria, 1988; Van Heijst and Flor, 1989). In the following section, we observe the viscous decay of the dipole through time evolution of peak vorticity and kinetic energy of the dipole.

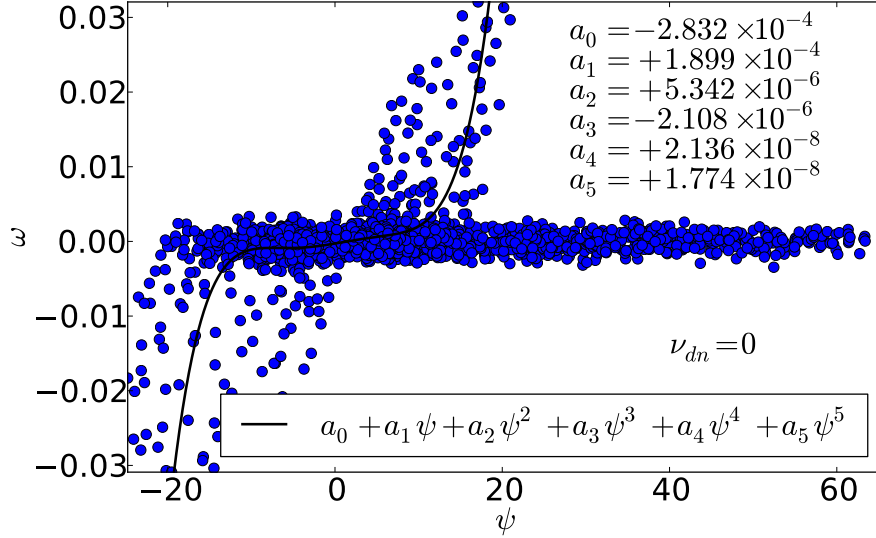


Figure 5.4: Scatter plot of vorticity ω and stream function ψ in the flow field associated with the dipolar vortex at $t = 220$, starting from an initial $\Gamma = 120$ and $\nu_{dn} = 0.0$. Each point on the scatter plot represents a pair of (ω, ψ) values obtained after fluidizing grain velocities on a 45×45 grid. The band of zero vorticity represents the region outside the dipole, whereas the branches of positive and negative vorticity correspond to the dipolar vortex. The nonlinear (ω, ψ) relation within the dipole is evident from the fitted polynomial (solid line).

5.3 Viscous decay

To further understand the time evolution of a dipole, we obtain the dipole kinetic energy

$$\bar{E}_k = (0.5/N_d) \sum_i^{N_d} v_{xi}^2 \quad (5.5)$$

directly from MD simulations. Here N_d stands for the number of grains within the dipole. In Figure 5.5, we show the plots showing temporal variation of peak vorticity $\bar{\omega}_x$ and kinetic energy \bar{E}_k of the evolving dipole as a function of time, normalized to unity at $t = t_F$, where $t_F = 220$ is the time at which the dipole is formed. The fall in dipole kinetic energy along with decay of peak vorticity ω_m is due to high fluid viscosity (Nielsen and Rasmussen,

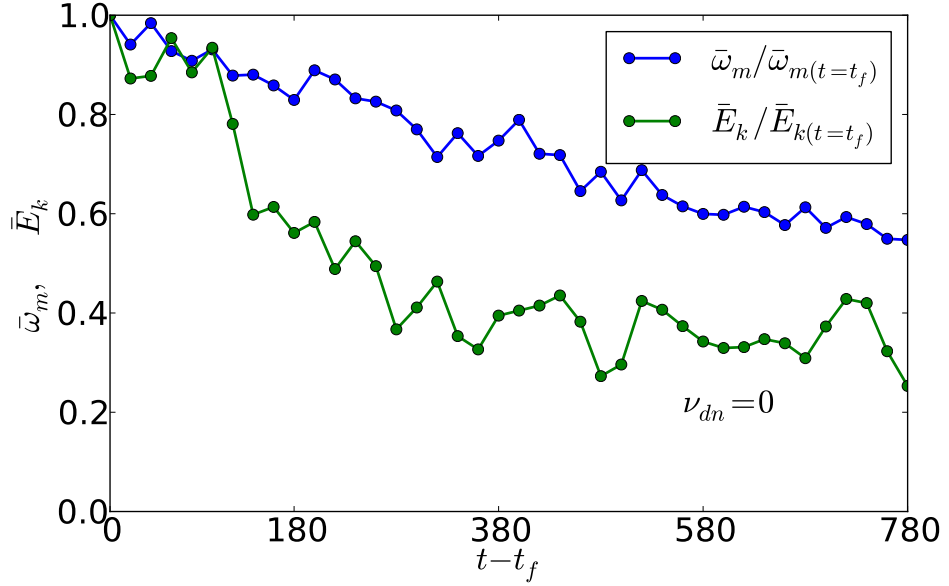


Figure 5.5: Peak vorticity $\bar{\omega}_m$ and kinetic energy \bar{E}_k of the evolving dipole as a function of time, normalized to unity at $t = t_f$ ($t_f = 220$, is the time at which the dipole is formed). The dust neutral collisions are absent or $\nu_{dn} = 0$. It is clear seen that the dipole slows down, along with the fall in ω_m . This is due to viscous effects (Nielsen and Rasmussen, 1997; Van Geffen and Van Heijst, 1998) dominant in a typical strongly coupled liquid. It should be noted that both peak vorticity and kinetic energy is faster at higher values of gas friction.

1997; Van Geffen and Van Heijst, 1998), which is a typical characteristic of a strongly coupled Yukawa liquid. In the following section, we present a discussion on the head on collision between two dipoles in such a frictionless limit.

5.4 Dipole interactions

The persistent behavior of dipolar vortex structures is observed in following simulations on frontally colliding dipoles (Figure 5.6a,b). We present the following dipole interaction study in the limit of vanishing gas friction or $\nu_{dn} = 0$. Starting from a thermally equilibrated liquid at $\Gamma = 120$, two jets [Equation 5.4] were excited at opposite locations $(\pm 240, 0)$ at time $t = 0$. The colliding dipoles are symmetric and they exchange partners which results into

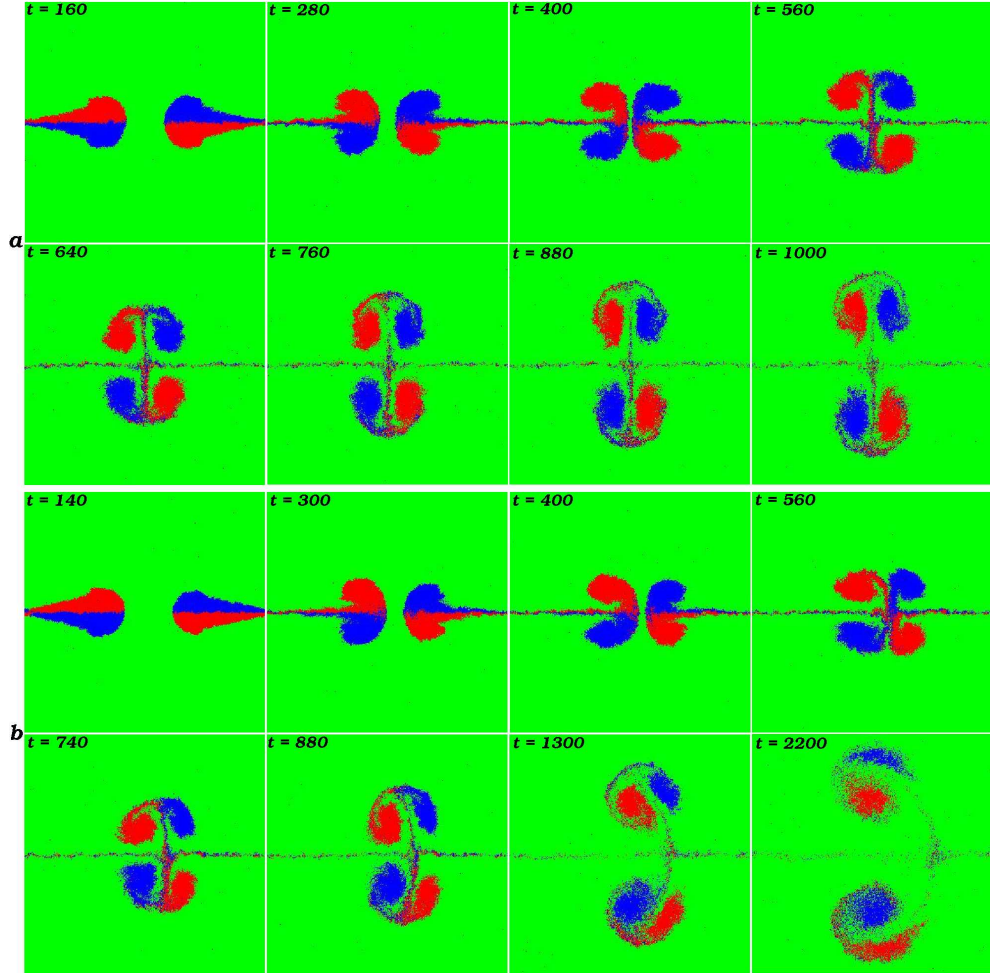


Figure 5.6: (a.) Snapshots showing stages of centered head-on collision between two dipoles of equal strength with $\nu_{dn} = 0$. Grains inside a jet are colored red if the local vorticity is positive and colored blue if the local vorticity is negative. Grains in the background fluid are colored pale green. It should be noted here that only grains with horizontal velocity greater than $20\%V_x$ (Equation 5.4) are considered to be inside a jet, the remaining contribute to the background fluid. Parameters $V_0 = 1.3$, $y_0 = 30.0$ for both the jets. (b.) Same as in (a.), but with dipoles of unequal strength. ($V_0 = 1.3$, $y_0 = 30.0$) for the left dipole and ($V_0 = 1.0$, $y_0 = 26.25$) for the right dipole.

the formation of two new dipoles moving along a straight line away from the collision area. This new axis of motion is exactly perpendicular to the original axis (Figure 5.6a). Particle color coding reveals that no mass is exchanged between the partners: except for some very few “streamers” wrapped around the respective new partners - an effect due to thermal fluctuations at the initial contact. The dipoles thus appear to conserve their mass. In the second run (Figure 5.6b), a centered head-on collision was created between two dipoles of slightly different strength and size. This was achieved by taking $(V_0 = 1.3, y_0 = 30.0)$ for the left dipole and $(V_0 = 1.0, y_0 = 26.25)$ for the right dipole. As before, the dipoles exchange partners (without any mass transfer between them) and the newly formed dipoles move away from the collision area. In a stark contrast, however, the newly formed dipoles are not symmetric (as they are of different size and strength), and as a consequence they leave out on a looping excursion. In our simulations, these newly formed dipoles become progressively slower and approach the periodic boundaries. So far we have shown the results of our MD simulations in limit of vanishing gas friction. It will be interesting to see the role played by finite gas friction on the evolution of these dipolar vortices. This is the subject matter of the following section.

5.5 Role of gas friction

Laboratory dusty plasma exist under finite neutral gas friction. The condensation of liquid “dusty” plasmas into a solid like state is routinely achieved by increasing the neutral gas pressure in ground based laboratory experiments. Hence it becomes important to study the role of neutral gas friction in the evolution of a dipolar vortex. In Figure 5.7(a,b,c), we show the time evolution of a dipole vortex at two different values of gas friction. It is easily seen from Figure 5.7 that inertial effects that are crucial for the evolution of a dipole are rapidly killed by the increasing gas friction. Hence, one may expect such dipolar structures to sustain for longer times only in the limit of low gas friction. In Figure 5.8(a,b), we show the time evolution of peak vorticity and kinetic energy of the dipole in presence of finite gas friction.

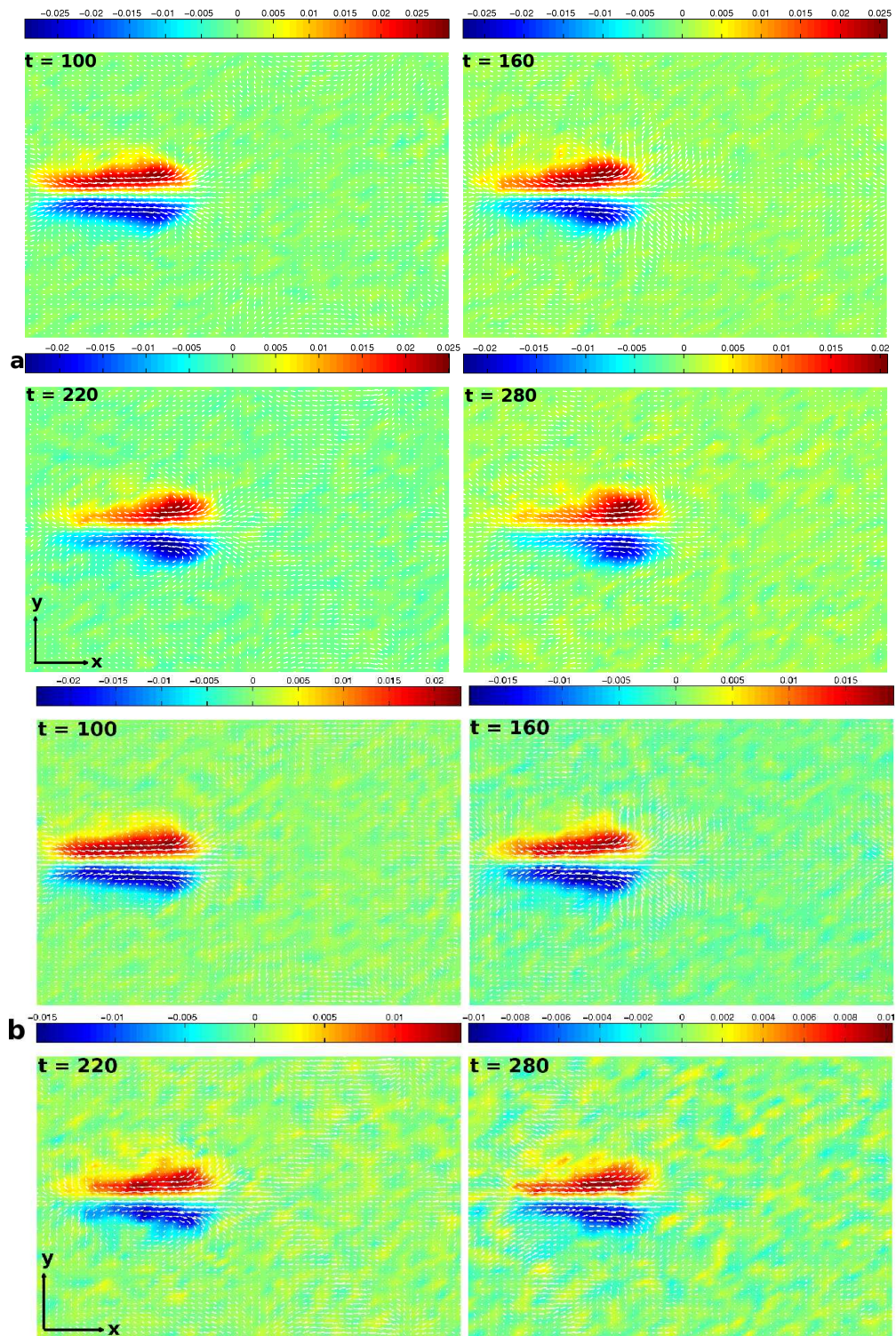


Figure 5.7: Time evolution of a dipole at two different values of gas friction, namely, (a.) $\nu_{dn} = 0.001$, (b.) $\nu_{dn} = 0.003$ and (c.) $\nu_{dn} = 0.007$. The inertial effects needed to sustain the dipole are rapidly quenched at higher values of gas friction.

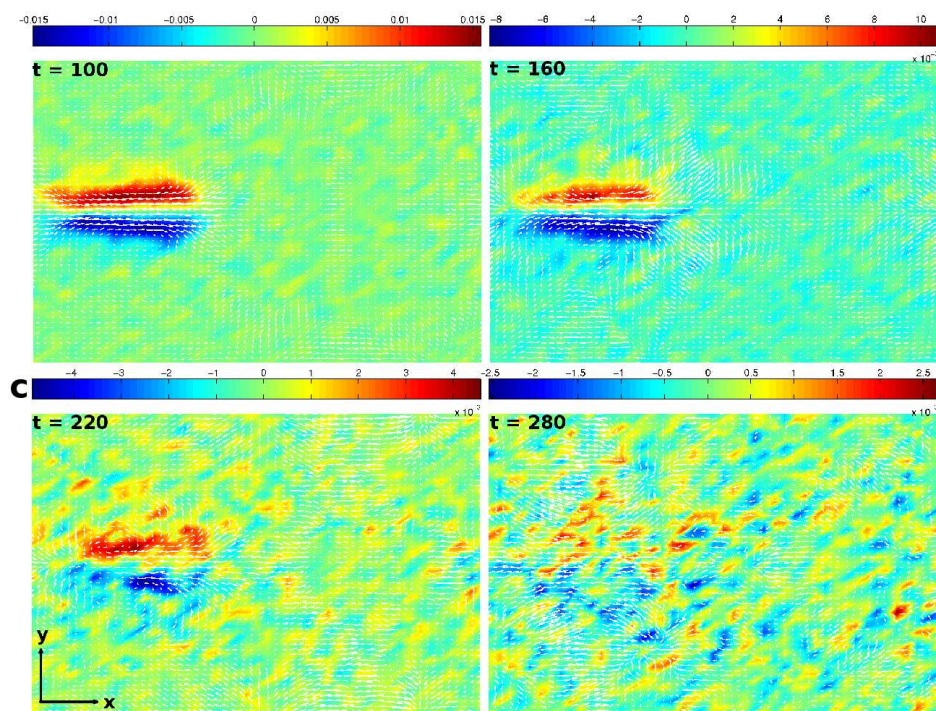


Figure 5.7: Continued

Once again, it is clear from these figures that the fall in both peak vorticity and kinetic energy is faster at higher values of gas friction.

5.6 Summary

In summary, we have reported, for the first time, through “first principles” classical MD simulations, the formation and collision of dipolar vortices in a prototype 2D strongly coupled Yukawa liquid. A dipolar vortex is seen to emerge from the self-organization of an initial sub-sonic jet profile, and, in general, is seen to have a nonlinear relation between vorticity and stream function. The dipoles formed are very robust and our simulations reveal that a centered head-on collisions between two such dipolar vortices results into exchange of partners but no mass is exchanged. For such dipoles to exist for longer times, the neutral gas friction needs to be small in value. At higher values of gas friction, the inertial effects needed to sustain a dipole are rapidly

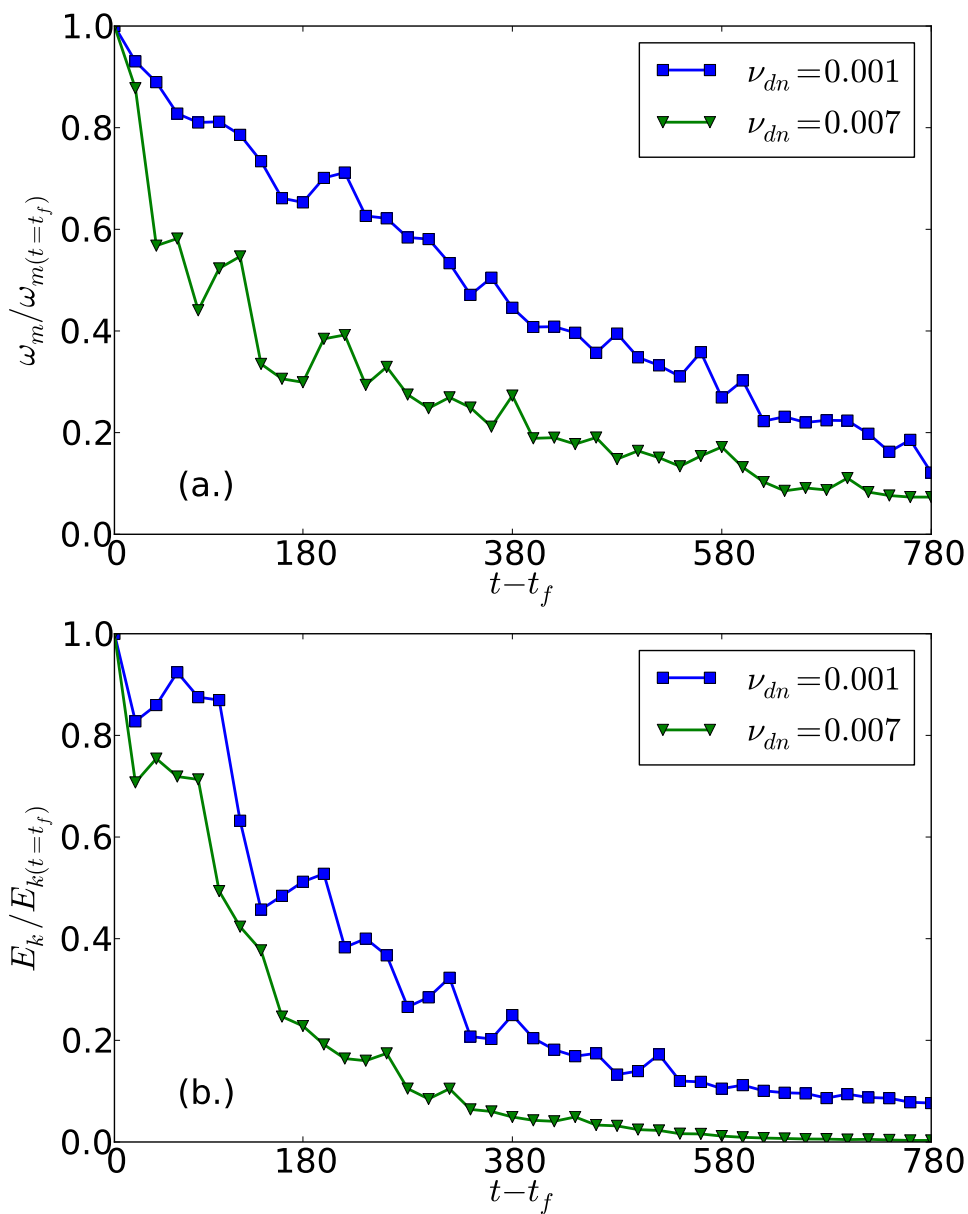


Figure 5.8: Time evolution of a dipole at two different values of gas friction, namely, (a.) $\nu_{dn} = 0.001$ and (b.) $\nu_{dn} = 0.007$. The inertial effects needed to sustain the dipole are rapidly quenched at higher values of gas friction.

quenched and the dipole is lost. For a comparison, it will be interesting to construct Lamb like solutions ([Lamb, 1932](#)) and perform nonlinear simulation of interacting jets using a lower dimensional generalized hydrodynamic model - an exercise which we defer for future work. Our work suggests the possibility of observing such dipolar vortices and their interactions in laboratory experiments on strongly coupled complex plasma at low values of gas friction, thereby, vastly extending the generality of the phenomenon.

Chapter 6

Heat Front Propagation

In the foregoing chapters on shear flow studies, generation of heat was observed at the particle level close to shear layers. It will be interesting to see if one can resolve the connection between such macroscopic shear flows and particle level heat generation. Here, we report using classical molecular dynamics simulations, the development and propagation of a nonlinear heat front in parallel shear flows of a strongly coupled Yukawa liquid. At a given coupling strength, a subsonic shear profile is superposed on an equilibrated Yukawa liquid and Kelvin Helmholtz (KH) instability is observed. Coherent vortices are seen to emerge towards the nonlinear regime of the instability. It is seen that while inverse cascade leads to a continuous transfer of flow energy towards the largest scales, at the smallest scale there is also a simultaneous transfer of flow energy into the thermal velocities of grains. The latter is an effect of velocity shear and thus leads to the generation of a nonlinear heat front. In the linear regime, the heat front is seen to propagate at speed much lesser than the adiabatic sound speed of the liquid. Spatio-temporal growth of this heat front occurs concurrently with the inverse cascade of KH modes.

6.1 Introduction

As is well known, complex plasmas can behave as essentially single phase systems when the grain-grain interactions dominate over the grain-plasma

interactions (Khrapak et al., 2004). Thus a near “exact” description of a complex plasma can be constructed by considering only the dust grains and assuming that the background plasma does not evolve in time. This allows the grain dynamics to be modeled by a Yukawa (screened Coulomb) potential (Equation 2.1). The resulting N body problem can then be numerically solved using a molecular dynamics (MD) simulation. In past, several authors have used such MD simulations to study transport phenomena (Saigo and Hamaguchi, 2002; Liu and Goree, 2005, 2008), phase transition (Hamaguchi et al., 1996, 1997; Ashwin and Ganesh, 2009) and collective behavior (Ohta and Hamaguchi, 2000b) in strongly coupled complex plasmas. There exists, however, a class of problems in complex plasmas where such a “first principles” study has so far, remained elusive. These are the “hydrodynamic instabilities”- a subject traditionally studied only through continuum methods. Recently, some of these hydrodynamic instabilities such as “shear flows” have been investigated at the most fundamental level of atomic motion by MD simulations of complex plasmas, for details, see chapter 3 and (Ashwin and Ganesh, 2010a,b, 2011b). In these works, it was noticed, that in addition to generation of coherent structures, shear flows also lead to “particle heat generation”. Such shear induced heat generation has been known to cause solid to liquid phase transition in soft materials (Ackerson and Clark, 1981; Delhommelle, 2004) and complex plasmas (Nosenko and Goree, 2004). Recently, shear induced melting has also been discovered in two-dimensional (2D) Yukawa crystals, where a melting front was seen to propagate at transverse sound speed (Feng et al., 2010). In the following section, we give details of the MD simulations carried out in the present chapter.

6.2 Molecular dynamics

In a typical large scale MD simulation like ours, one can control the grain-grain interactions using the switch ‘ κ ’ and obtain either ideal gas ($\kappa \rightarrow \infty$) or Coulomb gas ($\kappa \rightarrow 0$) behavior. We recall that the length, time and energy are normalized to a , Ω_{pd}^{-1} and $Q^2/(4\pi\epsilon_0 a)$ respectively. The dust plasma frequency is given by $\Omega_{pd} = [Q^2 n / (4\epsilon_0 m a)]^{1/2}$, where n and m are

the 2D dust number density and mass of the dust grain respectively. We take a total of 2.304×10^5 grains for the 2D Yukawa liquid and periodic boundary conditions are employed along \hat{x} and \hat{y} . The number density n of the Yukawa liquid is taken to be 1, which gives us a square region of size $L = 480$, centered at the origin $(0, 0)$. The value of screening parameter κ in our simulations is taken to be 0.5. The Yukawa liquid is first thermally equilibrated by connecting to a Gaussian thermostat (Evans et al., 1983) and letting it evolve canonically for $200\omega_{pd}^{-1}$. A standard leapfrog integrator with a time step $\Delta T = 0.01\omega_{pd}^{-1}$ is employed such that the fluctuation in total energy $\sim 10^{-5}\%$ without the thermostat over a typical run duration of $1000\Omega_{pd}^{-1}$. In the following section we report our results on Kelvin-Helmholtz instability due to a double step velocity profile.

6.3 Kelvin Helmholtz instability

The initial equilibrium is a thermally equilibrated Yukawa liquid at a desired Γ along the with the following step velocity profile superposed on grain velocities (only once at $t = 0$). Thus we have in Cartesian coordinates (x, y) :

$$V_x = \begin{cases} +V_0, & |y| \geq L/4 \\ -V_0, & |y| < L/4 \end{cases} \quad V_y = 0.0 \quad (6.1)$$

where $V_0 = 1$ is the magnitude of imposed velocity. The adiabatic sound speed of the system on this scale is $c_s \approx 2.4$ and the thermal speed is about $v_{th} = \sqrt{2/\Gamma} \approx 0.13$, at $\Gamma = 120$. Hence, our profile V_0 is “subsonic” in nature. In Figure 6.1, we show time evolution of KH instability starting from an equilibrated liquid at $\Gamma = 120$ and shear profile (Equation 6.1). A grain at time $t = 0$ (when the shear is imposed) is colored blue if $|y| \geq L/4$, else colored green. One can clearly see the development of KH instability and the roll up of vortices in the nonlinear regime eventually leading to turbulent mixing of the liquid. In the following section we present the time evolution of local vorticity ω and local flow field \mathbf{v} .

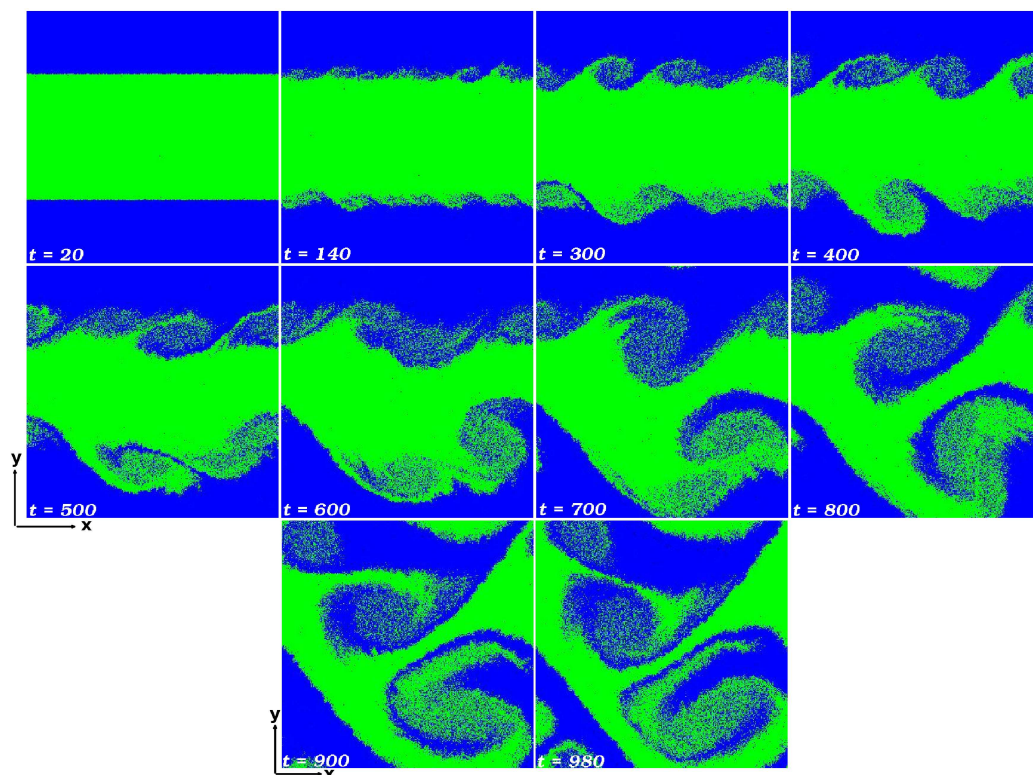


Figure 6.1: Blue colored fluid moves in the $+\hat{x}$ direction and green colored fluid moves in $-\hat{x}$ direction. Starting from an initial background $\Gamma = 120$, the snapshots are shown for the full system $(\pm 240, \pm 240)$ at different times. The development of KH instability leads to formation of vortices in the nonlinear regime. At late times $t \geq 800$, one can see the emergence of large coherent vortices due to inverse cascade which is typical of 2D turbulence [see Figure 6.5 for more detail].

6.4 Vorticity field

The development of KH instability leads to a nonlinear regime which is characterized by the formation of vortices. In Figure 6.2, we show a snapshot at $t = 400$ with well developed vortices in the nonlinear regime. The magnitude of local vorticity ($\boldsymbol{\omega} = \nabla \times \boldsymbol{v}$) is indicated on the vertical colorbar, where blue and red regions correspond to negative and positive values respectively. To construct local vorticity $\boldsymbol{\omega}$, we first obtain the local velocity \boldsymbol{v} by “fluidizing” grain velocities over a 45×45 grid. This amounts to a local averaging of grain velocities to obtain the fluid velocity at a grid point. The superposed white

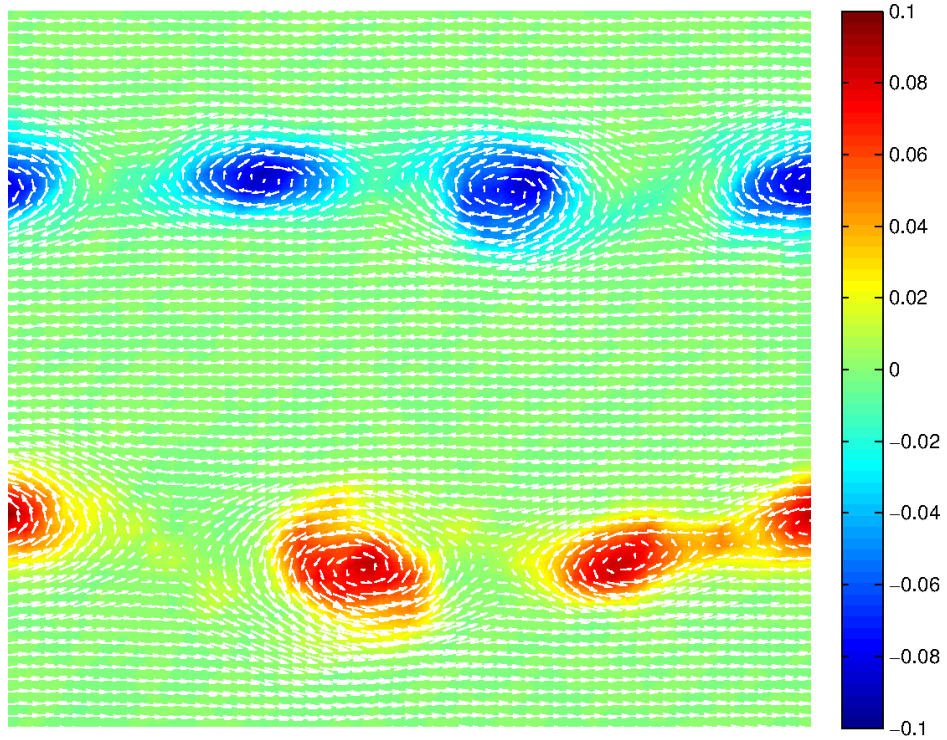


Figure 6.2: Vorticity field ($\omega = \nabla \times \mathbf{v}$) for the entire system $[\pm 240, \pm 240]$ shown at time $t = 400$ in the nonlinear regime. One can clearly see the developed vortices. Grain velocities in the region are fluidized through a 45×45 grid to construct local vorticity. Blue and red regions correspond to negative and positive vorticity respectively and the color-map label shows the magnitude of local vorticity. Arrows indicating direction of local velocity are obtained by fluidizing the grain velocities over a 60×60 grid. Arrow lengths give magnitude of local flow field qualitatively.

arrows showing the local flow direction are similarly obtained from a 60×60 grid. In Figure 6.3, we show the time evolution of this vorticity field through a sequence of vorticity (ω) snapshots for the full system $(\pm 240, \pm 240)$. At late times $t \geq 800$, one can clearly see the emergence of giant vortices due to inverse cascade of KH modes which is typical of 2D turbulence. In the following section, we present a discussion on the topology of this 2D turbulent field using the Okubo-Weiss criterion. The resulting Okubo-Weiss parameter \mathcal{Q} can then be used to divide the turbulent field into either “rotation dominated” or “deformation dominated” regions.

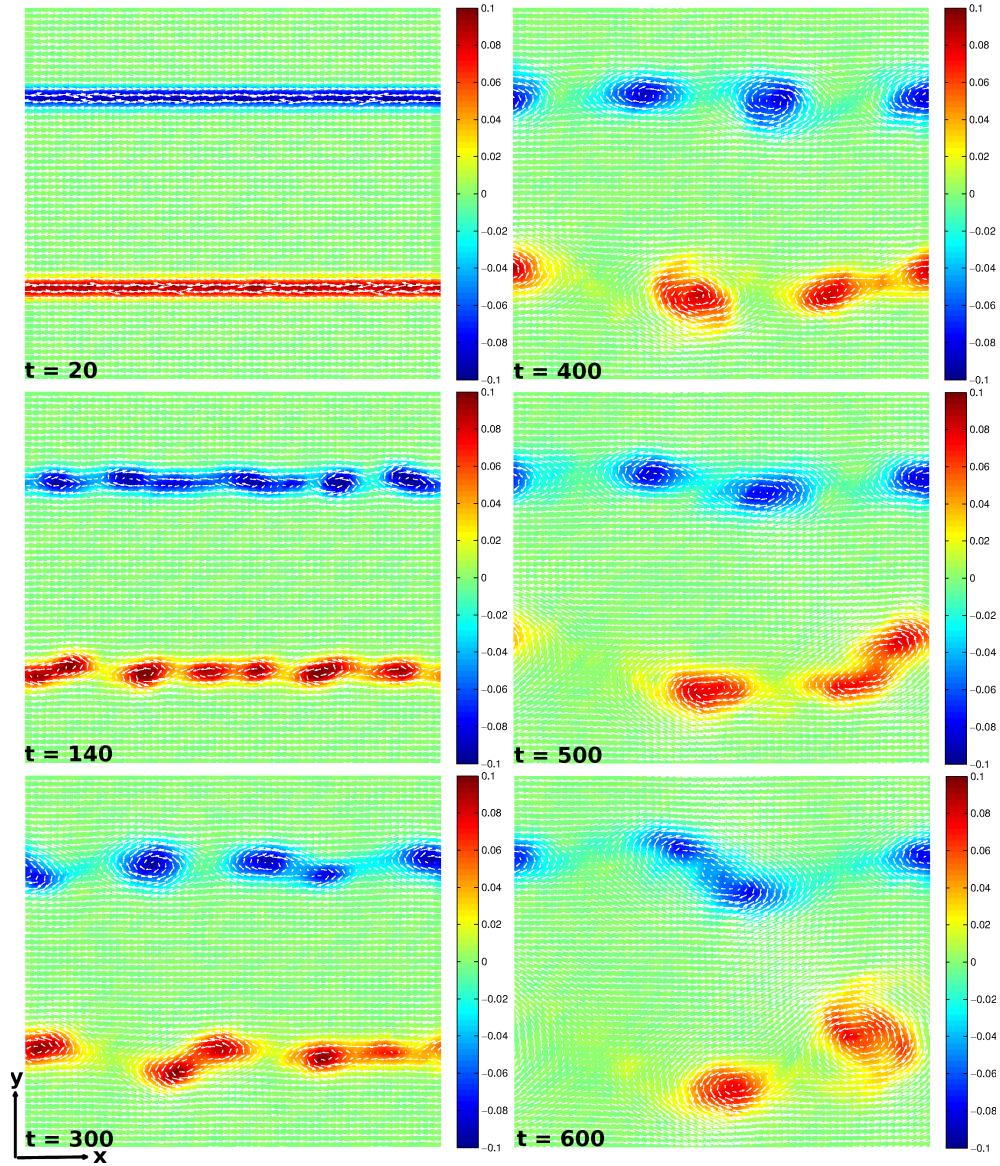


Figure 6.3: Snapshots showing vorticity ($\omega = \nabla \times \mathbf{v}$) contour plots for the full system ($\pm 240, \pm 240$). For details on extraction of ω and \mathbf{v} , see Figure 6.2 caption.

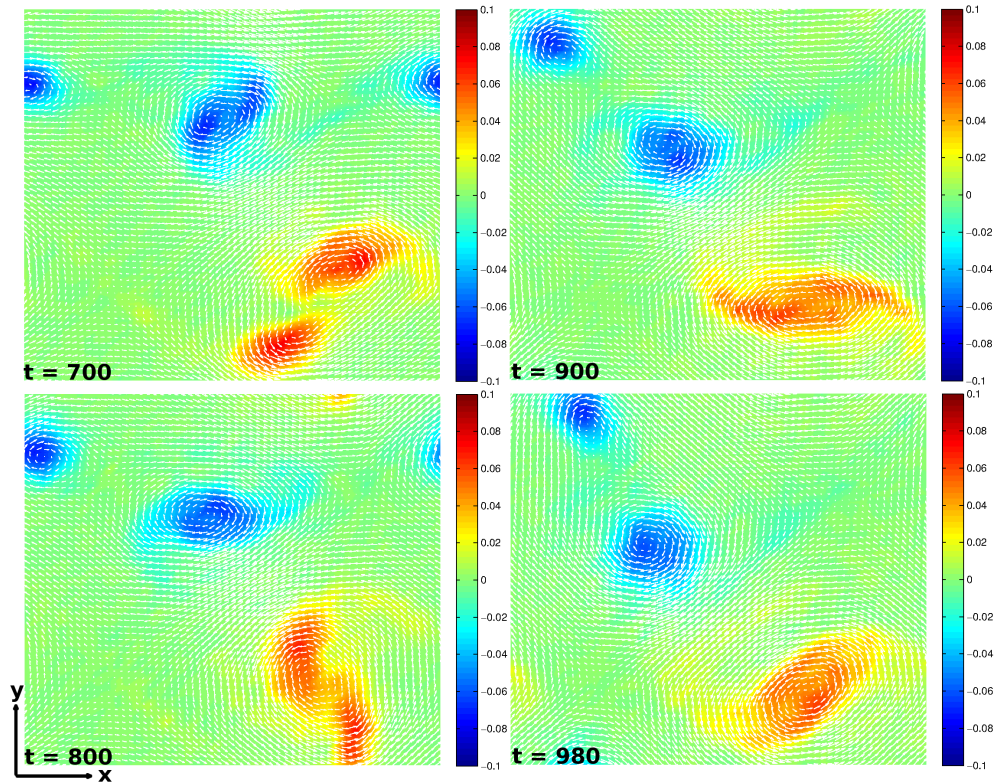


Figure 6.3: Continued

6.5 Topology of turbulent mixing

One can simplify the partition of a 2D turbulent field by distinguishing the contributions of rotation and deformation to the square of velocity gradient. This is done by writing,

$$\|\nabla \mathbf{v}\|^2 = \frac{1}{2}(\omega^2 + s^2) \quad (6.2)$$

where \mathbf{v} is the Eulerian velocity field, ω refers to the vorticity and s to the deformation, i.e

$$\omega = \partial_x v_y - \partial_y v_x, \quad s^2 = s_1^2 + s_2^2, \quad s_1 = \partial_x v_x - \partial_y v_y, \quad s_2 = \partial_x v_y + \partial_y v_x \quad (6.3)$$

Under the assumption that vorticity and strain (i.e spatial derivatives of velocity) are slowly varying with respect to the vorticity gradient, the Lagrangian evolution of $\nabla\omega$ is then given by a linear differential equation whose solution is (Okubo, 1970; Weiss, 1991; Elhmaidi et al., 1993)

$$\nabla\omega \approx \exp(\pm \frac{1}{2} \mathcal{Q}^{1/2} t) \quad (6.4)$$

where $\mathcal{Q} = s^2 - \omega^2$. Even though Weiss approximation holds in the limit of vanishing viscosity, it has also been used by several authors in presence of finite viscosity (Rivera et al., 2001; Perlekar and Pandit, 2009). The Okubo-Weiss parameter \mathcal{Q} provides a simplified picture of 2D turbulence by an elementary partition of the field into two distinct domains, namely (a) “elliptic domains” ($\mathcal{Q} < 0$), where rotation dominates deformation, $\omega^2 > s^2$, and (b) “hyperbolic domains” ($\mathcal{Q} > 0$), where deformation dominates rotation, $\omega^2 < s^2$.

Figure 6.4 shows contour plots of $\mathcal{Q}(x, y)$ at different times for the corresponding vorticity field shown in Figure 6.3. Based on the local value of \mathcal{Q} , we identify three regions, namely (a) vortex cores, which are characterized by strong negative values of \mathcal{Q} , (b) strain cells surrounding the vortex cores, which are characterized by large positive values of \mathcal{Q} , and (c) the background, where \mathcal{Q} fluctuates between positive and negative values. Depending on the sign of \mathcal{Q} , the background field may be further divided into non-coherent elliptic and hyperbolic patches. As the vortex cores show up in stark contrast to the background field, a \mathcal{Q} map is sometimes also used to count the number of vortices or coherent structures in the liquid. In the following section we present a quantitative analysis of inverse cascade of KH modes using Fourier transform of \hat{y} averaged kinetic energy.

6.6 Inverse cascade of KH modes

To further characterize the KH instability in detail, we obtain the power spectrum of modes as follows: On the 2D simulation box, we construct a (60×60) grid and calculate the \hat{y} averaged kinetic energy at various locations

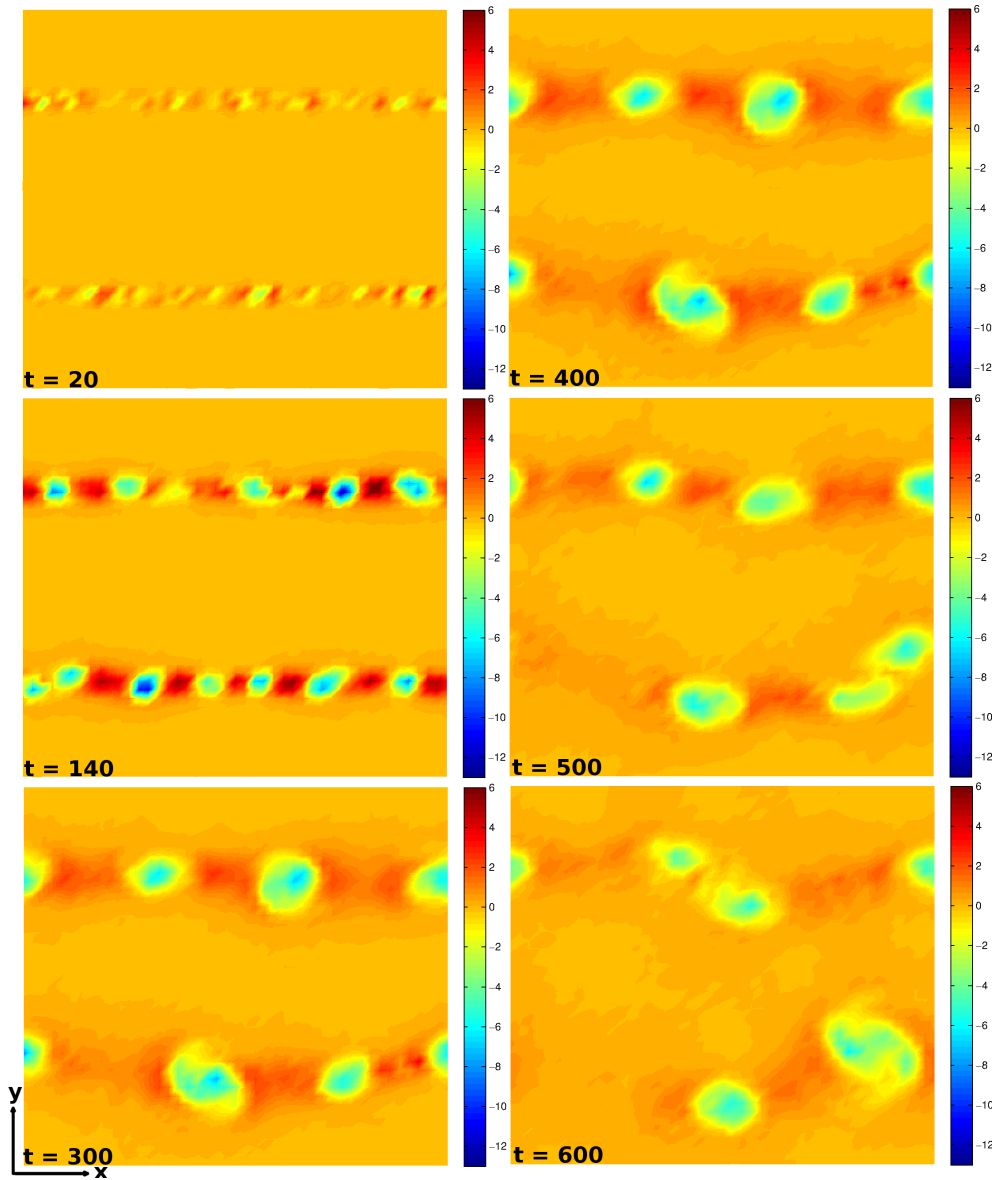


Figure 6.4: The field of Okubo-Weiss parameter Q ($\times 10^{-3}$) at corresponding times for the vorticity field shown in Figure 6.3. The positive (“hyperbolic domain”) and negative values (“elliptic domain”) of Q are indicated on the vertical colorbar.

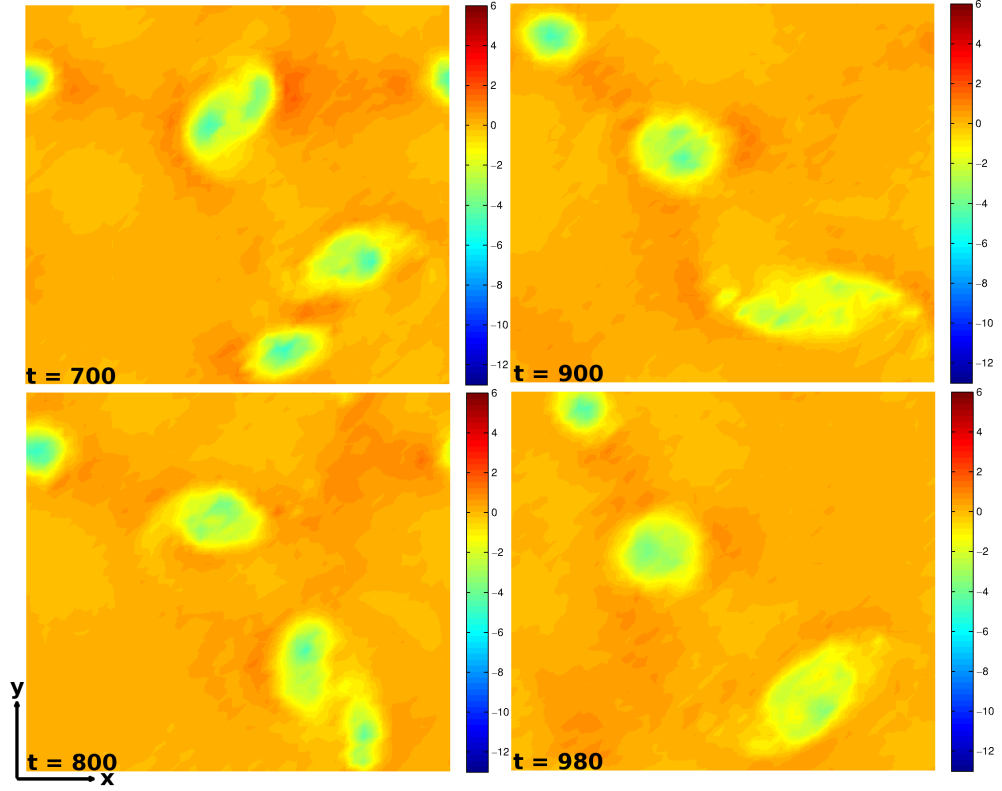


Figure 6.4: Continued

along \hat{x}

$$\bar{E}_k(x) = \frac{1}{L} \int_{-L/2}^{L/2} E_k(x, y) dy \quad (6.5)$$

where $E_k(x, y)$ is the kinetic energy per grain at the grid location (x, y) . By taking Fourier transform of this \hat{y} averaged kinetic energy $\bar{E}_k(x)$, we get the power spectrum of modes as follows:

$$E_k(m_n) = \int_{-\infty}^{\infty} \bar{E}_k(x) \exp\left(i \frac{2\pi m_n}{L} x\right) dx \quad (6.6)$$

where m_n is the mode number. In Figure 6.5, we show the power spectrum (normalized to the maxima) at similar times and quantitatively show inverse cascade of energy towards large scales (smaller m_n) which is typical

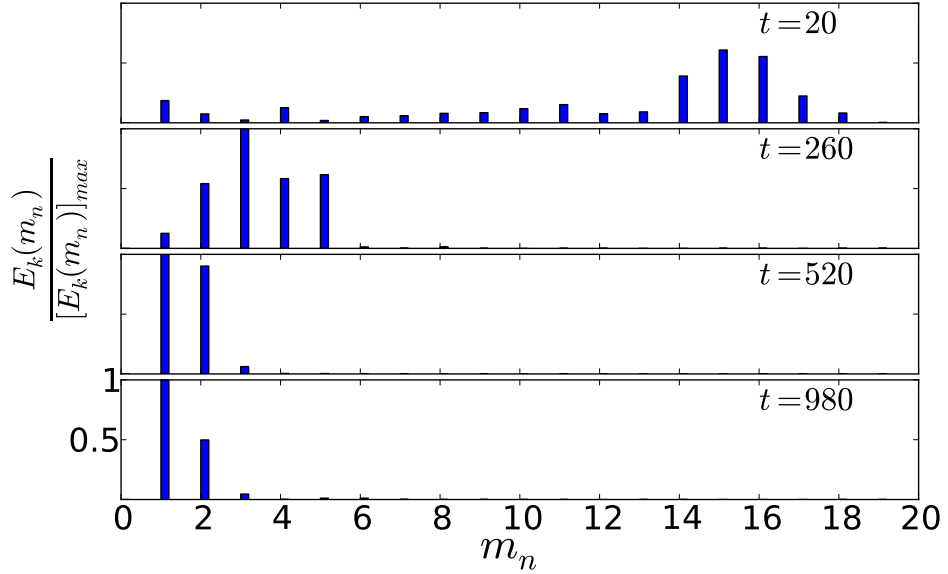


Figure 6.5: Power spectrum (normalized to the maxima) plotted at various times show the emergence of dominant mode $m_n = 1$ at late times. The initial excitation is random which is shown in the panel at $t = 20$. This inverse cascade of randomly excited modes to a dominant large scale structure ($m_n = 1$) at $t \sim 980$ is typical of 2D turbulence.

of 2D turbulence. This inverse cascade of KH modes is seen to concurrently evolve with the spatio-temporal growth of a nonlinear heat front, which is the subject matter of the following section.

6.7 Development and growth of heat front

At the smallest scales, particle heat generation due to velocity shear leads to the development of a heat front. The propagation of this heat front is elucidated through a time sequence of Γ contour plots as shown in Figure 6.6. A typical instantaneous plot of $\Gamma(x, y)$ field is obtained as follows:

$$\Gamma(x, y, t) = \frac{1}{\sum_i^{\mathcal{N}} \frac{1}{2}(\mathbf{v}_i - \bar{\mathbf{v}})^2} \quad (6.7)$$

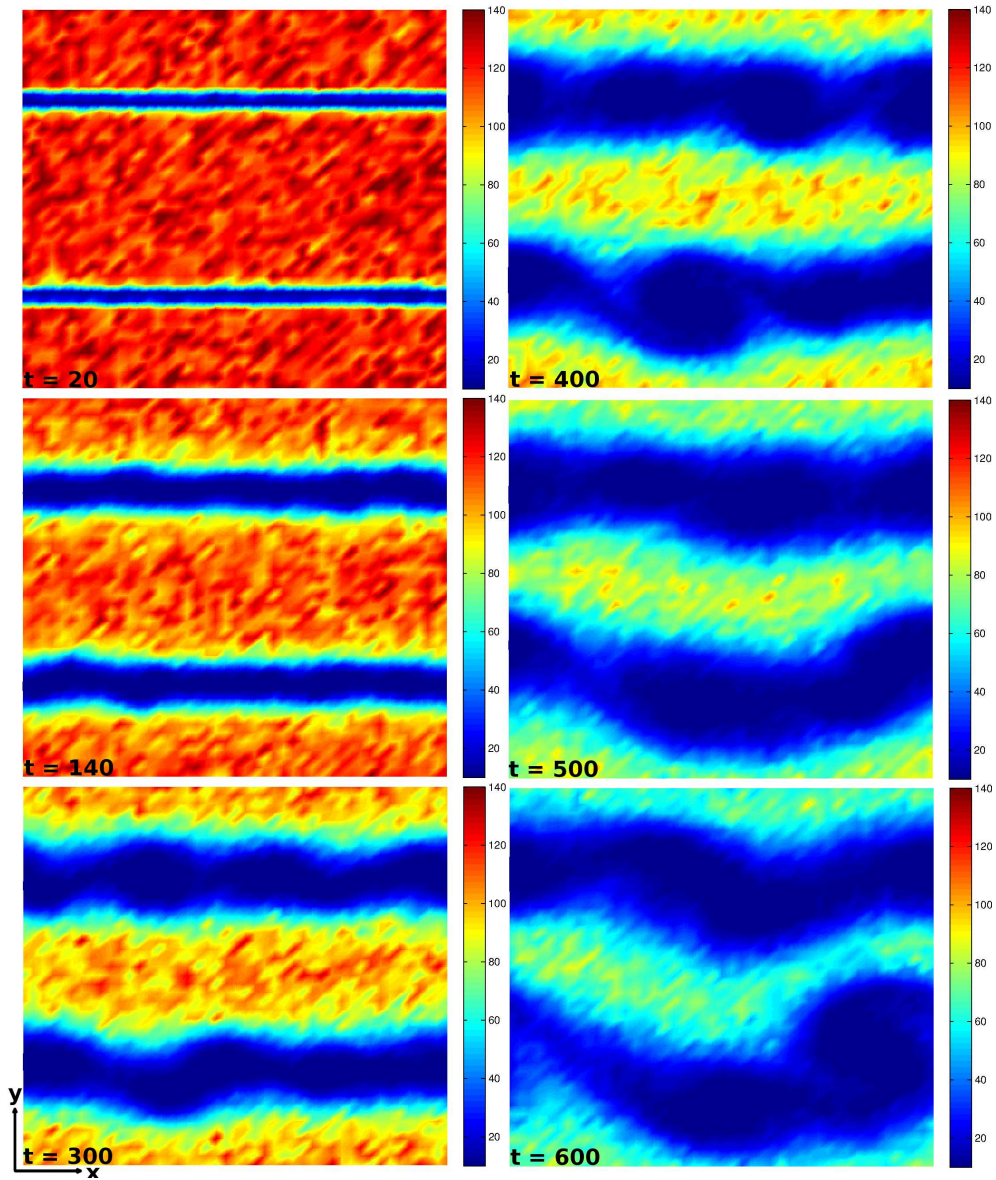


Figure 6.6: Γ contour plots at different times showing the spatio-temporal growth of heat front (Ashwin and Ganesh, 2011a). It is easily seen that the development of heat front follows the spatial profile of coherent structures as seen in Figure 6.3

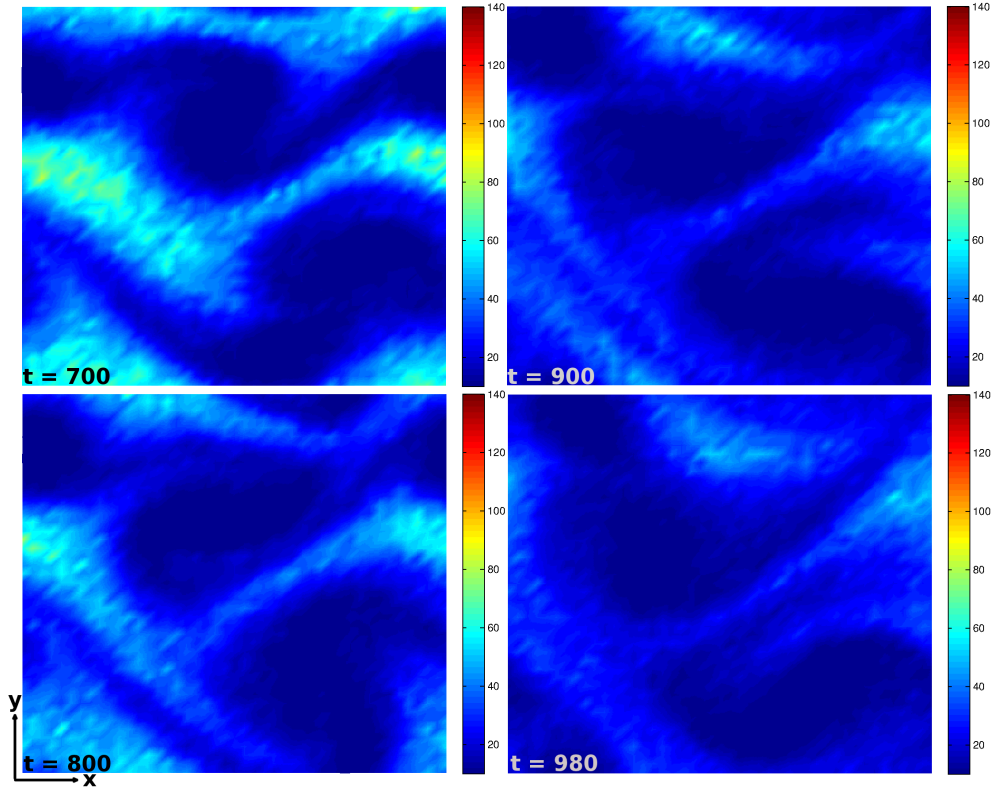


Figure 6.6: Continued

where \mathbf{v}_i is the velocity of i^{th} grain in the bin at location (x, y) on the 45×45 grid. \mathcal{N} and $\bar{\mathbf{v}}$ are the total number of grains and average velocity in the specified bin. The spatio-temporal growth of heat front reveals particle heat generation - an effect of velocity shear. In Figure 6.6, we see the spreading of hot regions due to particle heat generation. At $t = 20$, this hot region is confined close to the shear layer at $y = \pm 120$. In the nonlinear regime, a spatial growth (“widening”) of this hot region continues due to velocity shear close to vortex boundaries. Interestingly, while part of flow energy is transferred towards the largest possible length scale due to inverse cascade (see Figure 6.3 and 6.5), at the smallest scale there is also a simultaneous transfer of this flow energy into thermal velocities of grains.

The temporal evolution of thermal kinetic energy of the liquid can be obtained by constructing a spatial average of instantaneous $\Gamma(x, y, t)$ as follows:

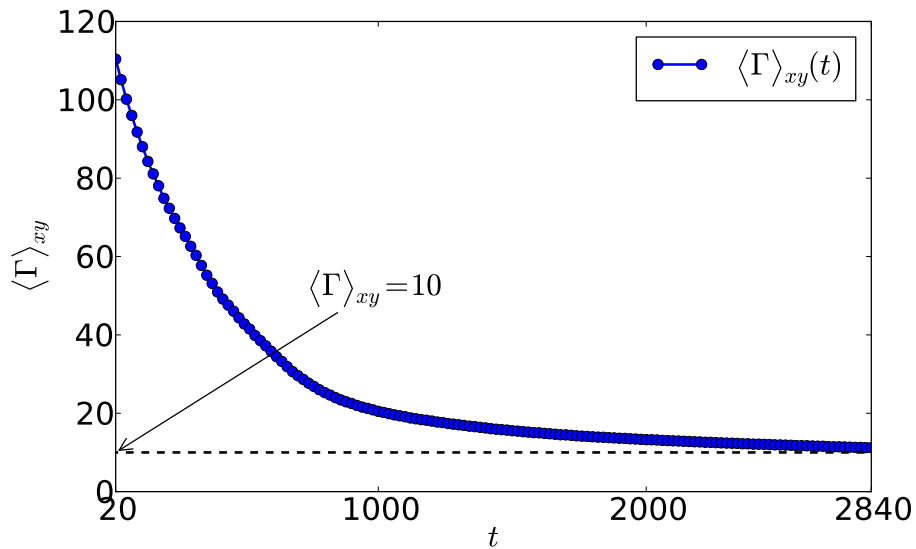


Figure 6.7: Plot of $\langle \Gamma \rangle_{xy}$ at different times for the full system ($\pm 240, \pm 240$). The rise in thermal kinetic energy (fall in Γ) is easily seen from this figure.

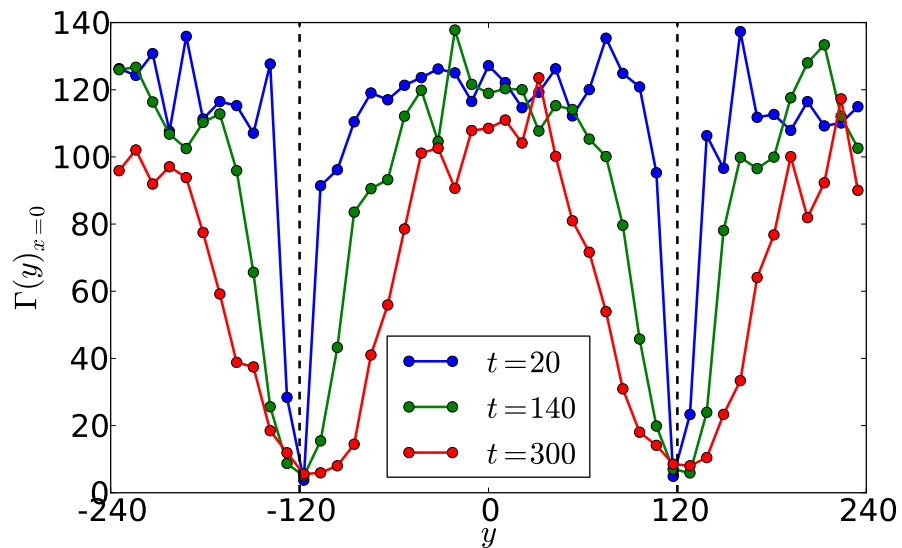


Figure 6.8: Profiles of the coupling parameter as function of y at $x = 0$: $\Gamma(y)_{x=0}$ at different times. The initial state is a uniform $\Gamma = 120$. These profiles show the propagation of heat front corresponding to the first three panels of Figure 6.6. Dashed lines show the location of initial shear layer at $y = \pm 120$.

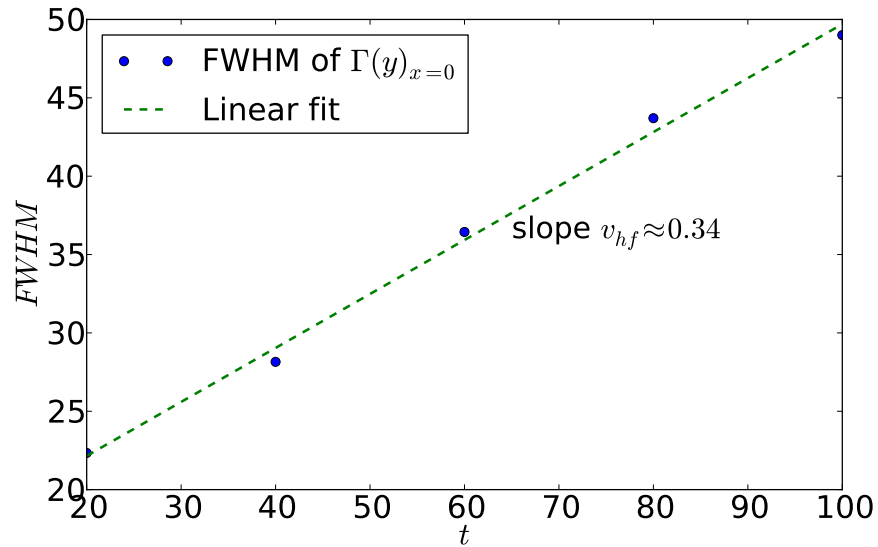


Figure 6.9: Time evolution of “full width half maxima” (FWHM) of $\Gamma(y)_{x=0}$ in the linear regime. Dashed line shows a linear fit having slope v_{hf} , which is the propagation speed of the heat front.

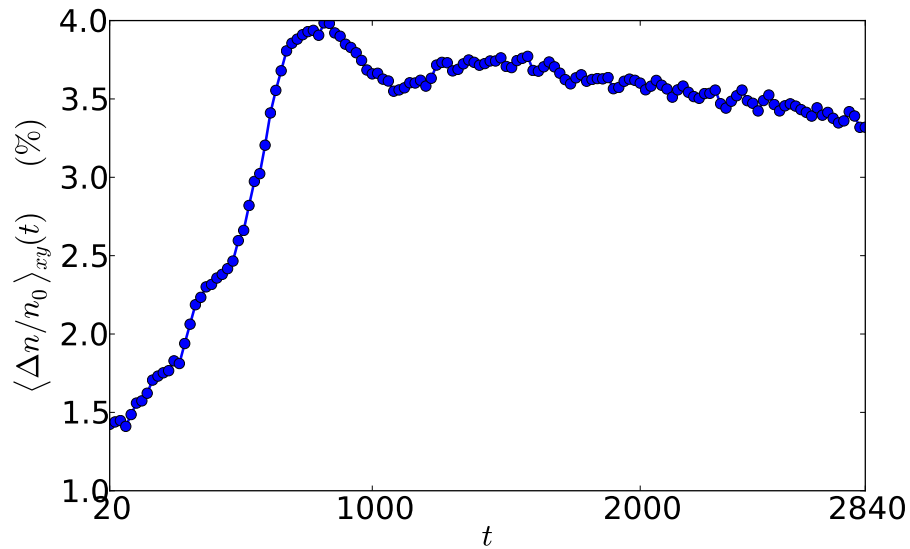


Figure 6.10: Time evolution of spatially averaged density variation normalized to initial background density (n_0). It is clearly seen that the peak density variation is around 4% which is observed close to $t \sim 800$. At such late times, inverse cascade has already resulted in the formation of large scale coherent structures in the liquid [see Figure 6.3]

$$\langle \Gamma \rangle_{xy}(t) = \frac{1}{L^2} \int \int \Gamma(x, y, t) dx dy \quad (6.8)$$

where $\langle \dots \rangle_{xy}$ correspond to instantaneous spatial average over the entire 2D system. In Figure 6.7, we show a plot showing the time evolution of $\langle \Gamma \rangle_{xy}$. The generation of heat in the system is evident from the fall of $\langle \Gamma \rangle_{xy}$ in time. It should be noted that the total energy of the 2D Yukawa liquid

$$E = 0.5 \left[\sum_i^N \mathbf{v}_i^2 + \sum_{i \neq j}^N \frac{1}{r_{ij}} \exp(-\kappa r_{ij}) \right] \quad (6.9)$$

remains conserved upto $10^{-5}\%$ throughout the simulation (not shown here). To further elucidate this spatio-temporal growth of heat front, we obtain the profile of Γ as a function of y at $x = 0$ and plot this at various times (see Figure 6.8). One can clearly see the propagation (“widening”) of heat front starting from a thermally equilibrated background at $t = 20$. To aid the reader, we have shown the location of initial shear layer ($y = \pm 120$) with vertical dashed lines.

The propagation speed of the heat front can be obtained by from the time evolution of “full width half maxima” (FWHM) of $\Gamma(y)_{x=0}$ in the linear regime (see Figure 6.9). The dashed line shows a linear fit, the slope of which gives the propagation speed v_{hf} of the heat front. In our normalized units $v_{hf} \approx 0.34$, which is much lesser than the adiabatic sound speed $c_s \approx 2.4$ at background $\Gamma = 120$. As shown in Figure 6.6, beyond this linear regime, structures begin to develop in the the heat front and it no longer remains symmetric about \hat{x} or \hat{y} . As time evolves and the heat front propagates nonlinearly, one can clearly see the local modulation of grain number density $n(x, y)$. The deviation from incompressibility can be quantified by taking a spatial average of density variation normalized to background density $n_0 = 1$ (in normalized units $n_0 = 1$) as follows:

$$\left\langle \left| \frac{\Delta n}{n_0} \right| \right\rangle_{xy}(t) = \frac{1}{L^2} \int \int \left| \frac{n_0 - n(x, y, t)}{n_0} \right| dx dy \quad (6.10)$$

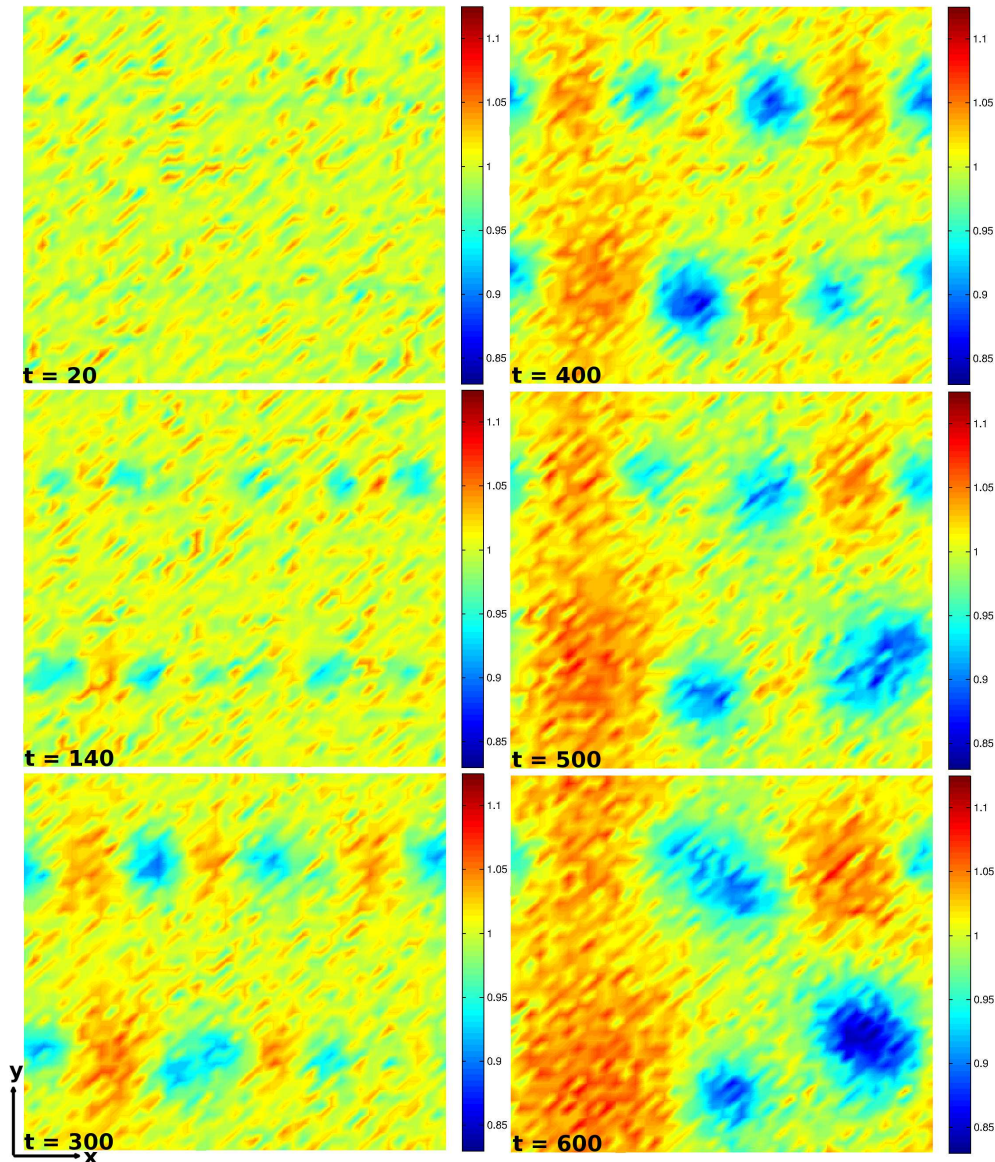


Figure 6.11: Snapshots of density profile $n(x, y)$ for the full system ($\pm 240, \pm 240$) shown at different times. As the heat front evolves (see Figure 6.6), hot zones expand in size and push grains into nearby cooler zones. This is evident from the reduced densities in hotter zones compared to cooler zones.

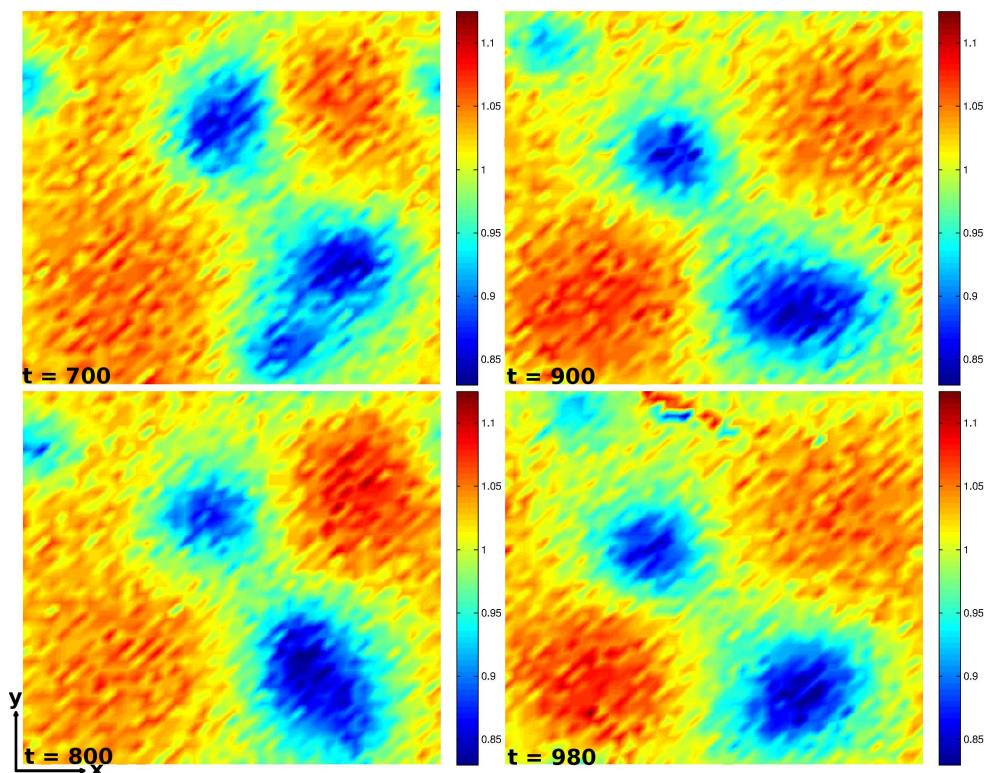


Figure 6.11: Continued

In Figure 6.10, we plot the time evolution of $\langle |\frac{\Delta n}{n_0}| \rangle_{xy}$ and see that the peak value of density variation is around 4% at $t \sim 800$. At such late times, large scale coherent structures “vortices” have already been formed due to inverse cascade [see Figure 6.3]. The development of heat front and its spatio-temporal growth is also manifested in Figure 6.11, where we show the time evolution density contour plots. One can clearly see the development of both low and high density zones as the time evolves. These zones are the manifestations of onset of hot and cool regions respectively. This is because these hot zones push the particles towards comparatively cooler zones.

6.8 Summary

For the first time, using large scale MD simulations, we have reported, the coevolution of inverse cascade and spatio-temporal growth of a heat front in

parallel shear flows of strongly coupled Yukawa liquids. At a given coupling strength, a subsonic shear profile is superposed on an equilibrated Yukawa liquid and KH instability is observed. The onset of nonlinear regime of the instability is observed by emergence of coherent vortices. The characterization of these coherent vortices is done through grain color coding, contour plots of vorticity ω and Okubo-Weiss parameter \mathcal{Q} . Inverse cascading of KH modes towards the largest scales is shown quantitatively. Concurrently, it is seen that shear flows lead to generation of heat at the smallest scales (“particle level”) resulting into the formation of a heat front. The spatio-temporal growth of this heat front is elucidated through the contour plots of inverse temperature Γ and grain density n . It is seen that the heat front propagates at speeds much lesser than the adiabatic sound speed of the system for the initial equilibrium chosen. It will be interesting to perform the present shear flow studies at supersonic speeds, a subject which we defer for future work. In the following chapter, we present a summary of the work done in this thesis.

Chapter 7

Conclusions

The present thesis investigates large scale hydrodynamic flows in complex “dusty” plasma through “first principles” classical MD simulations. To this end, a parallel **M**ulti **P**otential **M**olecular **D**ynamics (MPMD) code is developed using C language ([Ashwin and Ganesh, 2009](#)). The code can handle Lennard Jones, Yukawa and Tersoff-Brenner potentials. For the case of Yukawa liquids, the code is benchmarked exhaustively against several known results ([Donko et al., 2008](#)). The prototype system used in all the fluid dynamics studies reported here is a 2D strongly coupled Yukawa liquid. The results reported here are exact numerical solutions to the N body problem and hence “first principles” in nature. Wherever possible, comparison between MD results and a generalized hydrodynamic (GH) model is presented. In the following, we present a detailed discussion of the results and scope for future work in the present thesis.

7.1 Results

The thesis work begins with the development of the MPMD code. [Chapter 2](#) presents the computational methods used in the code in full detail. The code is benchmarked against several known results such as dispersion relations shown in ([Donko et al., 2008](#)). Presently, the code can handle Yukawa and Lennard-Jones inter-atomic potentials. Boundaries can be easily imple-

mented in both periodic or hard walls fashion. MPMD can simulate various thermodynamic ensembles such as NVT, NVE, NPT by employing a Gaussian thermostat (Evans et al., 1983) and an Andersen barostat (Andersen, 1980). To capture the underlying physics, several statistical mechanics and fluid dynamics diagnostics are developed. A test problem is then undertaken where we study the effect of a small external drive on a strongly coupled Yukawa solid. In particular, we report for the first time, extensive equilibrium and non-equilibrium molecular dynamics simulations on 3D Yukawa systems with periodic boundary conditions along \hat{x} , \hat{y} and \hat{z} , under a small external drive. The form of the drive taken is given by $V = V_0 \cos(k_L z) \Theta(t - t_0)$, where $\Theta(t - t_0)$ is a Heaviside step function in time and $k_L = 2\pi/L$, L being the size of the system. The long-range nature of the force and the periodic boundaries were properly handled by including Ewald sums. The initial state of the system of 432 particles is a regular BCC state. We then apply a small external drive and observe the melting of the system. After the initial transients die down we measure statistical properties like the self diffusion coefficient, mean square displacement and Fourier transformed velocity auto-correlation functions. The solid to liquid melting transition is discussed on the basis of these statistical properties and a mechanism for melting is proposed based on local heating in the system in regions where the magnitude of forces are maximum. We also qualitatively explain the decrease in melting times with increasing the magnitude of external drive V_0 . For a given (Γ, κ) pair, we have found a critical amplitude of external drive V_0^c below which there is no transition. This critical amplitude (V_0^c) depend on the location of the Yukawa system in the (κ, Γ) phase space. It is seen that for larger Γ , the value of V_0^c is larger. The melting problem addressed in this chapter serves as a benchmark for all the diagnostics of the MPMD code which is then used to study large scale hydrodynamic phenomena in subsequent chapters.

In chapter 3, we present the results of our first fluid dynamics study in complex plasma- the ‘‘Kelvin Helmholtz (KH) instability’’. For this, we take 2.5×10^5 grains in a simulation square box of size $640a$ and density $n = 1/a^2$, where $a \approx 0.4$ mm. This corresponds to a region size 26cm. Such a system size is comparable to the macroscopic length scales usually seen in labora-

tory experiments. Starting from a thermally equilibrated strongly coupled Yukawa liquid, we report for the first time, KH destabilization of a double step velocity shear profile (Ashwin and Ganesh, 2010a). The linear growth rates (γ) are directly computed from MD simulations and vortex roll formation in the non-linear regime is reported. The most interesting feature we notice here is the increase of instability growth rate with strong coupling. We also observe inverse cascading of the modes in time. For a comparison, growth rate spectra of KH instability has been obtained analytically using a generalized hydrodynamic (GH) model (Ashwin and Ganesh, 2010b). To this end, we have performed a linear stability analysis of the GH model equations using the assumption of incompressibility. The growth rates obtained from the linear stability calculations are compared with the MD simulations and the agreement is seen to be only qualitative. Inclusion of the effect of shear heating as an effective coupling parameter Γ_e appears to improve the quantitative comparison as well. However, we find a general disagreement between GH and MD growth rates at high mode numbers for all values of Γ_e . This could be due to the limitations of the GH model especially the uncertainties in the determination of viscosity $\eta(\Gamma)$ and viscoelastic relaxation time τ_m . The emergence of coherent vortices in the nonlinear regime of KH destabilized flows motivates one to think of the stability of an isolated coherent vortex, which is the subject matter of the following chapter.

In chapter 4, we present the results of our second study, namely “axisymmetric flows” in complex plasma. Here, we demonstrated for the first time, through large scale MD simulations, the emergence of isolated coherent tripolar vortices from the decay of unstable axisymmetric flows in strongly coupled Yukawa liquids (Ashwin and Ganesh, 2011b). Linear growth rates of the instability are directly obtained from “first principles” MD simulations and emergence of coherent tripolar vortices in the non-linear regime is reported. The tripoles formed are very robust and persist for several eddy turnover times. An attempt is made to compare the growth rates obtained from MD simulations with the GH fluid model. Our work expands the possibility of observing such tripolar vortices in laboratory experiments on complex plasmas, condensed matter systems and astrophysical systems such as

white dwarfs thereby vastly extending the generality of the phenomenon. In this chapter it was seen that a tripolar vortex under certain conditions can spontaneously decay into a pair of dipolar vortices propagating in mutually opposite directions. One naturally wonders if it is then possible to excite such dipolar vortices from generic initial conditions and study their interactions in a laboratory produced complex plasma. In the following chapter, the emergence of dipolar vortices from the self organization of an initial jet profile in a 2D strongly coupled Yukawa liquid is discussed in detail.

In chapter 5, we have reported, for the first time, through “first principles” classical MD simulations, the formation and collision of dipolar vortices in a prototype 2D strongly coupled Yukawa liquid (Ashwin and Ganesh, Under Review). A dipolar vortex is seen to emerge from the self-organization of an initial sub-sonic jet profile, and, in general, is seen to have a nonlinear relation between vorticity and stream function. The dipoles formed are very robust and our simulations reveal that a centered head-on collisions between two such dipolar vortices results into exchange of partners but no mass is exchanged. For such dipoles to exist for longer times, the neutral gas friction needs to be small in value. At higher values of gas friction, the inertial effects needed to sustain a dipole are rapidly quenched and the dipole is lost. Our work suggests the possibility of observing such dipolar vortices and their interactions in laboratory experiments on strongly coupled complex plasma at low values of gas friction, thereby, vastly extending the generality of the phenomenon.

In the foregoing shear flow studies, generation of heat is observed at the particle level close to shear layers. Similar generation of molecular heat has been observed in MD simulation of flows past an obstacle (Rapaport and Clementi, 1986a; Rapaport, D. C., 1995). Recently, a study on the evolution of shear induced melting has been reported experimentally by Feng and Goree (Feng et al., 2010), where they apply a sudden shear and observe the spatiotemporal development of the melting front. Their experiments thus corroborates our results on shear induced heating in both parallel and azimuthal shear flows. In chapter 6, perhaps for the first time, we report the development and spatio-temporal growth of a heat front in parallel shear

flows of strongly coupled Yukawa liquids (Ashwin and Ganesh, 2011a). At a given coupling strength, a subsonic shear profile is superposed on an equilibrated Yukawa liquid and KH instability is observed. The onset of nonlinear regime of the instability is observed by emergence of coherent vortices. The characterization of these coherent vortices is done through grain color coding, contour plots of vorticity ω and Okubo-Weiss parameter \mathcal{Q} . Inverse cascading of KH modes towards the largest scales is shown quantitatively. Concurrently, it is seen that shear flows lead to generation of heat at the smallest scales (“particle level”) resulting into the formation of a heat front. The spatio-temporal growth of this heat front is elucidated through the contour plots of inverse temperature Γ and grain density n . It is seen that the heat front propagates at speeds much lesser than the adiabatic sound speed of the system for the initial equilibrium chosen.

7.2 Future Work

As the present thesis focuses on “first principles” MD simulations of large scale flows in Yukawa liquids, one can think of several possible improvements in the present study. For eg. the inclusion of ion drag forces which result from momentum transfer from the flowing ions to charged dust grains. This can be an exceptionally important factor in complex plasmas. Ion flows are usually induced due to “global” large scale electric fields that can be either caused by natural inhomogeneities in a discharge plasma (ambipolar fields) or induced by external forces to manipulate dust grains. For typical experimental conditions the ion drag is pointed in the direction opposite to the electric force, and their competition usually determines global structures in complex plasmas (Goree et al., 1999). It can also result from the electric field that originates from the sheath where dusty plasma layer is formed due to the balance of gravity and cathode bias. The sheath is negatively charged and hence attracts ions at near acoustic speeds and hence the ions flow in and around the dusty plasma layer. The effect of ion drag forces leads to a new binary class of interaction such as an asymmetric Yukawa potential (Kompaneets et al., 2009). It will be interesting to study the phase transition and

hydrodynamic phenomena reported in the present thesis using this asymmetric Yukawa potential. The presence of temperature gradient in the neutral gas can also exert thermophoretic forces on the dust grains, which if included, can yield interesting consequences on the dynamics of dust grains and may alter the instabilities studied so far in the present thesis. One can also think of including the self consistent interaction between dust grains, ions, electrons and neutrals- an approach that will require massive computational power. Including a size distribution of dust grains instead of using point masses as in the present thesis may also lead to interesting consequences. The present code can also be easily modified to simulate ultra cold neutral (Killian et al., 1999) and ion-ion (Kanakasabapathy et al., 2001) plasmas.

In the following we list some of the possible future directions leading from the present thesis.

- Following the results for the driven Yukawa solids shown in chapter 2, one can think of several problems, such as, the effect of external drive at multiple values of forcing scale k_L , scaling of critical amplitude V_0^c with the screening parameter κ , and characterization of the nature of transition of Yukawa solid to a strongly correlated liquid. As a comparison, more rigorous potential models, such as the asymmetric Yukawa potential (Kompaneets et al., 2009; Ivlev et al., 2008) can be employed to study similar phenomena.
- In the area of parallel shear flows (see chapter 3), one can perform the stability analysis of the nonlinear GH model (Frenkel, 1946) and compare with growth rates directly obtained from MD simulations. It will be also very interesting perform such shear flow studies at supersonic speeds.
- In the context of centrifugal flows (see chapter 4), several important questions can be addressed, such as, the enhancement of transport length scales due to these coherent tripolar vortices, inertial power laws and inverse cascade phenomena in 2D turbulent strongly coupled liquids.

- Following the results on dipolar interaction studies shown in chapter 5, one can think of constructing Lamb like solutions (Lamb, 1932) and perform a nonlinear simulation of interacting jets using a lower dimensional generalized hydrodynamic model. It will be also very interesting to perform such dipole interaction studies at supersonic speeds. From our large scale MD simulations, the fluidization process yields a nonlinear relationship between fluid vorticity and stream function (See Figure 5.4, for example). Within the screened GH model, vorticity and stream function are related by: $\nabla^2\Psi - \kappa^2\Psi = \omega = \omega_{fit}$, where ω_{fit} is obtained from MD simulations. This nonlinear elliptic equation in Ψ if solved numerically would yield the structure of the coherent structure in the strongly coupled limit.

Appendix A

A.1 Gaussian Thermostat

Enforcing constant temperature amounts to introducing a nonholonomic constraint into the equations of motion in order to fix the kinetic energy and hence temperature. This is essentially a mathematical thermostat (Evans, 1983). The justification for this approach comes from the Gauss' principle of least constraint (Evans et al., 1983), which states that the following summation $\sum_i m_i (\ddot{\mathbf{r}}_i - \mathbf{F}_i/m_i)^2$ is minimized by the constrained motion. The equilibrium properties of this isothermal system can be shown to be those of the canonical ensemble (Evans and Moriss, 1984), but the dynamics must be handled with care especially if there are any macroscopic flows in the system, as the motion is no longer Newtonian. Since there are $3N$ degrees of freedom (ignoring the three lost to momentum conservation for 3D and two for 2D systems), the constraint equation taken to impose constant temperature is

$$\frac{1}{2} \sum_i^N \dot{\mathbf{r}}_i^2 = N E_k \tag{A.1}$$

The constrained equation of motion is

$$\ddot{\mathbf{r}}_i = \mathbf{F}_i/m_i + \alpha \dot{\mathbf{r}}_i \tag{A.2}$$

and since $\dot{E}k = 0$, and hence $\sum_i \mathbf{r}_i \cdot \ddot{\mathbf{r}}_i = 0$, it immediately follows that the value of the Lagrange multiplier α becomes

$$\alpha = -\frac{\sum_i \dot{\mathbf{r}}_i \cdot \mathbf{F}_i}{m \sum_i \dot{\mathbf{r}}_i^2} \quad (\text{A.3})$$

This constant temperature approach can also be combined with the leapfrog integrator as follows, see for eg. (Brown and Clarke, 1984)

$$\dot{\mathbf{r}}_i(t + \Delta t/2) = (1 + \alpha \Delta t) \dot{\mathbf{r}}_i(t - \Delta t/2) + \Delta t (1 + \alpha \Delta t/2) \mathbf{F}_i(t) \quad (\text{A.4})$$

where $\alpha = -\sum_i \dot{\mathbf{r}}_i(t) \cdot \mathbf{F}_i(t) / \sum_i \dot{\mathbf{r}}_i(t)^2$, and $\dot{\mathbf{r}}_i(t) = \dot{\mathbf{r}}_i(t - \Delta t/2) + (\Delta t/2) \mathbf{F}_i(t)$.

For further details regarding implementation in numerical codes, the reader should refer to (Rapaport, D. C., 1995) - an excellent recipe book for classical molecular dynamics methods.

A.2 Berendsen Barostat

Coupling to a constant pressure bath can be accomplished by adding an extra term to the equations of motion that affects the pressure change.

$$\left(\frac{dP}{dt} \right)_{bath} = \frac{P_0 - P}{\tau_P} \quad (\text{A.5})$$

The pressure is given by

$$P = \frac{2}{3V} (E_k - \Xi) \quad (\text{A.6})$$

where Ξ is the internal virial for pair-additive potentials

$$\Xi = -\frac{1}{2} \sum_{i < j} \mathbf{r}_{ij} \cdot \mathbf{F}_{ij} \quad (\text{A.7})$$

where $\mathbf{r}_{ij} = \mathbf{r}_i - \mathbf{r}_j$ and \mathbf{F}_{ij} is the force acting on particle i due to j . Since intramolecular contributions to the pressure vanish, in molecular systems Equations A.6 and A.7 can be evaluated using only the center of mass coor-

dinates and velocities and forces acting on the centers of mass. A pressure change can be accomplished by changing the virial through scaling of interparticle distances. A simple proportional coordinate scaling, concomitant with volume scaling, minimizes local disturbances (Berendsen et al., 1984). So an extra term in the equation of $\dot{x} = v$ is added, proportional to x :

$$\dot{x} = v + \alpha x \quad (\text{A.8})$$

while the volume changes accordingly:

$$\dot{V} = 3\alpha V \quad (\text{A.9})$$

The pressure change is related to the isothermal compressibility β :

$$\frac{dP}{dt} = -\frac{1}{\beta V} \frac{dV}{dt} = -\frac{3\alpha}{\beta} \quad (\text{A.10})$$

Along with Equation A.5, this determines α :

$$\alpha = -\beta(P_0 - P)/(3\tau_P) \quad (\text{A.11})$$

Thus the modified equation of motion is

$$\dot{x} = v - \frac{\beta(P_0 - P)x}{3\tau_P} \quad (\text{A.12})$$

Hence, a proportional scaling of coordinates and box length l (assuming an isotropic system in a cubic box) per time step from x to μx and l to μl with, to first order in Δt ,

$$\mu = 1 - \frac{\beta\Delta t}{3\tau_P}(P_0 - P) \quad (\text{A.13})$$

An equivalent expression to the same order is

$$\mu = \left[1 - \frac{\Delta t}{\tau_P}(P_0 - P) \right]^{1/3} \quad (\text{A.14})$$

The compressibility, that may not accurately known, appears in the expression for the scaling factor μ . Since an inaccuracy in β only influence the accuracy of the noncritical time constant τ_P , the imprecision of β is of no consequence for the dynamics (Berendsen et al., 1984). If β is not known for the potential model that is used in the simulation, it is sufficient to use an experimental value for the physical system that is approximated by the simulation.

A.3 Ewald sums

We follow references (Salin and Cailol, 2000) and (Mazars, 2007) to develop the numerical scheme of our MD simulation. Consider a system of N atoms, each of which now carries a charge. A periodic array of replicated systems is created, in the spirit of the periodic boundary conditions to mimic an infinitely large system, but now, because of the long-range nature of the interactions, the energy of the replicated system includes contributions from all replicas since no truncation is imposed. The interaction energy is now given as

$$\phi(\mathbf{r}) = \phi(|\mathbf{r}|) + \sum_{\mathbf{n} \neq \mathbf{0}} \phi(|\mathbf{r} + \mathbf{n}L|) \quad (\text{A.15})$$

with $\phi(r)$ being the Yukawa potential in Equation(2.1). L is the size of the simulation box and $\mathbf{n} = (n_x, n_y, n_z)$. The contribution from replicated systems becomes important especially if the Debye screening length λ_D becomes comparable to or greater than size of the simulation box L . The above mentioned potential represents the interaction energy of particle i with particle j (at separation $\mathbf{r} = \mathbf{r}_j - \mathbf{r}_i$) and with all the periodic images of the particles. The infinite sum in Equation(A.15) represents the contribution from all the periodic images. In our MD simulations we calculate the total Ewald-Yukawa potential energy of the system by rewriting it as

$$\phi = \phi_{\mathbf{r}} + \phi_{\mathbf{k}} - \phi_{\text{Self}} \quad (\text{A.16})$$

Here $\mathbf{k} = (n_x, n_y, n_z) \frac{2\pi}{L}$. The short range contribution to Eqn (A.16) is given as

$$\begin{aligned} \phi_r = & \frac{1}{4} \sum_{ij} \sum_{\mathbf{n}} \operatorname{erfc} \left(\alpha |\mathbf{r}_{ij} + \mathbf{n}L| + \frac{\kappa}{2\alpha} \right) \exp(\kappa |\mathbf{r}_{ij} + \mathbf{n}L|) \\ & + \operatorname{erfc} \left(\alpha |\mathbf{r}_{ij} + \mathbf{n}L| - \frac{\kappa}{2\alpha} \right) \exp(-\kappa |\mathbf{r}_{ij} + \mathbf{n}L|) \end{aligned} \quad (\text{A.17})$$

and the long ranged contribution

$$\phi_{\mathbf{k}} = \frac{2\pi}{V} \sum_{\mathbf{k} \neq 0} \frac{\exp\left(-\frac{\mathbf{k}^2 + \kappa^2}{4\alpha^2}\right)}{\mathbf{k}^2 + \kappa^2} \left| \sum_i \exp(i\mathbf{k} \cdot \mathbf{r}_i) \right|^2 \quad (\text{A.18})$$

and the self interaction is given as

$$\phi_{\text{self}} = \left[\frac{\alpha}{\sqrt{\pi}} \exp\left(\frac{-\kappa^2}{4\alpha^2}\right) - \frac{\kappa}{2} \exp\left(\frac{-\kappa}{2\alpha}\right) \right] \quad (\text{A.19})$$

In our simulations the summation over \mathbf{k} in Eqn(A.18) is taken over 297 vectors subject to the constraint $|\mathbf{n}| = \sqrt{n_x^2 + n_y^2 + n_z^2} \leq 5$. The value of Gaussian width α is taken as $5.6/L$ (Salin and Cailol, 2000).

Though we have employed Ewald sums in our MD simulations, for large system size (L) and large screening parameter (κ), Ewald sums are not necessary (Liu and Goree, 2005).

Bibliography

- Ackerson, B. J. and Clark, N. A. (1981).** “Shear-Induced Melting.” *Phys. Rev. Lett.*, 46(2): 123–126.
- Allen, M. P. and Tildesley, D. J. (1999).** *Computer simulation of liquids*. Clarendon Press.
- Andersen, H. C. (1980).** “Molecular dynamics at constant pressure and/or temperature.” *J. Chem. Phys.*, 72: 2384–2393.
- Ashwin, J. and Ganesh, R. (2009).** “Effect of external drive on strongly coupled Yukawa systems: A nonequilibrium molecular dynamics study.” *Phys. Rev. E*, 80(5): 056408.
- Ashwin, J. and Ganesh, R. (2010a).** “Kelvin Helmholtz Instability in Strongly Coupled Yukawa Liquids.” *Phys. Rev. Lett.*, 104(21): 215003.
- Ashwin, J. and Ganesh, R. (2010b).** “Parallel shear flow instabilities in strongly coupled Yukawa liquids: A comparison of generalized hydrodynamic model and molecular dynamics results.” *Phys. Plasmas*, 17: 103706.
- Ashwin, J. and Ganesh, R. (2011a).** “Coevolution of inverse cascade and nonlinear heat front in shear flows of strongly coupled Yukawa liquids.” *Phys. Plasmas*, 18: 083704.
- Ashwin, J. and Ganesh, R. (2011b).** “Coherent Vortices in Strongly Coupled Liquids.” *Phys. Rev. Lett.*, 106(13): 135001.
- Ashwin, J. and Ganesh, R. (Under Review).** “Formation and interaction of dipolar vortices in strongly coupled liquids.”
- Balbus, S. A. and Hawley, J. F. (1998).** “Instability, turbulence, and enhanced transport in accretion disks.” *Rev. Mod. Phys.*, 70(1): 1–53.
- Barba, L. and Leonard, A. (2007).** “Emergence and evolution of tripole vortices from net-circulation initial conditions.” *Phys. Fluids*, 19: 017101.

- Barkan, A., Merlino, R., D'Angelo, N., of Iowa. Dept. of Physics, U., Astronomy, and of Naval Research, U. S. O. (1995).** "Laboratory observation of the dust-acoustic wave mode." *Phys. Plasmas*, 2(10): 3563–3565.
- Berendsen, H., Postma, J., Van Gunsteren, W., DiNola, A., and Haak, J. (1984).** "Molecular dynamics with coupling to an external bath." *The Journal of Chemical Physics*, 81: 3684.
- Berkovsky, M. A. (1992).** "Spectrum of low frequency modes in strongly coupled plasmas." *Physics Letters A*, 166(5-6): 365 – 368.
- Birk, G. T. and Wiechen, H. (2002).** "Shear flow instabilities in magnetized partially ionized dense dusty plasmas." *Phys. Plasmas*, 9(3): 964–970.
- Brown, D. and Clarke, J. (1984).** "A comparison of constant energy, constant temperature and constant pressure ensembles in molecular dynamics simulations of atomic liquids." *Molecular Physics*, 51(5): 1243–1252.
- Carton, X., Flierl, G., and Polvani, L. (1989).** "The generation of tripoles from unstable axisymmetric isolated vortex structures." *Europhys. Lett.*, 9: 339.
- Chu, J., Du, J., et al. (1994).** "Coulomb solids and low-frequency fluctuations in RF dusty plasmas." *Journal of Physics D: Applied Physics*, 27: 296.
- Couder, Y. and Basdevant, C. (1986).** "Experimental and numerical study of vortex couples in two-dimensional flows." *Journal of Fluid Mechanics*, 173(-1): 225–251.
- D'Angelo, N. and Song, B. (1990).** "The Kelvin-Helmholtz instability in dusty plasmas." *Planetary and Space Science*, 38(12): 1577 – 1579.
- Delhommelle, J. (2004).** "Simulations of shear-induced melting in two dimensions." *Phys. Rev. B*, 69(14): 144 117.
- Donkó, Z., Hartmann, P., and Kalman, G. (2009).** "Two-dimensional dusty plasma crystals and liquids." *Journal of Physics: Conference Series*, 162: 012 016.
- Donko, Z., Kalman, G. J., and Hartmann, P. (2008).** "Dynamical correlations and collective excitations of Yukawa liquids." *Journal of Physics: Condensed Matter*, 20(41): 413 101 (35pp).

- Drazin, P. (1961).** *Journal of Fluid Mechanics*, 10: 571–583.
- Duc, J. and Sommeria, J. (1988).** “Experimental characterization of steady two-dimensional vortex couples.” *Journal of Fluid Mechanics*, 192(-1): 175–192.
- Dzwiniel, W., Alda, W., Pogoda, M., and Yuen, D. A. (2000).** “Turbulent mixing in the microscale: a 2D molecular dynamics simulation.” *Physica D: Nonlinear Phenomena*, 137(1-2): 157 – 171.
- Elhmaidi, D., Provenzale, A., and Babiano, A. (1993).** “Elementary topology of two-dimensional turbulence from a Lagrangian viewpoint and single-particle dispersion.” *Journal of Fluid Mechanics*, 257(-1): 533–558.
- Epstein, P. (1924).** “On the resistance experienced by spheres in their motion through gases.” *Physical Review*, 23(6): 710.
- Evans, D. and Moriss, G. (1984).** *Comp. Phys. Repts.*, 1: 297.
- Evans, D. J. (1983).** “Computer “experiment” for nonlinear thermodynamics of Couette flow.” *The Journal of Chemical Physics*, 78(6): 3297–3302.
- Evans, D. J., Hoover, W. G., Failor, B. H., Moran, B., and Ladd, A. J. C. (1983).** “Nonequilibrium molecular dynamics via Gauss’s principle of least constraint.” *Phys. Rev. A*, 28(2): 1016–1021.
- Feng, Y., Goree, J., and Liu, B. (2010).** “Evolution of Shear-Induced Melting in a Dusty Plasma.” *Phys. Rev. Lett.*, 104(16): 165 003.
- Fincham, D. and Ralston, B. J. (1981).** “Molecular dynamics simulation using the cray-1 vector processing computer.” *Computer Physics Communications*, 23(2): 127 – 134.
- Fortov, V., Ivlev, A., Khrapak, S., Khrapak, A., and Morfill, G. (2005).** “Complex (dusty) plasmas: Current status, open issues, perspectives.” *Phys. Reports*, 421(1-2): 1–103.
- Frenkel, Y. I. (1946).** *Kinetic Theory of Liquids*. Clarendon, Oxford.
- G J. Kalman, M. P. Rommel and K. B. Blagoev (Eds.) (1998).** *Strongly Coupled Coulomb Systems*. New York : Plenum Press.
- Gabor J. Kalman and Paul Carini (Eds.) (1977).** *Strongly Coupled Plasmas*. New York : Plenum Press.

- Goree, J., Morfill, G. E., Tsytovich, V. N., and Vladimirov, S. V. (1999). “Theory of dust voids in plasmas.” *Phys. Rev. E*, 59(6): 7055–7067.
- Gould, H. and Mazenko, G. F. (1975). “Coupling of Single-Particle and Collective Motions in a One-Component Plasma.” *Phys. Rev. Lett.*, 35(21): 1455–1458.
- Hamaguchi, S., Farouki, R. T., and Dubin, D. H. E. (1996). “Phase diagram of Yukawa systems near the one-component-plasma limit revisited.” *The Journal of Chemical Physics*, 105(17): 7641–7647.
- Hamaguchi, S., Farouki, R. T., and Dubin, D. H. E. (1997). “Triple point of Yukawa systems.” *Phys. Rev. E*, 56(4): 4671–4682.
- Hansen, J. and McDonald, I. (2006). *Theory of simple liquids*. Academic press.
- Hansen, J. P., McDonald, I. R., and Pollock, E. L. (1975). “Statistical mechanics of dense ionized matter. III. Dynamical properties of the classical one-component plasma.” *Phys. Rev. A*, 11(3): 1025–1039.
- Hartmann, P., Kalman, G. J., Donkó, Z., and Kutasi, K. (2005). “Equilibrium properties and phase diagram of two-dimensional Yukawa systems.” *Phys. Rev. E*, 72(2): 026 409.
- Hirshfeld, D. and Rapaport, D. C. (2000). “Growth of Taylor vortices: A molecular dynamics study.” *Phys. Rev. E*, 61(1): R21–R24.
- Hockney, R. and Eastwood, J. (1992). *Computer simulation using particles*. Institute of Physics.
- Hoffmann, G. P. and Lowen, H. (2000). “Melting of dusty plasma crystals in oscillating external fields.” *Journal of Physics: Condensed Matter*, 12(33): 7359–7370.
- Ichimaru, S., Iyetomi, H., and Tanaka, S. (1987). “Statistical physics of dense plasmas: Thermodynamics, transport coefficients and dynamic correlations.” *Physics Reports*, 149(2-3): 91 – 205.
- Ichimaru S. (1973). *Basic Principles of Plasma Physics: a Statistical Approach*. The Benjamin/Cummings Publishing Company, Inc., Reading, MA.

- Ivlev, A. V., Morfill, G. E., Thomas, H. M., Rath, C., Joyce, G., Huber, P., Kompaneets, R., Fortov, V. E., Lipaev, A. M., Molotkov, V. I., Reiter, T., Turin, M., and Vinogradov, P. (2008). “First Observation of Electrorheological Plasmas.” *Phys. Rev. Lett.*, 100(9): 095003.
- Kadau, K., Barber, J. L., Germann, T. C., and Alder, B. J. (2008). “Scaling of atomistic fluid dynamics simulations.” *Phys. Rev. E*, 78(4): 045301.
- Kadau, K., Germann, T., Hadjiconstantinou, N., Lomdahl, P., Dimonte, G., Holian, B., and Alder, B. (2004). “Nanohydrodynamics simulations: An atomistic view of the Rayleigh–Taylor instability.” *Proceedings of the National Academy of Sciences of the United States of America*, 101(16): 5851.
- Kanakasabapathy, S. K., Overzet, L. J., Midha, V., and Economou, D. (2001). “Alternating fluxes of positive and negative ions from an ion-ion plasma.” 78(1): 22–24.
- Kaw, P. K. and Sen, A. (1998). “Low frequency modes in strongly coupled dusty plasmas.” *Phys. Plasmas*, 5(10): 3552–3559.
- Khrapak, S., Samsonov, D., Morfill, G., Thomas, H., Yaroshenko, V., Rothermel, H., Hagl, T., Fortov, V., Nefedov, A., Molotkov, V., et al. (2003). “Compressional waves in complex (dusty) plasmas under microgravity conditions.” *Phys. Plasmas*, 10: 1.
- Khrapak, S. A., Ivlev, A. V., and Morfill, G. E. (2004). “Momentum transfer in complex plasmas.” *Phys. Rev. E*, 70(5): 056405.
- Killian, T. C., Kulin, S., Bergeson, S. D., Orozco, L. A., Orzel, C., and Rolston, S. L. (1999). “Creation of an Ultracold Neutral Plasma.” *Phys. Rev. Lett.*, 83(23): 4776–4779.
- Knuth, D. (1973). *The art of computer programming: sorting and searching*, volume 3. Addison Wesley Publishing Company.
- Kompaneets, R., Morfill, G. E., and Ivlev, A. V. (2009). “Design of new binary interaction classes in complex plasmas.” *Phys. Plasmas*, 16(4): 043705.
- Kramer, W., Clercx, H., and van Heijst, G. (2007). “Vorticity dynamics of a dipole colliding with a no-slip wall.” *Phys. Fluids*, 19: 126603.

- Kukharkin, N. (1995).** “Coherent structure formation, phase correlations, and finite-size effects in 2D turbulence.” *Journal of Scientific Computing*, 10(4): 409–448.
- Lamb, H. (1932).** *Hydrodynamics 6th ed.*
- Landau, L. D. and Lifschitz, E. M. (2007).** *Fluid mechanics*. Course of theoretical physics by L. D. Landau and E. M. Lifshitz, Vol. 6. Elsevier, 2 edition.
- Legras, B., Santangelo, P., and Benzi, R. (1988).** “High-resolution numerical experiments for forced two-dimensional turbulence.” *Europhys. Lett.*, 5: 37.
- Lin, Z., Hahm, T., Lee, W., Tang, W., and White, R. (1998).** “Turbulent transport reduction by zonal flows: Massively parallel simulations.” *Science*, 281(5384): 1835.
- Liu, B. and Goree, J. (2005).** “Shear Viscosity of Two-Dimensional Yukawa Systems in the Liquid State.” *Phys. Rev. Lett.*, 94(18): 185002.
- Liu, B. and Goree, J. (2008).** “Superdiffusion and Non-Gaussian Statistics in a Driven-Dissipative 2D Dusty Plasma.” *Phy. Rev. Lett.*, 100(5): 055003.
- Mazars, M. (2007).** “Ewald sums for Yukawa potentials in quasi-two-dimensional systems.” *The Journal of Chemical Physics*, 126(5): 056101.
- McQuarrie, D. A. (1976).** *Statistical Mechanics*. Harper and Row, New York.
- McWilliams, J. (1984).** “The emergence of isolated coherent vortices in turbulent flow.” *Journal of Fluid Mechanics*, 146: 21–43.
- McWilliams, J. (1985).** “Submesoscale, coherent vortices in the ocean.” *Reviews of Geophysics*, 23(2): 165–182.
- Montgomery D.C. and Tidman D.A (1964).** *Plasma kinetic theory*. McGraw Hill Book Company, Newyork.
- Morfill, G., Thomas, H., Konopka, U., Rothermel, H., Zuzic, M., Ivlev, A., and Goree, J. (1999).** “Condensed plasmas under microgravity.” *Physical review letters*, 83(8): 1598–1601.

- Morfill, G. E. and Ivlev, A. V. (2009).** “Complex plasmas: An interdisciplinary research field.” *Rev. Mod. Phys.*, 81(4): 1353–1404.
- Morfill, G. E., Rubin-Zuzic, M., Rothermel, H., Ivlev, A. V., Klumov, B. A., Thomas, H. M., Konopka, U., and Steinberg, V. (2004).** “Highly Resolved Fluid Flows: Liquid Plasmas at the Kinetic Level.” *Phys. Rev. Lett.*, 92(17): 175 004.
- Murillo, M. S. (2000).** “Critical Wave Vectors for Transverse Modes in Strongly Coupled Dusty Plasmas.” *Phys. Rev. Lett.*, 85(12): 2514–2517.
- Nielsen, A. and Rasmussen, J. (1997).** “Formation and temporal evolution of the Lamb-dipole.” *Phys. Fluids*, 9: 982.
- Nosenko, V. and Goree, J. (2004).** “Shear Flows and Shear Viscosity in a Two-Dimensional Yukawa System (Dusty Plasma).” *Phys. Rev. Lett.*, 93(15): 155 004.
- Nosenko, V., Zhdanov, S., Ivlev, A. V., Morfill, G., Goree, J., and Piel, A. (2008).** “Heat Transport in a Two-Dimensional Complex (Dusty) Plasma at Melting Conditions.” *Phys. Rev. Lett.*, 100(2): 025 003.
- Ohta, H. and Hamaguchi, S. (2000a).** “Molecular dynamics evaluation of self-diffusion in Yukawa systems.” *Physics of Plasmas*, 7: 4506.
- Ohta, H. and Hamaguchi, S. (2000b).** “Wave Dispersion Relations in Yukawa Fluids.” *Phys. Rev. Lett.*, 84(26): 6026–6029.
- Okubo, A. (1970).** “Horizontal dispersion of floatable particles in the vicinity of velocity singularities such as convergences.” *Deep Sea Research and Oceanographic Abstracts*, 17(3): 445 – 454.
- Orlandi, P. and van Heijst, G. (1992).** “Numerical simulation of tripolar vortices in 2D flow.” *Fluid Dynamics Res.*, 9(4): 179–206.
- Pedlosky, J. (1987).** *Geophysical fluid dynamics*. Springer.
- Perlekar, P. and Pandit, R. (2009).** “Statistically steady turbulence in thin films: direct numerical simulations with Ekman friction.” *New Journal of Physics*, 11(7): 073 003.
- Pramanik, J., Prasad, G., Sen, A., and Kaw, P. K. (2002).** “Experimental Observations of Transverse Shear Waves in Strongly Coupled Dusty Plasmas.” *Phys. Rev. Lett.*, 88(17): 175 001.

- Puhl, A., Mansour, M. M., and Mareschal, M. (1989).** “Quantitative comparison of molecular dynamics with hydrodynamics in Rayleigh-Bénard convection.” *Phys. Rev. A*, 40(4): 1999–2012.
- Rahman, A. (1964).** “Correlations in the motion of atoms in liquid argon.” *Physical Review*, 136(2A): 405–411.
- Rapaport, D. and Clementi, E. (1986a).** “Eddy formation in obstructed fluid flow: a molecular-dynamics study.” *Phys. Rev. Lett.*, 57(6): 695–698.
- Rapaport, D. C. (1988).** “Molecular-Dynamics Study of Rayleigh-Bénard Convection.” *Phys. Rev. Lett.*, 60(24): 2480–2483.
- Rapaport, D. C. and Clementi, E. (1986b).** “Eddy Formation in Obstructed Fluid Flow: A Molecular-Dynamics Study.” *Phys. Rev. Lett.*, 57(6): 695–698.
- Rapaport, D. C. (1995).** *The Art of Molecular Dynamics Simulation*. Cambridge University Press.
- Rivera, M., Wu, X.-L., and Yeung, C. (2001).** “Universal Distribution of Centers and Saddles in Two-Dimensional Turbulence.” *Phys. Rev. Lett.*, 87(4): 044 501.
- Rosenberg, M. and Kalman, G. (1997).** “Dust acoustic waves in strongly coupled dusty plasmas.” *Phys. Rev. E*, 56(6): 7166–7173.
- Rostoker, N. and Rosenbluth, M. N. (1960).** “Test Particles in a Completely Ionized Plasma.” 3(1): 1–14. URL <http://dx.doi.org/doi/10.1063/1.1705998>.
- S. Chandrasekhar (1998).** *Hydrodynamic and Hydromagnetic Stability*. Dover publications, New York.
- Saigo, T. and Hamaguchi, S. (2002).** “Shear viscosity of strongly coupled Yukawa systems.” *Phys. Plasmas*, 9(4): 1210–1216.
- Salacuse, J. J., Denton, A. R., and Egelstaff, P. A. (1996).** “Finite-size effects in molecular dynamics simulations: Static structure factor and compressibility. I. Theoretical method.” *Phys. Rev. E*, 53(3): 2382–2389.
- Salin, G. and Cailol, J. (2000).** “Ewald sums for Yukawa potentials.” *J. Chem. Phys.*, 113(23): 10 459 – 10 463.

- Schmidt, P., Zwicknagel, G., Reinhard, P. G., and Toepffer, C. (1997).** “Longitudinal and transversal collective modes in strongly correlated plasmas.” *Phys. Rev. E*, 56(6): 7310–7313.
- Totsuji, H. (2001).** “Structure and melting of two-dimensional dust crystals.” volume 8, pages 1856–1862. AIP.
- Totsuji, H., Kishimoto, T., and Totsuji, C. (1997).** “Structure of Confined Yukawa System (Dusty Plasma).” *Phys. Rev. Lett.*, 78(16): 3113–3116.
- Tsyтович, V., Morfill, G., Vladimirov, S., and Thomas, H. (2008).** “Elementary physics of complex plasmas.” In “Lecture Notes in Physics, Berlin Springer Verlag,” volume 731.
- Van Geffen, J. and Van Heijst, G. (1998).** “Viscous evolution of 2D dipolar vortices.” *Fluid dynamics research*, 22(4): 191–213.
- Van Heijst, G. and Flor, J. (1989).** “Dipole formation and collisions in a stratified fluid.”
- Van Heijst, G. and Kloosterziel, R. (1989).** “Tripolar vortices in a rotating fluid.” *Nature*, 338: 569 – 571.
- Verheest, F. and Meuris, P. (1996).** “Nonlinear electromagnetic modes in plasmas with variable dust charges.” *Physics Letters A*, 210(3): 198 – 201. URL <http://www.sciencedirect.com/science/article/pii/S0375960196800107>.
- Verlet, L. (1967).** “Computer ”Experiments” on Classical Fluids. I. Thermodynamical Properties of Lennard-Jones Molecules.” *Phys. Rev.*, 159(1): 98.
- Weiss, J. (1991).** “The dynamics of enstrophy transfer in two-dimensional hydrodynamics.” *Physica D: Nonlinear Phenomena*, 48(2-3): 273–294.
- Wiechen, H. M. (2006).** “Simulations of Kelvin-Helmholtz modes in partially ionized dusty plasmas comparing different charge numbers, charge polarities, and masses of the dust.” *Phys. Plasmas*, 13(6): 062104.